

A Finite Difference Representation of Neutrino Radiation Hydrodynamics in Spherically Symmetric General Relativistic Space-Time

Matthias Liebendörfer^{1,2,3}, O. E. Bronson Messer^{1,2,6}, Anthony Mezzacappa²,
Stephen W. Bruenn⁴, Christian Y. Cardall^{1,2,6}, and F.-K. Thielemann⁵

ABSTRACT

We present an implicit finite difference representation for general relativistic radiation hydrodynamics in spherical symmetry. Our code, AGILE-BOLTZTRAN, solves the Boltzmann transport equation for the angular and spectral neutrino distribution functions in self-consistent simulations of stellar core collapse and postbounce evolution. It implements a dynamically adaptive grid in comoving coordinates. A comoving frame in the momentum phase space facilitates the evaluation and tabulation of neutrino-matter interaction cross sections, but produces a multitude of observer corrections in the transport equation. Most macroscopically interesting physical quantities are defined by expectation values of the distribution function. We optimize the finite differencing of the microscopic transport equation for a consistent evolution of important expectation values. We test our code in simulations launched from progenitor stars with 13 solar masses and 40 solar masses. Half a second after core collapse and bounce, the protoneutron star in the latter case reaches its maximum mass and collapses further to form a black hole. When the hydrostatic gravitational contraction sets in, we find a transient increase in electron flavor neutrino luminosities due to a change in the accretion rate. The μ - and τ -neutrino luminosities and rms energies, however, continue to rise because previously shock-heated material with a non-degenerate

¹Department of Physics and Astronomy, University of Tennessee, Knoxville, Tennessee 37996-1200

²Physics Division, Oak Ridge National Laboratory, Oak Ridge, Tennessee 37831-6354

³CITA, University of Toronto, Toronto, Ontario M5S 3H8, Canada

⁴Department of Physics, Florida Atlantic University, Boca Raton, Florida 33431-0991

⁵Department of Physics and Astronomy, University of Basel, Klingelbergstrasse 82, 4056 Basel, Switzerland

⁶Joint Institute for Heavy Ion Research, Oak Ridge National Laboratory, Oak Ridge, Tennessee 37831-6374

electron gas starts to replace the cool degenerate material at their production site. We demonstrate this by supplementing the concept of neutrinospheres with a more detailed statistical description of the origin of escaping neutrinos. Adhering to our tradition, we compare the evolution of the 13 solar mass progenitor star to corresponding simulations with the multi-group flux-limited diffusion approximation, based on a recently developed flux limiter. We find similar results in the postbounce phase and validate this MGFLD approach for the spherically symmetric case with standard input physics.

Subject headings: supernovae: general—neutrinos—radiative transfer—hydrodynamics—relativity—methods: numerical

1. Introduction

A supernova explosion is a dramatic event which includes such a rich diversity of physics (Bethe 1990; Burrows & Young 2000; Mezzacappa & Bruenn 2000; Janka, Kifonidis & Rampp 2001) that self-consistent numerical simulations on current computer hardware do not allow to include all relevant pieces at once. After stellar core collapse, a nascent neutron star is formed at the center of the event, requiring a description in general relativity. Neutrinos generated in the compactifying region are tightly coupled to the matter at high densities, while they leak or stream out at lower densities. The collapsing stellar core bounces as the equation of state stiffens when nuclear densities are exceeded, and a shock wave is formed that ploughs outwards through the still infalling outer layers. Multi-frequency radiation hydrodynamics must be used to quantify the energy that the neutrinos deposit in the material behind the shock. This energy deposition has been considered to be essential for the success or failure of the supernova explosion (Colgate & White 1966; Wilson 1985; Bethe & Wilson 1985). Observational and theoretical evidence suggests that this neutrino heating drives convection behind the shock. Instabilities in the protoneutron star, significant rotation, and strong magnetic fields further complicate the picture. Observations of neutron star kicks, mixing of nuclear species, inhomogeneous ejecta, and polarization of spectra support the presence of asymmetries in supernova explosions (Tueller et al. 1991; Strom et al. 1995; Galama et al. 1998; Leonard et al. 2000). Motivated by such observations, the neutrino driven explosion mechanism has been explored in multidimensions (Herant, Benz, & Colgate 1992; Miller, Wilson, & Mayle 1993; Herant et al. 1994; Burrows, Hayes, & Fryxell 1995; Janka & Müller 1996; Mezzacappa et al. 1998; Fryer & Heger 2000; Fryer & Warren 2002), and alternative jet-based explosion scenarios have received new momentum (Höflich, Wheeler, & Wang 1999; Khokhlov et al. 1999; MacFadyen & Woosley 1999;

Wheeler et al. 2000).

Because of their excessive computational demand, multi-dimensional simulations have had to rely on physically significant approximations. Simulations are performed that impose the neutrino radiation field externally or uniformly, that prescribe the neutrino spectrum *ab initio*, that artificially seed instabilities, or that insert jets in order to explore important phenomena of supernova explosions in observational data. A complementary approach is to model supernovae in spherical symmetry. Spherically symmetric simulations of stellar core collapse reach back to the late sixties (Colgate & White 1966; May & White 1967; Arnett 1967; Schwartz 1967; Wilson 1971) when computers first became available. Although the assumption of pure spherical symmetry is also a physically significant simplification, it can provide an essential contribution to the quality of numerical supernova models and their interpretation. A spherically symmetric model can implement full general relativity. Additionally, the reduced number of computational zones allows an accurate treatment of neutrino radiation transport and the inclusion of sophisticated microscopic input physics. During the search for a robust supernova mechanism, standards in the nuclear input physics (Lattimer & Swesty 1991) and weak interaction physics (Bruenn 1985) have been established. In recognition of the importance of neutrino transport in the supernova, its numerical treatment has been improved from simple leakage schemes (Van Riper & Lattimer 1981; Baron, Cooperstein, & Kahana 1985) to multi-group flux-limited diffusion (MGFLD) approximations (Arnett 1977; Bowers & Wilson 1982; Bruenn 1985; Myra et al 1987) to investigations of the full Boltzmann transport equation (Mezzacappa & Bruenn 1993a; Messer et al. 1998; Yamada, Janka, & Suzuki 1999; Burrows et al. 2000; Rampp & Janka 2002). Only recently have self-contained simulations of stellar core collapse and postbounce evolution with Boltzmann neutrino transport been performed, in Newtonian gravity and the $O(v/c)$ limit (Rampp & Janka 2000; Mezzacappa et al. 2001; Thompson, Burrows, & Pinto 2003) and in general relativistic space-time (Liebendörfer et al. 2001). They allow, on the one hand, the exploration of nuclear physics under extreme conditions, and, on the other hand, provide a solid point of reference for the construction of accurate multidimensional simulations (Buras et al. 2003b).

Basic numerical techniques for radiative transfer have been designed and continuously improved over the last three decades (see e.g. (Mihalas & Mihalas 1984) and (Lewis & Miller 1984) for a review). In most applications, photons or neutrons are the transported particles. In our application to supernova dynamics, the transport of neutrinos requires a new combination of capabilities derived from both fields, photon and neutron transport.

As in *neutron transport* the radiation particles are fermions. In contrast to photons, the neutrinos assume a Fermi-Dirac distribution in thermal equilibrium. Weak interactions with

nuclear matter can be suppressed due to Pauli blocking of final states. This makes the dependence of the collision integral on the distribution function nonlinear. Several quantities have to be evolved with special care: An important constraint for the evolution of neutrino and electron abundances is lepton number conservation. While applications to photon transport do not require an exact count of photons as particles, the outcome of a supernova simulation sensitively depends on the deleptonization. The transfer of lepton number occurs via the reactions $e^- + p^+ \rightleftharpoons n + \nu_e$ and $e^+ + n \rightleftharpoons p + \bar{\nu}_e$ where the protons, p , and neutrons, n , are free or bound in nuclei. The electron neutrino, ν_e , and antineutrino, $\bar{\nu}_e$, may escape to infinity or be absorbed at distant locations. These reactions determine the electron fraction, and hence, the partial pressure of the electron gas in the fluid. This pressure contributes importantly to the dynamics if the electron gas is degenerate and the density lower than nuclear density. Beside of the transport of lepton number, the transport of energy is a crucial phenomenon in supernova dynamics. Neutrinos escaping from the accreting material and the protoneutron star may be absorbed behind the stalled shock. This energy transfer is believed to add to the thermal pressure behind the shock such that ultimately a supernova explosion is launched with the ejection of the outer layers (Colgate & White 1966; Bethe & Wilson 1985). Last, but not least, the evolution of the global energy should be monitored. Just before collapse, the progenitor star is marginally bound. During collapse, the binding energy of the nascent protoneutron star increases dramatically. It is balanced by the internal energy of the compressed matter and the trapped neutrinos. Only on a longer time scale is the energy of the radiation field transported away from the star while the emptied states in the neutrino phase space are immediately replenished by neutrino emission in the cooling protoneutron star. Since the gravitational energy, the internal energy, and the energy in the radiation field rise to the order of 10^{53} erg, a detailed analysis of global energy conservation is advised in order to make the comparatively small explosion energy of 10^{51} erg predictable. Whether we choose a kinetic equation for the propagation of particle number or an equation prescribing the evolution of radiation intensity, it is a numerical challenge to conserve both lepton number and energy with the same finite difference representation of the transport equation.

The following transport requirements more closely resemble the astrophysical applications of *photon transport* than neutron transport. Owing to the protoneutron star or black hole formed at the center of the event, space-time is curved. The particles follow geodesics in general relativistic space-time, i.e. their angular distribution is affected by gravitational bending. Additionally, the particle energies are subject to a gravitational frequency shift. In contrast to many neutron transport applications, the fluid is highly dynamic during collapse and even more so after shock formation. Thus, observer corrections for Doppler shift and angular aberration have to be implemented as in photon transport applications. However,

there is some freedom in the choice of where to apply these corrections. In an inertial frame they complicate the description of interactions in the collision integral. In a comoving frame they enter the transport terms in the Boltzmann equation.

We proceed with the latter choice in an S_N -method. Our code, AGILE-BOLTZTRAN, emerged from the following components: The neutrino transport part, BOLTZTRAN, has been developed for the simulation of stellar core collapse in an implicitly finite differenced $O(v/c)$ approximation (Mezzacappa & Bruenn 1993a,b,c). It has been compared to MGFLD in selected stationary state phases, and standard test problems for radiative transfer in supernovae have been performed (Messer et al. 1998; Messer 2000). AGILE is an implicit general relativistic hydrodynamics code that evolves the Einstein equations based on conservative finite differencing on an adaptive grid (Liebendörfer, Rosswog & Thielemann 2002). In this paper, we describe how these codes are merged and extended to enable accurate simulations of the very dynamic postbounce phase. In particular, we detail the finite differencing of the observer corrections for the dynamic conservation of particle number and total energy in the transport scheme, and describe the extension of BOLTZTRAN to general relativistic flows (Liebendörfer 2000). In section 2, we start with the characterization of the equation of state and a list of the included neutrino-matter interactions, followed by a collection of the basic equations of general relativistic radiation hydrodynamics in spherical symmetry. Two exemplary runs from collapse through bounce and postbounce evolution are also described in this section. In order to test our code in a broad range of conditions, we launched simulations from a small $13 M_\odot$ progenitor star (Nomoto & Hashimoto 1988) and a very massive $40 M_\odot$ progenitor star (Woosley & Weaver 1995). We investigate the different regions of neutrino emission in the star. Section 3 is entirely devoted to the documentation of the finite differencing in our computer model. In section 4, we analyze and verify the performance of our code in various example situations encountered in the evolution of the two simulation runs. We close the section with the comparison of our results with Bruenn’s multi-group flux-limited diffusion code which implements a recently developed new flux limiter (Bruenn 2002).

2. Physics in the Model

The physical model can be divided into two parts. On the one hand, there is the microscopic physics input—the specification of particle abundances and reaction cross sections. The microphysics in supernova models is continuously improving and many uncertainties remain to be resolved. However, in this methodological paper, we will only shortly summarize the ingredients that were standard at the time the code was written and hope that our code

AGILE-BOLTZTRAN will continue to be useful in future discussions and evaluations of input physics improvements. On the other hand, there are the radiation hydrodynamics equations we are solving on the computer. They are the foundation of our implementation of neutrino transport and receive a detailed discussion later in this section.

2.1. Equation of state and weak interactions

The equation of state describes the thermodynamical state of a fluid element based on density, ρ , temperature, T , and the composition. We use the equation of state of Lattimer & Swesty (1991). It assumes nuclear statistical equilibrium and we apply it wherever the density is larger than 10^7 g/cm³ and the temperature larger than 5×10^9 K. This region is described by a liquid drop model for a representative nucleus with atomic number A and charge Z , surrounded by free alpha particles, protons, and neutrons. The baryons are immersed in an electron and positron gas in equilibrium with a photon gas. Beyond nuclear density, where no isolated nuclei are present, the complicated population of hadrons (Glendenning 1985; Pons et al. 1999) is approximated by bulk nuclear matter comprised of protons, neutrons, and electrons. However, the central density of the protoneutron star at bounce reaches only about twice nuclear density and the hadron population may only develop later, after the very dynamical postbounce phases. At the low temperature border of nuclear statistical equilibrium, the equation of state is connected to a Boltzmann gas of silicon atoms. In any of these cases, once the density and temperature are given, the composition is fully determined by the specification of the electron fraction Y_e .

Matter is connected to the neutrino radiation field by weak interactions. We consider neutrinos of all three flavors and assume that they are massless. The weak interactions enter the collision term in the Boltzmann equation as energy- and angle-dependent emissivities, opacities, and scattering kernels. We include the set specified by (Bruenn 1985): (i) electron-type neutrino absorption on neutrons, (ii) electron antineutrino absorption on protons, (iii) electron-type neutrino absorption on nuclei, (iv) neutrino-nucleon scattering, (v) coherent scattering of neutrinos on nuclei, (vi) neutrino-electron scattering, and (vii) neutrino production from electron/positron pair annihilation. These reactions, and their inverses, are implemented in our code as described by Mezzacappa & Bruenn (1993b,c); Messer (2000). In the following code description, we will only include emissivities, j , and opacities, χ , because this is sufficient to describe how the collision term enters the transport and hydrodynamics equations. In the simulations, the scattering kernels are included in the collision integral as well.

The particles treated by the equation of state are assumed to react with each other on

very short time scales such that a description in terms of an instantaneous equilibrium is appropriate. Neutrinos in high-density regimes can also achieve local thermal and weak equilibrium with matter if the opacities are sufficiently high. Unlike the equilibrium with respect to the strong interaction, however, this equilibrium must be determined within our solution of the transport equation. For example, in the protoneutron star at densities above 10^{12} g cm^{-3} and temperatures above 5×10^{10} K the neutrinos are trapped and are well-described by a Fermi-gas in thermal equilibrium with the fluid. At lower densities, the thermalization time scale becomes longer; then the neutrinos can propagate with a nonequilibrium spectrum throughout these regions, to be absorbed elsewhere or leave the star. The strong coupling of the neutrinos to the matter at high densities and the strong coupling between different locations mediated by neutrino transport complicates the evolution of a numerical solution. If the problem is separated into independently updated pieces by operator splitting, the numerical solution will only be stable if information in the numerical implementation is shared faster between the independent updates than in the evaluated physical processes. The fast time scale of neutrino-matter interactions and the propagation of neutrinos at light speed may severely restrict the time step. The required coupling can be built directly into the numerical scheme by an implicit finite differencing of essential parts of the transport equation. Unfortunately, such a differencing requires knowledge of the derivatives of the collision term with respect to all independent state variables—i.e., density, temperature, electron fraction, and neutrino distribution functions. Because the emissivities, opacities, and scattering kernels strongly depend on the neutrino energies and, in the scattering case, on the neutrino propagation directions, the numerical evaluation of the collision term and its derivatives becomes a nonnegligible part of the overall computational effort. Mezzacappa & Bruenn (1993a) developed a storage scheme that allows the reuse of previously calculated emissivities, opacities, and scattering kernels by linear interpolation within a dynamical table in the independent variables of logarithmic density, $\log_{10}(\rho)$, logarithmic temperature, $\log_{10}(T)$, and electron fraction, Y_e . If one uses these same independent variables in the implicit formulation of the Boltzmann equation, the correct partial derivatives of the reactions directly emerge from the coefficients of the linear interpolation, without additional computational effort. On the one hand, the reuse of previously evaluated interactions is straightforward if the transport equation is solved in the rest frame of the fluid, such that no transformation of the neutrino energy or angle dependence of the interactions is required. On the other hand, the transport equations are simpler in the laboratory frame. In this paper we demonstrate that in the case of spherical symmetry the complexity of the transport equation is manageable and proceed with the analysis in a comoving frame (spacetime coordinates and neutrino four-momentum) to take advantage of the simplifications in the collision term. On average, we have to evaluate new collision integrals in about two to three zones per time step (out of a hundred zones). Although these numbers depend very much on the specific phase of

the simulation, the evaluation of nuclear physics input may still take about half of the total execution time.

2.2. Radiation hydrodynamics in spherical symmetry

Many spherically symmetric simulations of compact objects have been approached in comoving orthogonal coordinates (Misner & Sharp 1964; May & White 1966). Finite difference schemes of varying complexity were designed in (May & White 1967; Van Riper 1979; Bruenn 1985; Rezzolla & Miller 1994; Swesty 1995; Liebendörfer, Rosswog & Thielemann 2002), culminating in an approximate Riemann solver (Yamada 1997). The left-hand side of the Einstein field equation, the Einstein tensor, is based on the metric

$$ds^2 = -\alpha^2 dt^2 + \left(\frac{r'}{\Gamma}\right)^2 da^2 + r^2 (d\vartheta^2 + \sin^2 \vartheta d\varphi^2), \quad (1)$$

where r is the areal radius and a is a label corresponding to an enclosed rest mass (the prime denotes a derivative with respect to a : $r' = \partial r / \partial a$). The proper time lapse of a comoving observer is related to the coordinate time dt by the lapse function α . We have made the substitution $g_{aa} = r'/\Gamma$, based on a function $\Gamma(t, a)$, for the space-space component of the metric. The angles ϑ and φ describe a two-sphere. We use natural units such that the velocity of light, c , and the gravitational constant, G , become 1.

The right-hand side of the Einstein equations is given by the fluid- and radiation stress-energy tensor, T . In a comoving orthonormal basis, it has the components (Lindquist 1966)

$$\begin{aligned} T^{tt} &= \rho(1 + e + J) \\ T^{ta} = T^{at} &= H \\ T^{aa} &= p + \rho K \\ T^{\vartheta\vartheta} = T^{\varphi\varphi} &= p + \frac{1}{2}\rho(J - K). \end{aligned} \quad (2)$$

The total energy is expressed in terms of the rest mass density, ρ , the specific internal fluid energy, e , and the specific radiation energy, J . The isotropic fluid pressure is denoted by p , and the radiation stress is composed from the zeroth (J) and second (K) angular moments of the radiation intensity. Radial net energy transport is accounted for by the nondiagonal component of the stress-energy tensor, the first angular moment (H) of the specific radiation intensity.

We define a velocity u , equivalent to the r component of the fluid four-velocity as observed from a frame at constant areal radius r (May & White 1967), and identify the

total energy enclosed in a sphere with the gravitational mass, m . In the special relativistic limit, $\Gamma = \sqrt{1 + u^2 - 2m/r}$ then becomes the Lorentz factor corresponding to the boost between inertial and comoving observers. As in nonrelativistic hydrodynamics we can define a specific volume, $1/D$, specific energy, τ , and specific radial momentum, S , by

$$\frac{1}{D} = \frac{\Gamma}{\rho} \quad (3)$$

$$\tau = \Gamma(e + J) + \frac{2}{\Gamma + 1} \left(\frac{1}{2}u^2 - \frac{m}{r} \right) + uH \quad (4)$$

$$S = u(1 + e + J) + \Gamma H. \quad (5)$$

It has been shown in (Liebendörfer, Mezzacappa, & Thielemann 2001) that these definitions lead to conservation equations (6)-(8) that are analogous to the continuity equation, the conservation of total energy, and the conservation of radial momentum⁷:

$$\frac{\partial}{\partial t} \left[\frac{1}{D} \right] = \frac{\partial}{\partial a} [4\pi r^2 \alpha u] \quad (6)$$

$$\frac{\partial \tau}{\partial t} = -\frac{\partial}{\partial a} [4\pi r^2 \alpha (up + u\rho K + \Gamma\rho H)] \quad (7)$$

$$\begin{aligned} \frac{\partial S}{\partial t} &= -\frac{\partial}{\partial a} [4\pi r^2 \alpha (\Gamma p + \Gamma\rho K + u\rho H)] \\ &- \frac{\alpha}{r} \left[\left(1 + e + \frac{3p}{\rho} + J + 3K \right) \frac{m}{r} - \left(1 - \frac{2m}{r} \right) (J - 3K) \right. \\ &\quad \left. + 8\pi r^2 ((1 + e + J)(p + \rho K) - \rho H^2) - 2 \left(\frac{p}{\rho} + K \right) \right] \end{aligned} \quad (8)$$

$$\frac{\partial V}{\partial a} = \frac{1}{D} \quad (9)$$

$$\frac{\partial m}{\partial a} = 1 + \tau \quad (10)$$

$$\frac{\partial}{\partial t} \left[\frac{1}{4\pi r^2 \rho} H \right] = -(1 + e + J) \frac{\partial \alpha}{\partial a} - \frac{1}{\rho} \frac{\partial}{\partial a} [\alpha (p + \rho K)] + \frac{\alpha}{3VD} (J - 3K). \quad (11)$$

The change of the specific volume in Eq. (6) is given by the balance in the displacement of the zone boundaries. The rate of change of total energy in Eq. (7) is determined by the

⁷This reference unnecessarily assumes an isotropic radiation stress. However, we note that the difference between the full stress-energy tensor (2) and the isotropic approximation has exactly the same form as the artificial viscosity tensor introduced in the same reference to numerically stabilize shock fronts. Hence, in all derivations in the above reference we may simply use the pressure $\tilde{p} = p + \rho J/3$ for the isotropic part and set the viscosity coefficient, Q , to $\tilde{Q} = -\rho(J/3 - K)$, in order to obtain a description of radiation hydrodynamics that extends to the case where large radiation energies do not satisfy $J \not\approx 3K$.

surface luminosity, $L = 4\pi r^2 \rho H$, and the work on the surface of the mass shell against the pressure, $p + \rho K$. Of leading order in the momentum equation (8) are the pressure gradient and the gravitational force, m/r^2 . The constraints (9) and (10) are most easily understood in the Newtonian limit (the enclosed volume is defined by $V = 4\pi r^3/3$), where the first becomes the definition of the rest mass density and the second the Poisson equation for the gravitational potential. The time derivative in equation (11) is very small; therefore, this equation essentially acts as a constraint on the lapse function, α . This equation derives from the space component of the four-divergence of the stress-energy tensor. In addition to the evolution of the total energy, we also need an equation for the evolution of the internal energy that we may derive from the time component of the four-divergence of the stress-energy tensor:

$$\frac{\partial}{\partial t} [e + J] = -\frac{1}{\alpha} [4\pi r^2 \alpha^2 \rho H] - (p + \rho K) \frac{\partial}{\partial t} \left(\frac{1}{\rho} \right) - \frac{\alpha u}{r} (J - 3K). \quad (12)$$

Next, we detail the description of the radiation field. We identify the energy flux ρH with a particle flux that is determined by a Boltzmann transport equation. The transport equation is split into a left-hand side and a right-hand side. The left-hand side is the directional derivative of the particle distribution function along trajectories of free particle propagation. This derivative is equated to the changes in the distribution function due to collisions, which are described by the right hand side of the equation. Once a 1+1 decomposition of space-time (Arnowitt, Deser & Misner 1962; Smarr & York 1978) and a basis in the momentum phase space for the particle four-momentum have been chosen, the directional derivative along the phase flow can be expressed in terms of partial derivatives of the distribution function with respect to the space-time coordinates and momenta (Lindquist 1966; Mezzacappa & Matzner 1989). We measure the particle four-momentum in a comoving orthonormal frame, with components

$$p^a = p \cos \theta, \quad p^\theta = p \sin \theta \cos \phi, \quad p^\varphi = p \sin \theta \sin \phi. \quad (13)$$

In spherical symmetry, the particle energy, E , measured in a comoving frame, and the cosine of the angle between the particle momentum and the radial direction, $\mu = \cos \theta$, completely describe the particle phase space. The neutrinos are assumed to have no mass. In spherical symmetry, the distribution function does not depend on the three-momentum azimuth angle ϕ . Thus, the specific particle distribution function depends on four arguments and describes the number of particles at a given time, t , in the phase space volume $E^2 dE d\mu da$ by

$$dN = F(t, a, \mu, E) E^2 dE d\mu da. \quad (14)$$

With the metric of Eq. (1), the Boltzmann equation reads (Yamada, Janka, & Suzuki 1999; Liebendörfer, Mezzacappa, & Thielemann 2001),

$$C_t + D_a + D_\mu + D_E + O_\mu + O_E = C_c, \quad (15)$$

with

$$C_t = \frac{\partial F}{\alpha \partial t} \quad (16)$$

$$D_a = \frac{\mu}{\alpha} \frac{\partial}{\partial a} [4\pi r^2 \alpha \rho F] \quad (17)$$

$$D_\mu = \Gamma \left(\frac{1}{r} - \frac{1}{\alpha} \frac{\partial \alpha}{\partial r} \right) \frac{\partial}{\partial \mu} [(1 - \mu^2) F] \quad (18)$$

$$D_E = -\mu \Gamma \frac{1}{\alpha} \frac{\partial \alpha}{\partial r} \frac{1}{E^2} \frac{\partial}{\partial E} [E^3 F] \quad (19)$$

$$O_E = \left(\mu^2 \left(\frac{\partial \ln \rho}{\alpha \partial t} + \frac{3u}{r} \right) - \frac{u}{r} \right) \frac{1}{E^2} \frac{\partial}{\partial E} [E^3 F] \quad (20)$$

$$O_\mu = \left(\frac{\partial \ln \rho}{\alpha \partial t} + \frac{3u}{r} \right) \frac{\partial}{\partial \mu} [\mu (1 - \mu^2) F] \quad (21)$$

$$C_c = \frac{j}{\rho} - \chi F. \quad (22)$$

The source on the right-hand side, C_c , is the collision term that describes changes in the particle distribution function due to local interactions with matter. It is represented here by an emissivity j and an opacity χ . All other terms stem from the partial derivatives of the distribution function with respect to the phase-space coordinates in the directional derivative along the phase flow. They can all be physically interpreted. The first term on the left hand side of the equation, C_t , is the temporal change of the particle distribution function. The second term, D_a , counts the particles that are propagating into or out of an infinitesimal mass shell. The third term, D_μ , accounts for the change in the neutrino distribution function in an angle interval owing to the propagation of the neutrinos along geodesics with changing local angle cosine μ . The curved particle trajectories in general relativity are accounted for by the term proportional to the gradient of the gravitational potential, Φ ,

$$\frac{1}{\alpha} \frac{\partial \alpha}{\partial r} = \frac{\partial \Phi}{\partial r}.$$

The fourth term, D_E , expresses the redshift or blueshift of the particle energy that applies when the particles have a velocity component in the radial direction ($\mu \neq 0$) and, therefore, change their position in the gravitational well. The fifth and sixth term, O_E and O_μ , account for the Doppler shift and the angular aberration between adjacent comoving observers.

The integration of the Boltzmann equation over momentum space, spanned by the particle direction cosine and energy, gives the local conservation laws for particle number and energy. We define J^N and H^N to represent the zeroth and first μ moments of the

distribution function:

$$\begin{aligned} J^N &= \int_{-1}^1 \int_0^\infty F E^2 dE d\mu, \\ H^N &= \int_{-1}^1 \int_0^\infty F E^2 dE \mu d\mu. \end{aligned} \quad (23)$$

Integration of Eq. (15) over μ and E with E^2 as the measure of integration gives the following evolution equation for J^N :

$$\frac{\partial J^N}{\partial t} + \frac{\partial}{\partial a} [4\pi r^2 \alpha \rho H^N] - \alpha \int \frac{j}{\rho} E^2 dE d\mu + \alpha \int \chi F E^2 dE d\mu = 0. \quad (24)$$

The derivatives with respect to the momentum phase space in Eq. (15) do not contribute because $(1 - \mu^2)$ vanishes at $\mu = \pm 1$ and $E^3 F$ is zero for $E = 0$ and $E = \infty$. Eq. (24) is a continuity equation analogous to Eq. (6), extended by source and sink terms for the radiation particles. One more integration over the rest mass a from the center of the star to its surface gives the evolution equation of the total particle number.

Slightly less straightforward is the derivation of total radiation energy conservation. We define the energy moments

$$\begin{aligned} J &= \int F E^3 dE d\mu \\ H &= \int F E^3 dE \mu d\mu \\ K &= \int F E^3 dE \mu^2 d\mu \\ Q &= \int F E^3 dE \mu^3 d\mu \end{aligned} \quad (25)$$

and evaluate the evolution of the radiation energy as measured by an observer at infinity,

$$\frac{\partial}{\partial t} \int (\Gamma + u\mu) F E^3 dE d\mu. \quad (26)$$

To this purpose, we integrate Eq. (15) again over phase space, but this time with measure of integration $(\Gamma + u\mu) E^3$. After performing some integrations by parts to account for the time and space dependence of Γ and u , this leads to the concise result (Liebendörfer, Mezzacappa, & Thielemann 2001)

$$\begin{aligned} 0 &= \frac{\partial}{\partial t} (\Gamma J + uH) + \frac{\partial}{\partial a} [4\pi r^2 \alpha \rho (uK + \Gamma H)] + 4\pi r \alpha \rho \left(1 + e + \frac{p}{\rho}\right) H \\ &- \alpha \Gamma \int \left(\frac{j}{\rho} - \chi\right) E^3 dE d\mu + \alpha u \int \chi F E^3 dE \mu d\mu. \end{aligned} \quad (27)$$

Note that the conserved quantity $\Gamma J + uH$ is the radiation energy density in the frame of an observer at infinity. It is expressed in terms of the momentum moments J and H in the comoving frame. The second term describes the surface work by the radiation pressure, ρK , and the energy loss or gain due to the luminosity $L = 4\pi r^2 \rho H$ at the boundary. The third term contains a gravitational term coupling the matter enthalpy with the luminosity that we neglected in previous work (Liebendörfer, Mezzacappa, & Thielemann 2001). The source terms in Eq. (27) describe the energy exchange with matter by particle emission, absorption, and radiation stress. The omitted terms from neutrino scattering enter the equation in a similar form. Beforehand, we found that Eq. (7) describes the evolution of the total energy. Then, from the Boltzmann equation, we derived Eq. (27) for the evolution of the radiation energy. Thus, we will find a consistent equation for the evolution of the hydrodynamics part by the subtraction of Eq. (27) from Eq. (7). The result is Eq. (89) in section 3.4 where we discuss the implementation of the hydrodynamics part. The same procedure applied to other conserved quantities leads the full set of consistent hydrodynamics equations. By taking moments of the Boltzmann equation with the measures of integration $E^3(u + \Gamma\mu)$, $E^3\mu/(4\pi r^2\rho)$, and E^3 , respectively, we derive equations for the evolution of the radiation momentum, Eq. (28), a radiative contribution to the lapse function, Eq. (29), and the radiation energy in the comoving frame, Eq. (30):

$$\begin{aligned} \frac{\partial}{\partial t} [uJ + \Gamma H] &= -\frac{\partial}{\partial a} [4\pi r^2 \alpha \rho (\Gamma K + uH)] \\ &\quad - \frac{\alpha}{r} \left[(J + 3K) \frac{m}{r} - \left(1 - \frac{2m}{r} \right) (J - 3K) - 2K \right. \\ &\quad \left. + 4\pi r^2 (J(p + \rho K) + (1 + e + J)\rho K - 2\rho H^2) \right] \\ &\quad - \alpha \Gamma \int \chi F E^3 dE \mu d\mu + \alpha u \int \left(\frac{j}{\rho} - \chi F \right) E^3 dE d\mu \end{aligned} \quad (28)$$

$$\begin{aligned} \frac{\partial}{\partial t} \left[\frac{1}{4\pi r^2 \rho} H \right] &= -J \frac{\partial \alpha}{\partial a} - \frac{1}{\rho} \frac{\partial}{\partial a} [\alpha \rho K] + \frac{\alpha}{3VD} (J - 3K) \\ &\quad - \frac{1}{4\pi r^2 \rho} \int \chi F E^3 dE \mu d\mu \end{aligned} \quad (29)$$

$$\begin{aligned} \frac{\partial J}{\partial t} &= -\frac{1}{\alpha} [4\pi r^2 \alpha^2 \rho H] - \rho K \frac{\partial}{\partial t} \left(\frac{1}{\rho} \right) - \frac{\alpha u}{r} (J - 3K) \\ &\quad + \alpha \int \left(\frac{j}{\rho} - \chi F \right) E^3 dE d\mu. \end{aligned} \quad (30)$$

The subtraction of Eq. (28) from Eq. (8) leads to a hydrodynamics equation for the evolution of the momentum, Eq. (90). The subtraction of Eq. (29) from Eq. (11) leads to a hydrodynamics equation for the update of the lapse function, Eq. (94). Finally, the subtraction of Eq. (30) from Eq. (12) leads to a hydrodynamics equation for the evolution

of the internal energy, Eq. (95). We will pay attention to preserve this consistency also in our finite difference representation of the equations of radiation hydrodynamics. However, before we proceed with the technical details in section 3, we provide in the next subsection an overview of two exemplary simulation runs to complete the physical context and to illustrate the numerical challenges we face.

2.3. Neutrino transport in two representative simulations

In this section, we provide an overview of the core collapse and postbounce evolution in our models for the $13 M_{\odot}$ and $40 M_{\odot}$ stellar progenitors. These provide the physical context for the code tests in section 4. A thorough discussion of supernova physics can be found in previous reviews, e.g. in (Bethe 1990; Burrows & Young 2000; Mezzacappa & Bruenn 2000; Janka, Kifonidis & Rampp 2001). Earlier runs of the $13 M_{\odot}$ model have been described in (Mezzacappa et al. 2001; Liebendörfer et al. 2001) with Newtonian and general relativistic gravity. Here, we add information on the formation of the neutrino spectra and report on our first self-consistent simulation running all the way from core collapse to the onset of black hole formation in the case of the $40 M_{\odot}$ model. We have chosen progenitors on the light and massive side with respect to the range of potential core collapse supernova progenitors. This demonstrates the spread in the results. The results of our simulations for intermediate mass progenitors are summarized in (Messer 2000; Liebendörfer et al. 2001a, 2002). The latest was calculated with the finite differencing described in this paper.

The most prominent characterization of a supernova explosion is the trajectory of the shock position. We define the shock position as the location with the maximum infall velocity (i.e. minimum in the velocity profile). Before the shock is formed after bounce, the location with maximum infall velocity coincides with the sonic point which separates the causally connected inner core from the supersonically infalling outer core. The pressure wave emerging from the center at bounce turns at this transition point into a shock wave. The trajectory of maximum infall velocity is therefore continuous across bounce as shown in the magnifying window on the left hand side of Fig. (1). If we compare the position of the sonic point in the $13 M_{\odot}$ model with its position in the $40 M_{\odot}$ model, we find that they converge to the same point before bounce. For the explanation, we recall that the sonic point depends on the Chandrasekhar mass, which is determined by the electron fraction profile. The electron fraction profile of the two runs converges due to a strong feedback of the electron fraction on the free proton abundance (Messer et al. 2003). Within the “standard” input physics, it is assumed that electron capture on nuclei with a full neutron $f7/2$ shell is Pauli-blocked (Bruenn 1985). Under such conditions, our simulations allow

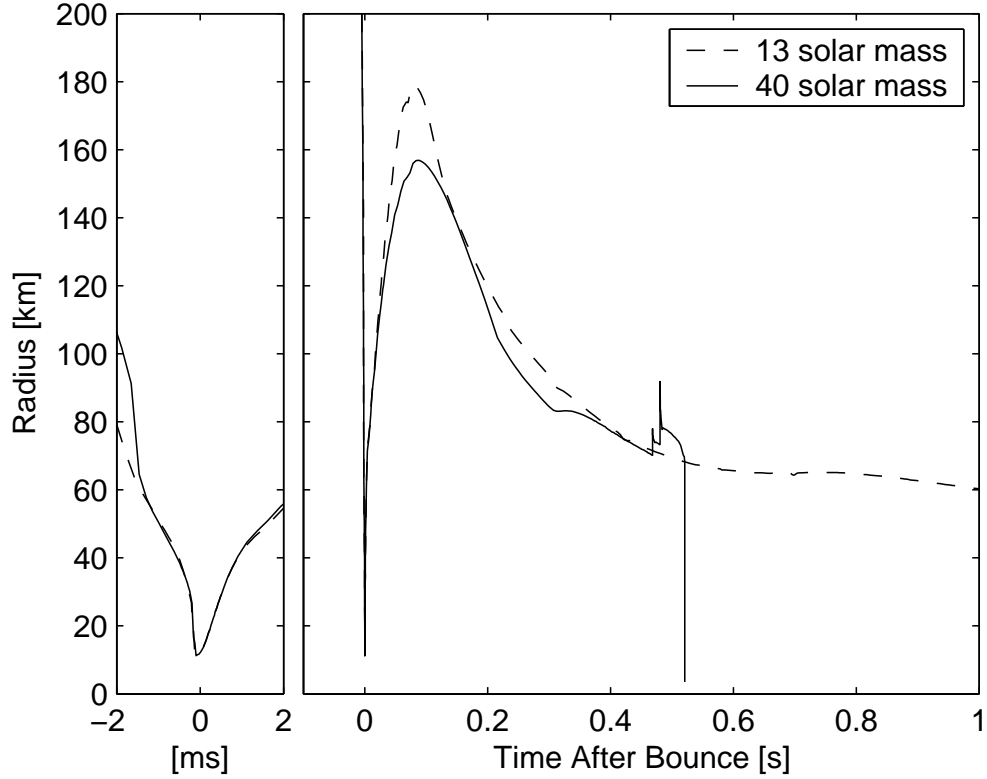


Fig. 1.— Shown are the shock trajectories of the $13 M_{\odot}$ (dashed line) and $40 M_{\odot}$ (solid line) models. At negative times, i.e. before bounce, the trajectories indicate the position of the sonic point instead of the position of the not yet formed shock wave. The left hand part of the figure zooms in on the time around bounce to demonstrate that the shock is formed at the sonic point (no discontinuity in the lines) and that this happens at the same position in both models. The right hand part shows the shock trajectories over a longer time scale. After about 500 ms, the $40 M_{\odot}$ star collapses to a black hole. The perturbation at $t_{pb} = \sim 0.3$ s is the consequence of a physical change in the luminosities. The two perturbations after $t_{pb} = \sim 0.4$ s are the result of an artificial increase of the numerical shock width we had to apply in order to run the simulations to the end.

only electron capture on free protons. Now, if the electron fraction and/or temperature in one model would only be slightly higher than in the other model, this would result in a significantly higher free proton abundance. It would cause a significantly higher number of electron captures than in the other model. Hence, the differences between the models are reduced. It has recently been shown that, due to the finite temperature in the nuclei and due to correlations, electron capture on nuclei dominates electron capture on free protons throughout core collapse (Langanke et al. 2003). It will be interesting to see if the described feedback will to the same extent be at work with these more realistic electron capture rates. We can only expect this if the electron capture on low abundance nuclei would turn out to be comparable to, or larger than, the electron capture on the most abundant nuclei (the quantity to compare would of course always be the product of the electron capture rate with the abundance of the target). The right hand side of Fig. (1) shows the shock trajectories over a longer time interval, up to one second after bounce. The shocks recede in both models after $t_{pb} = 100$ ms. The conditions for a shock revival deteriorate. The intensive neutrino emission from the cooling region undermines the pressure support below the heating region and the material is drained from the latter onto the protoneutron star (Janka 2001). The transient stall in the receding shock front in the $40 M_{\odot}$ model at 0.3 s after bounce is a reaction to an enhanced electron flavor luminosity. It will be further analyzed below, together with the description of the evolution of the luminosities. In the evolution of the $40 M_{\odot}$ progenitor, we encountered a numerical stability problem after $t_{pb} = 0.4$ s. The adaptive grid created extremely small mass zones such that the convergence radius of the Newton-Raphson algorithm in the implicit hydrodynamics was severely reduced due to truncation errors. We increased the artificial viscosity in two sequential steps to widen the shock and continue the run. This numerical shock widening is responsible for the outward steps in the shock position ~ 0.5 s after bounce. Shortly after the collapse of the protoneutron star to a black hole has set in, our code crashes unavoidably because of the coordinate singularity in the comoving coordinates at the Schwarzschild horizon. We will extensively use the hydrodynamic profiles at 0.4 s after bounce for testing in later subsections.

The neutrino luminosities and rms energies are shown in Fig. (2). The electron neutrino luminosities rise during core collapse and reach a level of 10^{53} erg/s. The collapse is halted at nuclear densities and a bounce shock propagates outwards through neutrino opaque material. The neutrino luminosity decays to a 30% lower level during this short period of ~ 4 ms duration. It has been assigned to a decrease in the free proton fraction when the shock is formed (Thompson, Burrows, & Pinto 2003). Additionally, while the shock is running out to the neutrinospheres, it condenses previously still neutrino emitting material to even more neutrino opaque densities. When the shock reaches the electron neutrinosphere, an electron neutrino burst with a peak height of 3.5×10^{53} erg/s is launched by copious electron capture.

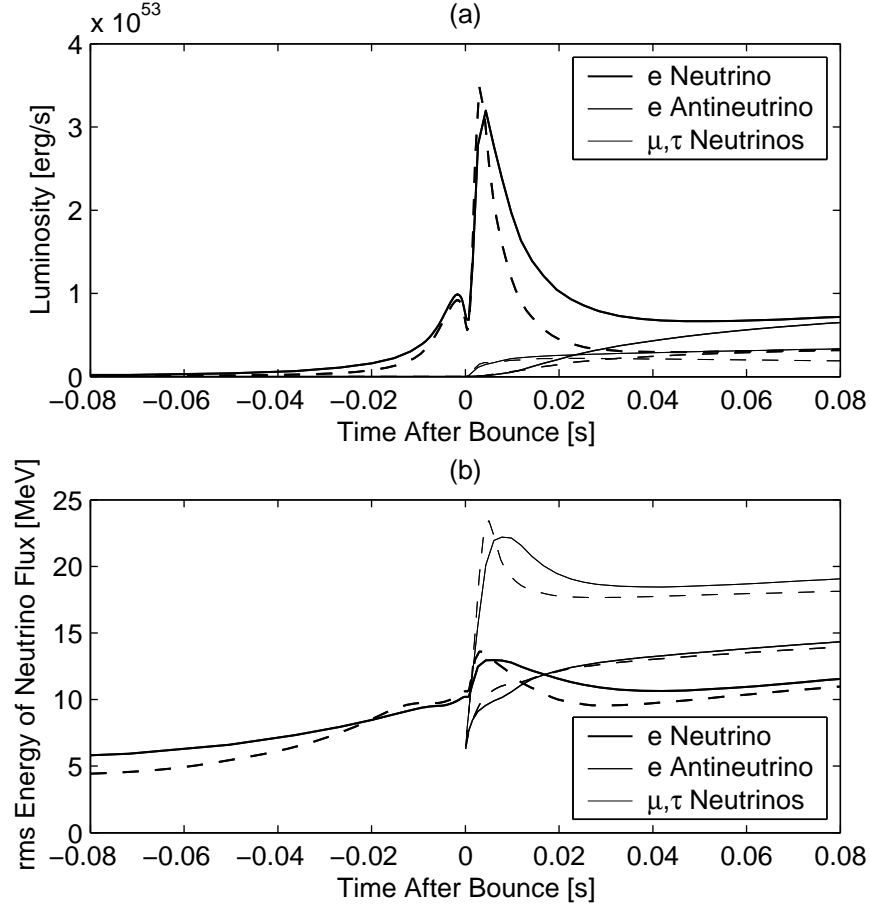


Fig. 2.— The luminosities and rms energies of the neutrinos are shown as a function of time. The results of the 13 M_{\odot} model are drawn with dashed lines and the results of the 40 M_{\odot} model with solid lines. A thick line belongs to the electron neutrino, a line with medium width to the electron antineutrino, and a thin line to the μ - and τ -neutrinos. We sampled the luminosities at a radius of 500 km. Also the rms energy of the neutrino flux (not abundance) was calculated at this location. We adjusted the time coordinate by $\Delta t = -500 \text{ km}/c$ to account for the (approximate) propagation time to the sampling radius. The two progenitors show a comparable neutrino burst with a peak height of 3.5×10^{53} erg/s. Significant differences appear in later phases. The variations in the density profiles in the outer layers of the two models determine the accretion-dominated electron flavor luminosities.

As the neutrinos escape quickly, the freed phase space is refilled with new neutrinos and the matter deleptonizes rapidly. This phase is very similar in both models because, after core collapse, the structure of the inner core is so similar. Differences appear later, when the accretion luminosity dominates over the core diffusion luminosity with a ratio of about 2 : 1 to 3 : 1. The higher densities in the outer layers of the more massive progenitor produce considerably higher accretion luminosities when they settle in the gravitational potential on the surface of the protoneutron star. The rising electron neutrino rms energies before bounce reflect the conditions in the compactifying material at infall. After the neutrino burst, the rms energies adjust to the spectrum set by the shock heated mantle and reflect the conditions at the location of decoupling. However, we have to keep in mind that the location of decoupling strongly varies for individual neutrino flavors and neutrino energies. Thus, the rms energy rather reflects an emission-weighted sampling of conditions at different locations. Quite generally, the μ and τ neutrinos decouple deeper because of the insensitivity of these neutrinos to charged current reactions. The electron antineutrinos decouple deeper than the electron neutrinos because of the smaller proton than neutron abundance.

In order to investigate the origin of the neutrino luminosities in more detail, we introduce in appendix B radius- and energy-dependent attenuation coefficients, $\xi(r, E)$, that express the probability that a neutrino with energy E emitted at radius r escapes from the computational domain without a reaction that changes its type or energy. The attenuation coefficients carry information that is similar to the optical depth, $\tau(r, E)$: $\xi(r, E) \simeq \exp(-\tau(r, E))$. However, their evaluation according to Eq. (B5) is fully consistent with the finite differencing of the Boltzmann equation and takes the variations in the local flux factors into account. Assume for example, we investigate a reaction ℓ that produces at radius r neutrinos in the energy interval dE with an energy emissivity $E^3 j^\ell(r, E) dE$. With the help of the attenuation coefficients, we can quantify the contribution of a given volume element $4\pi r^2 dr$ to the total luminosity,

$$g^\ell(r, E) dE dr = \xi(r, E) j^\ell(r, E) E^3 dE 4\pi r^2 dr.$$

The total neutrino luminosity of a given neutrino type is then given by the integral of $g^\ell(r, E)$ over energy and position for all reactions that contribute,

$$L = \sum_\ell \int dr \int g^\ell(r, E) dE.$$

We demonstrate in appendix B that the attenuation coefficients in Eq. (B5) represent the total luminosity in the simulation accurately. In the following figures, we cumulatively plot the quantity $g^\ell(r, E) \Delta E$ in units of erg/s/km. It is natural to choose ΔE in accordance with the width of the $k_{\max} = 12$ energy groups we used in the simulations. At the bottom of the figure we start with the electron or positron capture reaction (depending on the neutrino

type). We draw $g^{\text{capt}}(r, E_1) \Delta E_1$ for the lowest energy group and enclose it by a black line. On top of it, we add $g^{\text{capt}}(r, E_2) \Delta E_2$ for the next energy group, again enclosed by a black line. The shading of the enclosed areas indicates the energy group according to the legend at the bottom of the figure. Energy groups that do not contribute collapse to a single line with zero enclosed area. On top of $g^{\text{capt}}(r, E_{k_{\text{max}}}) \Delta E_{k_{\text{max}}}$ we continue with $g^{\text{pair}}(r, E_1) \Delta E_1$ for the pair creation reaction. We enclose this and the following area elements by a white line to distinguish them from the electron or positron capture reactions. After the addition of $g^{\text{pair}}(r, E_{k_{\text{max}}}) \Delta E_{k_{\text{max}}}$, we continue with the contributions from neutrino-electron scattering, i.e. $g^{\text{scat}}(r, E_1) \Delta E_1$ to $g^{\text{scat}}(r, E_{k_{\text{max}}}) \Delta E_{k_{\text{max}}}$. We use again black lines as separators for the neutrino-electron scattering. The figures become intuitively accessible as soon as one realizes that the total shaded area is proportional to the total luminosity of the star. The total area of a specific energy shading is proportional to the contribution to the total luminosity of neutrinos from the corresponding energy group. The total area of a specific reaction is proportional to the contribution to the total luminosity of neutrinos with this last inelastic interaction before the escape. A cross section through the shaded area at a given radius tells about the spectrum of the neutrinos escaping from that region, and about the probability of the reaction type they had at that position before the escape. In order to characterize also the extent of isoenergetic scattering of neutrinos off nucleons and nuclei, we mark the neutrinospheres for the energy groups at the top of the figure. The energies are rising from the left to the right according to the legend at the bottom of the figure. For the interpretation of the figures it is also useful to know the thermodynamical conditions at the locations the neutrinos are emitted. For each density decade we set a marker at the bottom of the figure. Additionally, we include the electron fraction in the graph with the electron neutrino analysis, and the entropy in the graph with the electron antineutrino analysis. The solid line represents the profile in the simulation, the dashed line represents the equilibrium value that would be achieved by infinitely long exposure of the stationary fluid element to the prevailing neutrino abundances. Finally, the graph with the μ - and τ -neutrino analysis obtains profiles with the temperature (dashed line) and electron chemical potential (solid line).

Fig. (3), for example, shows a snapshot at 5 ms before bounce in the collapse of the 13 M_{\odot} progenitor. Neutrinos are escaping from the range between 20 km and 200 km radius, roughly corresponding to a density range of 10^{10} g/cm^3 to 10^{12} g/cm^3 . The electron fraction profile (solid line) reflects the deleptonization that has already occurred in the more interior regions where Y_e approaches values around 0.3. The equilibrium value (dashed line) is still lower, indicating that the deleptonization is ongoing and that the deleptonization time scale is slightly slower than the dynamical time scale. The pair process does not contribute in this collapse phase of high electron degeneracy. The corresponding area collapses to one

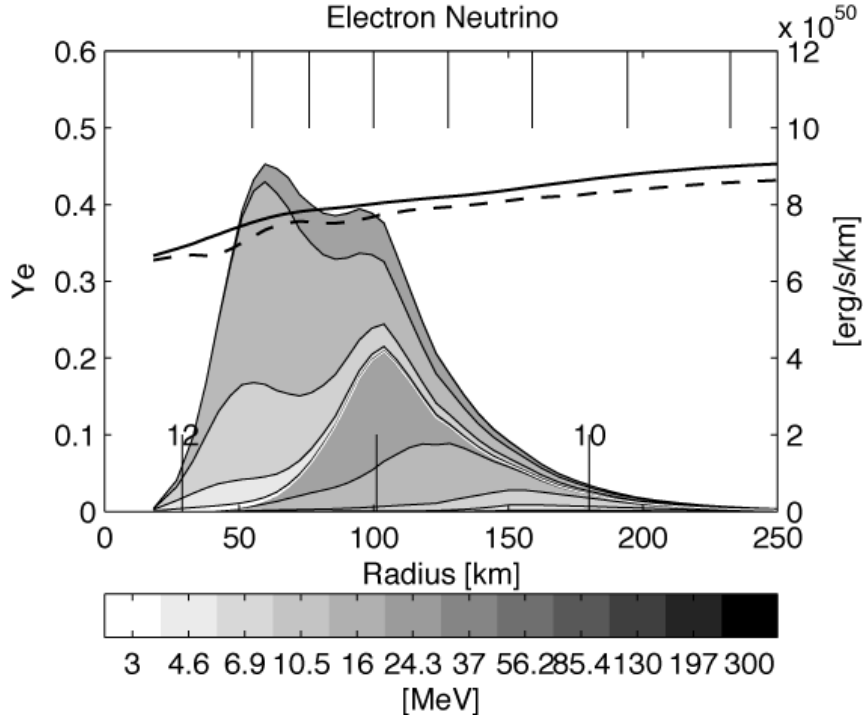


Fig. 3.— The last inelastic interactions of escaping neutrinos at 5 ms before bounce in the $13 M_{\odot}$ model. The abscissa of the graph is the radius, ranging from the center of the star to 250 km radius. The density markers at the bottom of the graph indicate the position of density decades, $\log_{10}(\rho)$, where ρ is given in g/cm^3 . The thick solid line shows the electron fraction profile. The thick dashed line shows the electron fraction in weak equilibrium under otherwise unchanged conditions (same density, temperature, neutrino abundances, and spectra). These quantities belong to the ordinate at the left hand side. The total shaded area in the graph corresponds to the total electron neutrino luminosity at 5 ms before bounce in units of erg/s . The appropriate ordinate on the right hand side then carries the units $\text{erg}/\text{s}/\text{km}$. The shaded area is divided into three sections, according to the type of the last energy-changing reaction of the escaping neutrinos. Segments separated by black lines in the lower part of the shaded area outline the contribution of electron captures to the escaping neutrinos. The contribution from pair production is bordered by white lines. The contribution from neutrino-electron scattering is shown in the upper part of the shaded area, once more bordered by black lines. As there are no contributions from pair production in the cool and electron-degenerate material at 5 ms before bounce, the section belonging to the pair production reaction collapses to a white line between the electron capture section and the neutrino-electron scattering section. The contribution for each reaction is further subdivided into contributions from each energy group in the simulation. The intensity of the shading identifies the neutrino energy according to the legend at the bottom of the figure. Each energy group has its own neutrinosphere at optical depth $\tau = 2/3$. Their locations, marked in the upper part of the figure, statistically indicate the positions of the last interaction of the neutrinos with matter, isoenergetic scattering included. The energies rise from the left to the right according to the legend. The transient undulations in the luminosity contributions in this phase are a numerical artefact caused by the low resolution of the Fermi surface in

white line in the graph that separates the electron capture contributions below it from the neutrino-electron scattering contributions above it. Almost no neutrinos escape directly after an electron capture at a radius as small as 50 km. Neutrinos escaping from this region are thermalized by scattering off electrons. They escape with quite low energies. Around 100 km radius we find that about half of the escaping neutrinos stem directly from electron capture, while the other half has scattered off an electron. At 150 km $\sim 2/3$ of the neutrinos escape without further electron-scattering. Among the neutrinos produced by electron capture, the neutrinos with higher energies escape from smaller radii than the neutrinos with lower energies. In this collapse phase, the “standard” input physics only includes electron captures on free nucleons. The Q value of the reaction is small and very few low energy neutrinos are directly produced if the electron chemical potential is large (e.g. 17 MeV at 100 km radius in this time slice). The escaping low energy neutrinos have scattered off electrons. However, the larger Q value of more realistic electron capture rates on neutron-rich nuclei may shift the energy of directly escaping neutrinos to lower values such that the count of direct escapes is increased (Langanke et al. 2003). Finally, we remark that the neutrinos in a given energy group are produced at a significantly smaller radius than the location of the corresponding transport sphere. This is the result of the dominance of the isoenergetic scattering cross section in the collapse phase. The diffusive propagation of the neutrinos extends to much lower densities than neutrino-electron scattering or neutrino absorption.

We switch to the next interesting phase: the electron neutrino burst at ~ 5 ms after bounce (Fig. 4). While the region of neutrino emission during core collapse was very broad, it is extremely narrow (~ 10 km) in the burst phase. In the neutrino burst, the electron neutrinos escape directly from electron capture. Some neutrino-electron scattering does occur in front of the shock in an earlier stage and inelastic scattering of burst neutrinos on nuclei in front of the shock are possible (Bruenn & Haxton 1991), but not included in the standard input physics. Only the energy groups at 10.5 MeV and 16 MeV contribute significantly to the burst. This is in good agreement with the position of the corresponding transport sphere in the upper part of the figure (fourth and fifth from the left, respectively). The density is of order 10^{11} g/cm³. The trapped electron neutrinos inside the region of main emission are in weak (and thermal) equilibrium with the fluid. This is evident in the congruence of the electron fraction profile (solid line) with the equilibrium Y_e (dashed line).

The situation at 50 ms after bounce is shown in Fig. (5). This is the phase where neutrino heating starts to set in. All luminosities are fully developed at this time. Graph (a) reveals electron capture as the almost exclusive source of electron neutrinos. The higher energy neutrinos emerge from larger radii. The isoenergetic scattering cross sections are comparable to the neutrino absorption cross sections. Thus, the regions of emission for the different energy groups are nicely centered around the corresponding transport sphere.

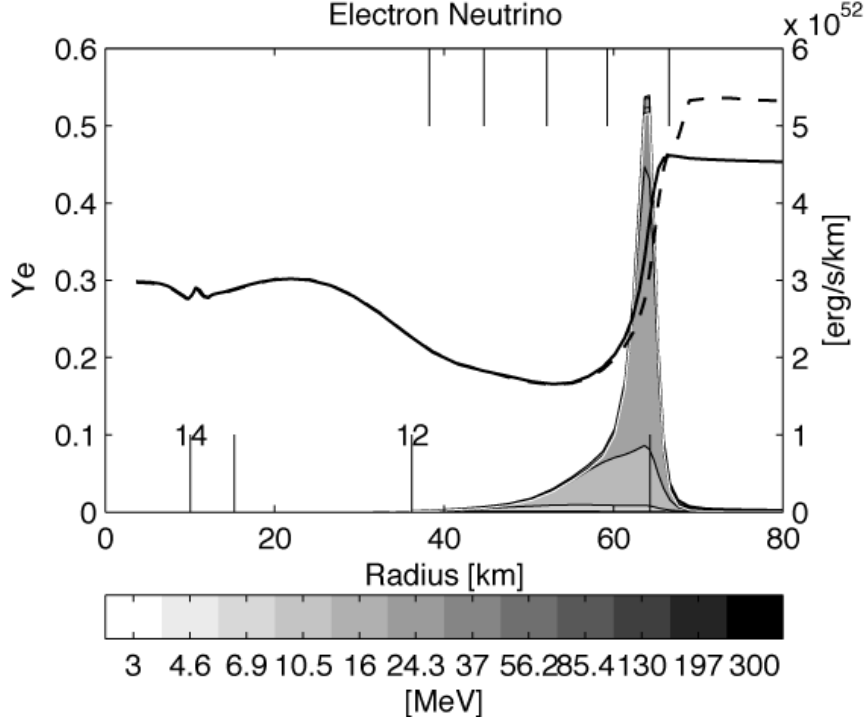


Fig. 4.— The last inelastic interactions of escaping neutrinos at 5 ms after bounce in the 13 M_{\odot} model. The abscissa of the graph is the radius, ranging from the center of the star to 80 km radius. The density markers at the bottom of the graph indicate the position of density decades, $\log_{10}(\rho)$, where ρ is given in g/cm^3 . The thick solid line shows the electron fraction profile. The thick dashed line shows the electron fraction in weak equilibrium under otherwise unchanged conditions (same density, temperature, neutrino abundances, and spectra). These quantities belong to the ordinate at the left hand side. The total shaded area in the graph corresponds to the total electron neutrino luminosity at 5 ms after bounce in units of erg/s . The appropriate ordinate on the right hand side then carries the units $\text{erg}/\text{s}/\text{km}$. Note that the scale is 50 times larger than in Fig. (3). In this phase, almost all neutrinos escape directly after their production by electron capture on free protons (area below the white line). The emission of the neutrino burst occurs from a very narrow radius interval. This causes a steep drop in the electron fraction at the same position. The subdivision of the burst into different energy groups also shows a narrow energy spectrum of the emitted neutrinos. Inside 50 km radius, the trapped neutrinos are in weak equilibrium with the matter. In the burst region, the deleptonization time scale is only slightly slower than the shock propagation. Outside the shock front, it is much slower because of the low abundance of free protons.

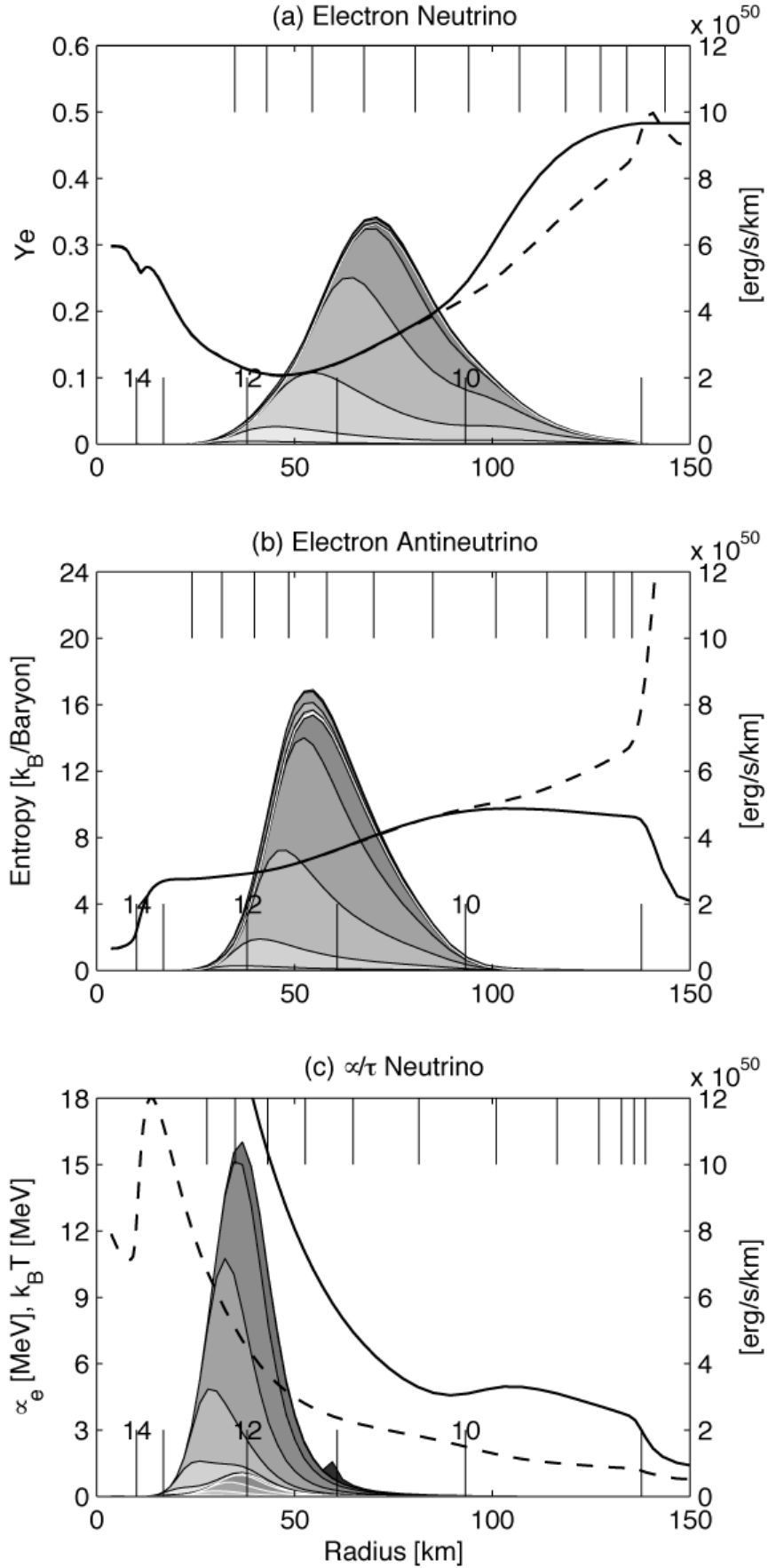


Fig. 5.— The last inelastic interactions of escaping neutrinos at 50 ms after bounce in the $13 M_{\odot}$ model. The abscissa of the graph is the radius, ranging from the center of the star to 150 km radius. The density markers at the bottom of the graph indicate the position of density decades, $\log_{10}(\rho)$, where ρ is given in g/cm^3 . The thick solid line in graph (a) shows the electron fraction profile. In graph (b) it is the entropy profile, and in graph (c) the electron chemical potential. The thick dashed line gives the equilibrium Y_e in graph (a), the equilibrium entropy in graph (b), and the temperature profile in graph (c). We do not repeat the detailed explanation of the differently shaded and separated areas indicating the energy- and reaction-specific contribution of neutrino emissivities to the total luminosity of the star. Instead, we refer to the caption of Fig. (3) or to the explanation given in the text. Graph (a) shows the origin of escaping electron neutrinos. Only electron capture contributes significantly (area below the white line). By definition, the region of neutrino emission coincides with the cooling region where the fluid is in weak equilibrium with the neutrino abundances. In the heating region, between the cooling region and the shock front at 140 km radius, the reaction time scales are comparable to, or larger than, the infall time scale. Graph (b) shows the origin of the electron antineutrino luminosity. The electron antineutrinos are emitted from a slightly smaller radius. The contribution of electron-scattered neutrinos (above the white line) is also slightly larger than for the electron neutrinos. By following the entropy profile from the right to the left (as an infalling fluid element would experience it) we find the expected abrupt entropy increase at the shock position. Behind the shock, the fluid element would drift more slowly inwards and neutrino absorption indeed leads to a small increase of the entropy in the region between 140 km and ~ 100 km radius. However, the equilibrium entropy is declining towards smaller radii such that cooling becomes unavoidable once the fluid entropy has joined the equilibrium entropy in a still infalling state. Graph (c) shows the origin of the μ - and τ -luminosities. Almost no neutrinos escape directly from pair creation (area enclosed by white lines at the bottom of the figure). Most of the neutrinos have scattered off electrons before their escape (area enclosed by black lines).

The continued deleptonization after the neutrino burst caused a rather broad trough in the electron fraction profile. The region of neutrino emission coincides with the cooling region where the fluid is in weak equilibrium with the neutrino abundances. In the heating region, between the cooling region and the shock front at 140 km radius, the reaction time scales are comparable to, or larger than, the infall time scale. Graph (b) shows the origin of the electron antineutrino luminosity. The electron antineutrinos are emitted from a slightly smaller radius at densities exceeding 10^{11} g/cm³ (while they were similar to 10^{11} g/cm³ for the electron neutrinos). The electron antineutrinos decouple at smaller radii because of the higher neutron than proton abundance. The contribution of electron-scattered neutrinos (above the white line) is slightly larger than in the case of the electron neutrinos. The pair production process does not noticeably contribute to the luminosity at this stage. The equilibrium entropy (dashed line) is increasing with increasing radius. An infalling fluid element changes its entropy rather slowly by electron capture until it hits the accretion shock. At the shock front, most of its kinetic energy is converted into heat by shock dissipation. The heavy nuclei are dissociated, mainly into free nucleons which are good neutrino absorbers. However, before the stage at 50 ms after bounce, the entropy of an infalling fluid element has already reached or exceeded the equilibrium entropy, alone by shock dissipation. Only cooling is then possible during the continued infall. After $t_{pb} \sim 50$ ms, however, the equilibrium entropy is not reached by the shock dissipation and the fluid element indeed increases its entropy towards the equilibrium by neutrino absorption during its flight through the heating region (solid line in graph (b) ~ 120 km radius). As the fluid element also tends to decrease the electron fraction (graph (a)), electron antineutrinos are preferentially absorbed. Once the equilibrium is reached, cooling becomes unavoidable if the fluid element is still infalling because the reaction rates at these densities are faster than the dynamical infall time. Convection in the heating region is expected to increase the neutrino heating efficiency (see e.g. the parameter study of Janka & Müller (1996)), but not included in our simulations. We did not find any sign of shock revival in spherical symmetry with the included input physics. Graph (c) shows the origin of the μ - and τ -luminosities. The μ - and τ -neutrinos are produced at an average density slightly larger than 10^{12} g/cm³. Almost no neutrinos escape directly from pair creation (area enclosed by white lines at the bottom of the figure). Most of the neutrinos have scattered off electrons before their escape (area enclosed by black lines). Pair production is not the dominant source of μ - and τ -neutrinos. It has been shown, that the production from bremsstrahlung (Thompson, Burrows, & Horvath 2000) and from electron flavor neutrino annihilation (Buras et al. 2003a) exceeds the pair process production rate (both reactions are not included in our simulations). The latter reference finds that the μ - and τ -neutrino luminosities show differences of 10%–20% in the first 100 ms after bounce and converge to the standard luminosities afterwards. The spectra are not significantly different. This finding is also supported by our graph (c): The production site of the μ - and τ -neutrinos

is at a much smaller radius than their transport sphere. Hence, the neutrino luminosity is set by the (though energy-dependent) diffusivity between the location of neutrino production and the transport sphere. Moreover, graph (c) shows that the majority of escaping neutrinos scattered off electrons in their last reaction. Differences in the production-spectrum are likely to be washed out during the thermalization the neutrinos are experiencing while they are diffusing outwards to the transport sphere.

Finally, we present the situation at 500 ms after bounce in Fig. (6). This is after a long quasi-stationary phase of matter accretion and shock recession. The volume of neutrino emitting material has considerably shrunk with respect to the situation at 50 ms after bounce. But there are not much qualitative changes. The neutrinos with larger energies still escape from larger radii because of the corresponding staggering of the transport spheres in the steep density gradient at the surface of the protoneutron star. The shock has receded to a radius of 57 km. Graph (b) shows the origin of the electron antineutrino luminosity. The infalling fluid elements are now crossing the heating region that rapidly (with several thousand km/s) that there is no time for significant neutrino heating. This can be seen in the flat top of the entropy curve between 30 km and 50 km radius (solid line). Even the cooling sets in with a slight delay and thermal balance is only reached at densities larger than 10^{11} g/cm³. Graph (c) shows the origin of the μ - and τ -luminosities. Still very few neutrinos escape directly from pair creation (area enclosed by white lines at the bottom of the figure). Most of the neutrinos have scattered off electrons before their escape (area enclosed by black lines). The continued cooling by μ - and τ -neutrino emission becomes now clearly visible in the entropy profile at a radius of 18 km, where an entropy dip develops. At larger radii, however, between 25 km and the shock position, the temperature is rising and the electrons have become nondegenerate. The overlap of this material with the emission region of electron antineutrinos in graph (b) lets the emission of higher energy antineutrinos shift to lower densities than before.

Figure (7) shows the luminosities and rms energies of the neutrino flux after bounce on a longer time scale. In the $13 M_{\odot}$ model, the luminosities decrease as a consequence of the declining accretion rate and continued deleptonization of the core. The electron flavor luminosities reach very similar values because the lifted electron degeneracy in a large part of the cooling region (see Fig. (6bc)) allows the electrons and positrons to be captured from similar chemical potentials. The luminosities are higher than the luminosities of the μ - and τ -neutrinos because the latter do not have an accretion luminosity component. The rms energies show the usual hierarchy at the beginning, but after $t_{pb} = 0.7$ s, the rms energy of the μ - and τ -neutrinos falls below the rms energy of the electron antineutrino. This is also understood if one looks again at Fig. (6bc). While the emission of high energy electron antineutrinos is aided by shock-heated material settling at the base of the cooling region

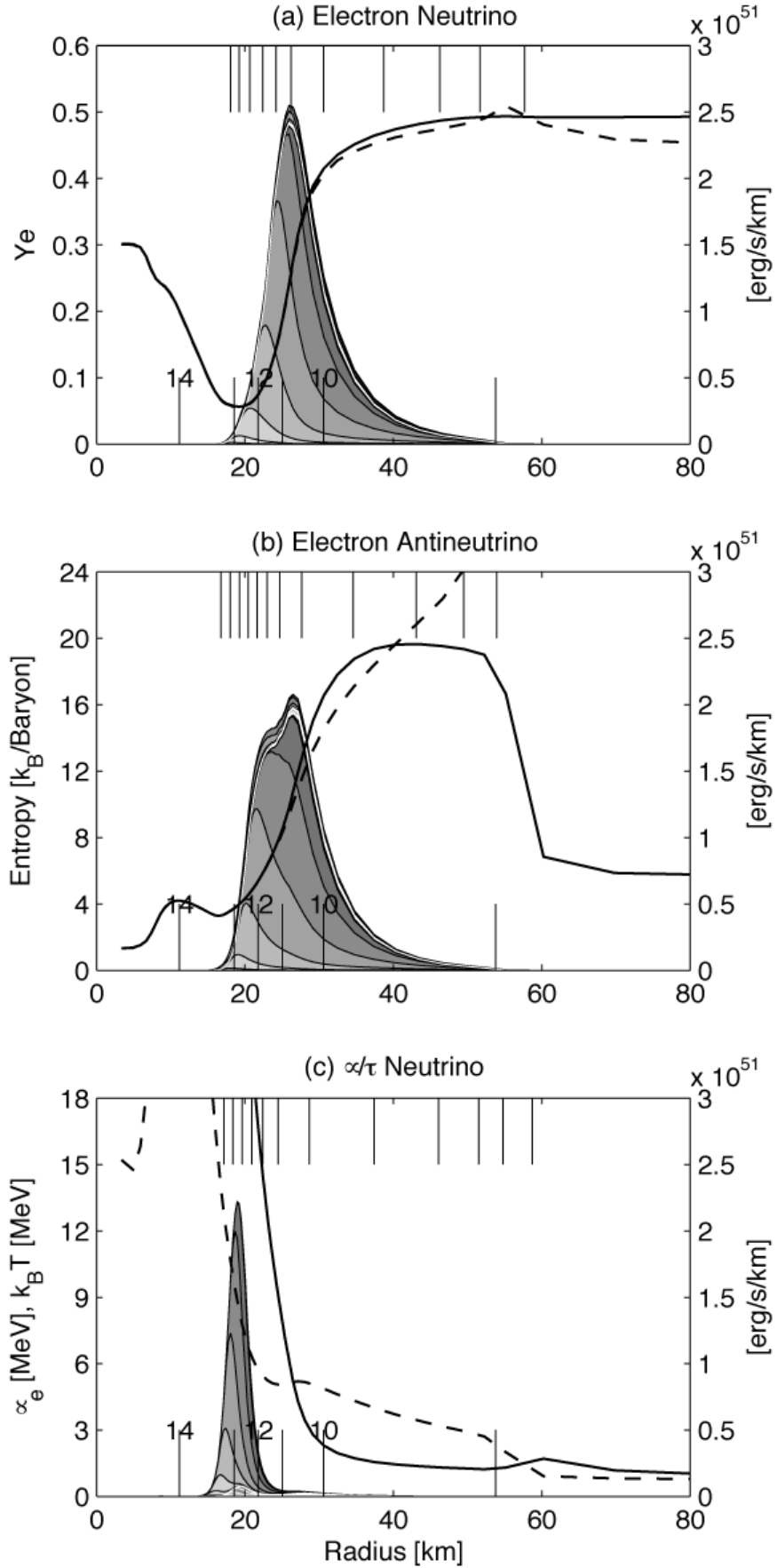


Fig. 6.— The last inelastic interactions of escaping neutrinos at 500 ms after bounce in the $13 M_{\odot}$ model. The abscissa of the graph is the radius, ranging from the center of the star to 80 km radius. The density markers at the bottom of the graph indicate the position of density decades, $\log_{10}(\rho)$, where ρ is given in g/cm^3 . The thick solid line in graph (a) shows the electron fraction profile. In graph (b) it is the entropy profile, and in graph (c) the electron chemical potential. The thick dashed line gives the equilibrium Y_e in graph (a), the equilibrium entropy in graph (b), and the temperature profile in graph (c). We do not repeat the detailed explanation of the differently shaded and separated areas indicating the energy- and reaction-specific contribution of neutrino emissivities to the total luminosity of the star. Instead, we refer to the caption of Fig. (3) or to the explanation given in the text. Graph (a) shows the origin of escaping electron neutrinos. Only electron capture contributes significantly (area below the white line). Neutrinos with larger energies still escape from larger radii because of the corresponding staggering of the transport spheres at the top of the figure. The shock has receded to a radius of 57 km and all regions are more compact. Graph (b) shows the origin of the electron antineutrino luminosity. The accreted fluid elements fall rapidly through the heating region without significant neutrino heating. Graph (c) shows the origin of the μ - and τ -luminosities. Still very few neutrinos escape directly from pair creation (area enclosed by white lines at the bottom of the figure). Most of the neutrinos have scattered off electrons before their escape (area enclosed by black lines). The continued cooling by μ - and τ -neutrino emission becomes now visible in the entropy profile at a radius of 18 km. At larger radii, however, between 25 km and the shock position, the temperature is rising and the electrons are nondegenerate. The overlap of this material with the emission region of electron antineutrinos in graph (b) enhances the emission of higher energy antineutrinos.

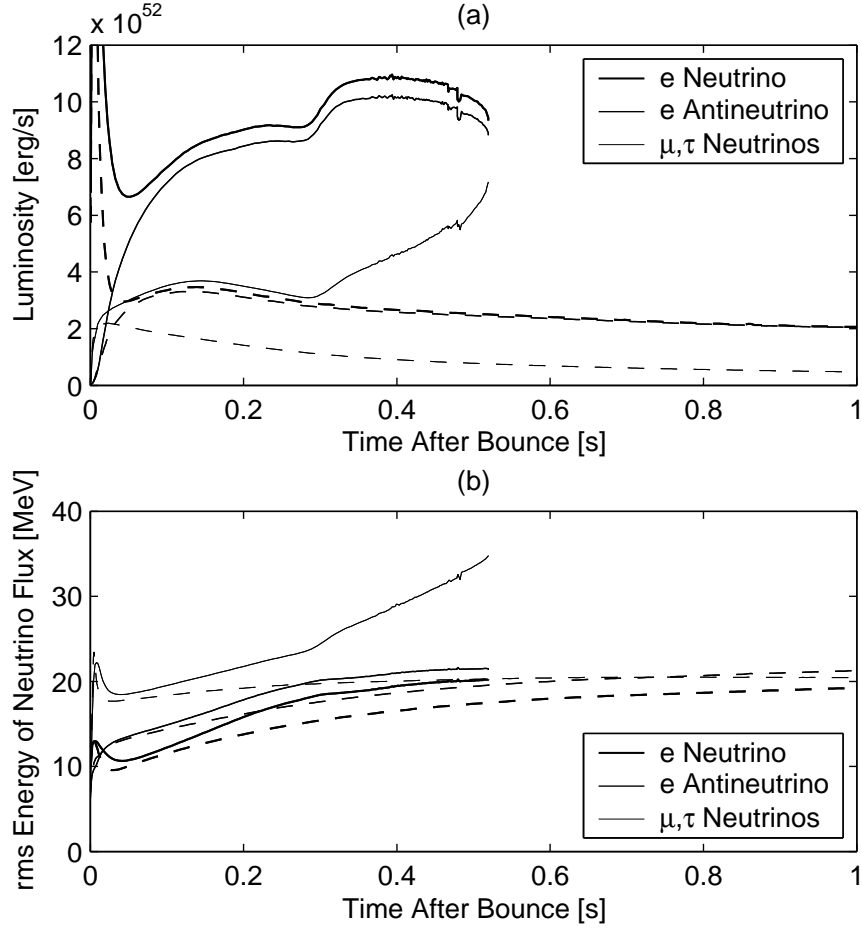


Fig. 7.— The luminosities and rms energies in the two models are shown on a longer time scale. In the 13 M_{\odot} model (dashed lines), the electron neutrino luminosity (thick line) and electron antineutrino luminosity (medium width line) converge. Both are much larger than the μ - and τ -neutrino luminosities (thin line) because of the contribution from the accretion luminosity. The rms energies show the conventional hierarchy at the beginning. However, at 0.7 s after bounce, the rms energy of the μ - and τ -neutrino luminosity falls below the rms energy of the electron antineutrinos. This is due to the fact that this low mass protoneutron star is quite incompressible with respect to the accumulated mass at the given accretion rate. The continued emission of μ - and τ -neutrinos cools the deep layers (around $r = 18$ km in Fig. (6)) independently from the dynamics of the outer layers. This is different in the 40 M_{\odot} mass model (solid lines). The protoneutron star comes closer to its maximum mass at 0.3 s after bounce such that it contracts appreciably with continued accretion. An increase in the accretion rates lets the electron flavor neutrinos step up. The accelerated transition from a mass accumulating stiff central object to a contracting compressible core affects the μ - and τ -neutrino properties. Shock-heated material is faster condensed to higher densities and the luminosities and rms energies of the μ - and τ -neutrinos start to rise continuously until the protoneutron star collapses to a black hole at ~ 0.5 s after bounce.

with moderate electron degeneracy, the layers around 18 km radius, i.e. where the energy spectra of the μ - and τ -neutrinos are set, are barely affected by the continued accretion on the still not very massive protoneutron star. This domain just slowly cools by neutrino emission (compare the entropy profiles in Fig. (5b) and (6b)). The result are decreasing luminosities and rms energies of the μ - and τ -neutrinos. The more massive 40 M_{\odot} model shows qualitatively different features. In order to understand them, we first discuss Fig. (8). Shown are the profiles of the mass flux through surfaces at constant radii in the two models. The dashed lines show the mass flux in the 13 M_{\odot} model. Nothing special happens there, the mass flux generally decreases in accordance with the decreasing density in the outer layers. Moreover, the contraction of the stiff core, which is far from its maximum mass, is minimal. A similar evolution is visible during the first 300 ms in the 40 M_{\odot} model. However, if we examine the massflux in the 300 ms time slice in Fig. (8) more closely, we find a variation in the density profile around 1000 km that falls in (from ~ 2000 km at 100 ms after bounce). The corresponding variation in the massflux or accretion rate leads to a step in the electron flavor neutrino luminosities between 300 ms and 350 ms after bounce. The increase is of order 20%. The slope in their rms energies flattens slightly. More independent of the details of the progenitor model, however, might be that the protoneutron star in the 40 M_{\odot} model approaches its maximum mass much more rapidly because a high accretion rate is maintained when the outer layers fall in. They have a significantly larger density in comparison to the 13 M_{\odot} model. The fast mass accumulation in the 40 M_{\odot} model becomes evident in Table (1), which lists the enclosed mass at 100 km radius for different time slices in both models. As the accumulated mass in the 40 M_{\odot} protoneutron star gets closer to the maximum mass, the protoneutron star starts to contract faster by the general relativistic enhancement of the effective gravitational potential (an effect absent in Newtonian calculations). We observe in Fig. (8) that, after an initial decrease, the mass flux in the inner core is increasing again. This is by no means a “sudden” change on the short dynamical time scale of the protoneutron star. The contraction is a hydrostatic adaption to the accumulated mass in the gravitational potential. The change is, however, sudden on the time scale of the variations in the neutrino properties shown in Fig. (7). The μ - and τ -neutrino luminosities and rms energies rise steeply. This happens because, by the contraction of the protoneutron star, electron-nondegenerate shock-heated material is condensed to densities where the main emission of heavy neutrinos occurs. We investigate the conditions at the locations of the main neutrino emission in more detail in Fig. (9). We calculate the average conditions for the emission of a specific neutrino type according to Eq. (B7). Instead of the average radius, we calculate here the average density (graph (a)), temperature (graph (b)), and electron fraction (graph (c)). These represent the typical conditions where an escaping neutrino makes its last energy-changing interaction with the matter. The conditions at the origin of electron neutrino emission are traced with a solid

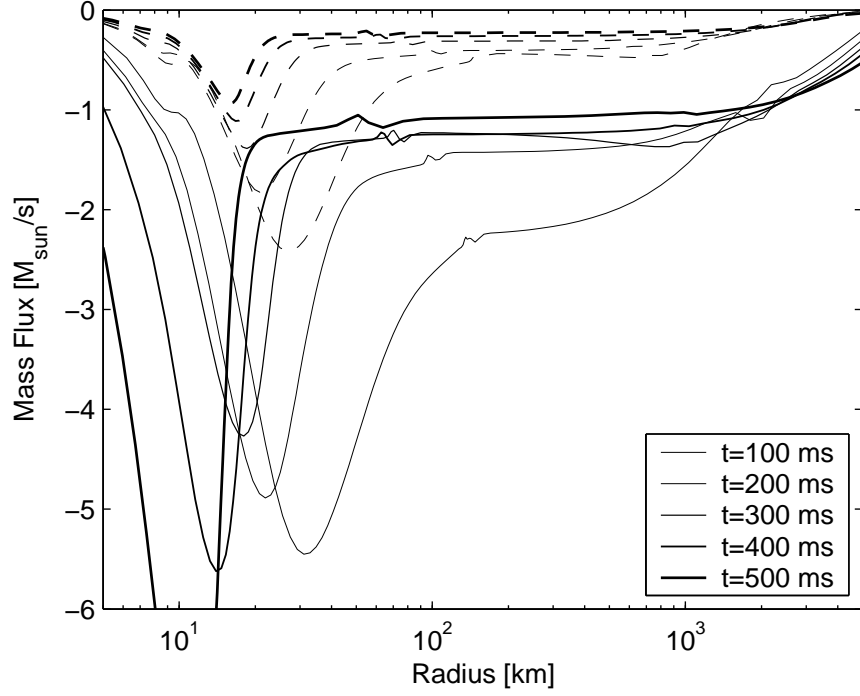
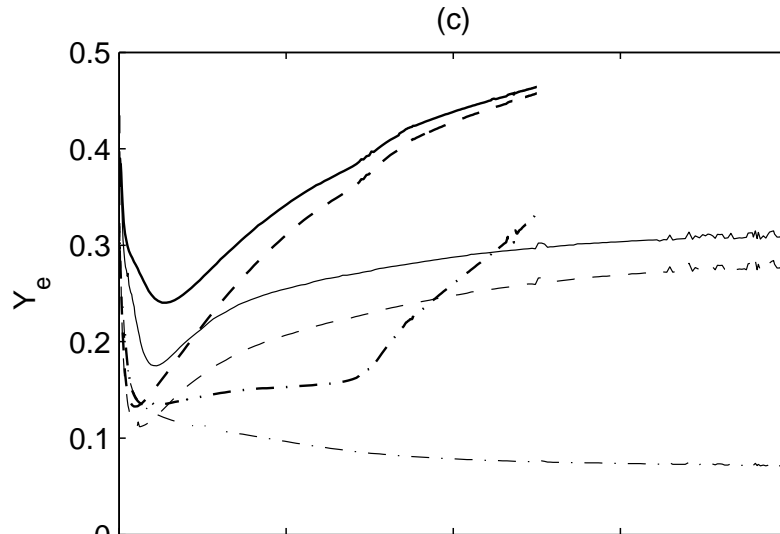
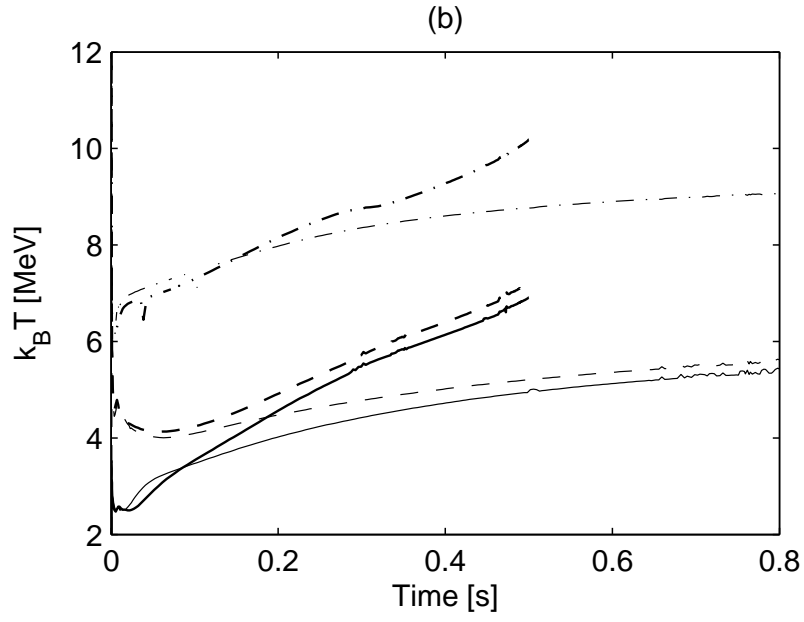
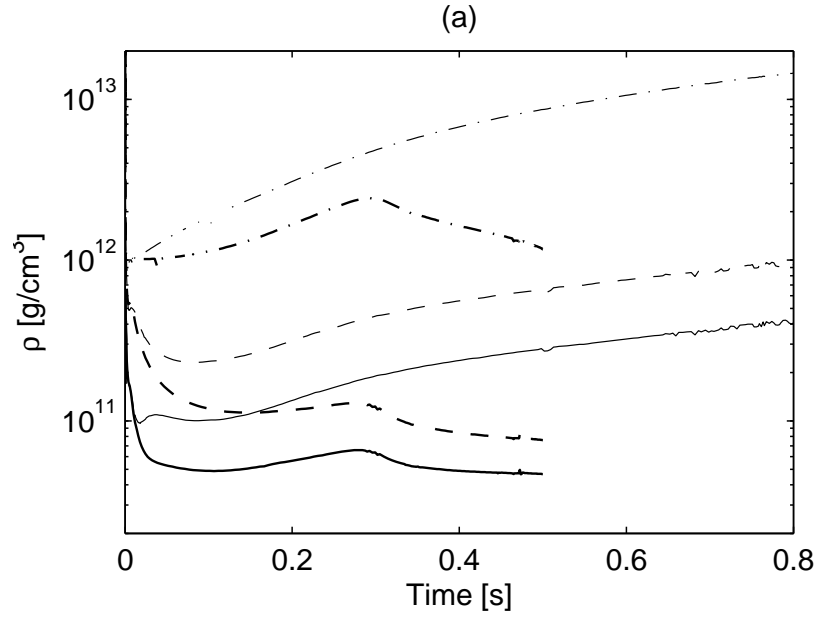


Fig. 8.— Mass flux through surfaces at constant radii in the 13 M_\odot model (dashed lines) and 40 M_\odot model (solid lines). The profiles are given at 0.1 s, 0.2 s, 0.3 s, 0.4 s, and 0.5 s after bounce. While the accreted mass piles up on the small protoneutron star in the 13 M_\odot model, it forces the massive protoneutron star in the 40 M_\odot model to hydrostatic gravitational contraction after $t_{pb} = 0.3\text{ s}$. An incoming variation in the accretion rate is visible outside of 1000 km radius.



t_{pb}	13 M_{\odot}	40 M_{\odot}
[s]	[M_{\odot}]	[M_{\odot}]
0.0	0.90	0.88
0.1	1.19	1.57
0.2	1.25	1.77
0.3	1.28	1.89
0.4	1.31	2.02
0.5	1.33	2.20
1.0	1.42	–

Table 1: Shown is the enclosed mass at a radius of 100 km as a function of time for the 13 M_{\odot} and 40 M_{\odot} model. In the 13 M_{\odot} model, the accretion rate reduces quickly and the mass of the protoneutron star does not even come close to its maximum mass during the ~ 1 s time window so far explored with Boltzmann neutrino transport. The outer layers in the 40 M_{\odot} model are much denser. The accretion rate stays high and the simulation can be performed until the protoneutron star collapses.

Fig. 9.— The thermodynamic conditions where escaping neutrinos have their last inelastic interaction are averaged with the weight of the contribution of the neutrinos to the total luminosity. Shown is the average neutrino emission density in graph (a), the average neutrino emission temperature in graph (b), and the average neutrino emission electron fraction in graph (c). Inelastic scattering of neutrinos off electrons is also included as an “emission” reaction. The typical conditions for electron neutrino emission are represented with a solid line, the typical conditions for electron antineutrino emission with a dashed line, and the typical conditions for μ - and τ -neutrino emission with a dash-dotted line. The thin lines belong to the 13 M_{\odot} model and the thick lines to the 40 M_{\odot} model. The conditions are similar at bounce. They diverge afterwards. In the 13 M_{\odot} model, the main neutrino emission recedes to higher densities during the evolution of the simulation. In the 40 M_{\odot} model, the main neutrino emission turns back to lower densities after gravitational contraction sets in at 300 ms after bounce. The emission from the gravitationally compressed shock-heated matter at moderate densities competes more successfully with the emission from the cooler core at higher densities.

line, the conditions at the origin of electron antineutrino emission with a dashed line, and the conditions at the origin of μ - and τ -neutrino emission with a dash-dotted line. We discuss first the $13 M_{\odot}$ model (thin lines). After an initial decrease up to the time of maximum neutrino heating around 100 ms after bounce, the average density at the sites of neutrino production increases steadily. This goes along with a temperature increase for all neutrino types. At least in the case of the very temperature-sensitive pair production rates for the μ - and τ -neutrinos, however, the argumentation should be turned around: Because the temperature at a given density is slowly decreasing on the long time scale, the emission from lower density regions decreases and the average emission conditions shift to increasingly deeper layers, where the temperatures are higher. Graph (c) shows that the electron fraction at the place of emission is increasing for the electron flavor neutrinos. This is due to the rather high electron fraction in the shock-heated material behind the shock front, where the electron degeneracy is gradually lifted. The μ - and τ -neutrinos escape from the floor in the electron fraction profile, which is steadily decreasing by continued deleptonization. This is reflected in the declining electron fraction at the location of the production of heavy neutrinos in graph (c). The contraction of the protoneutron star in the $40 M_{\odot}$ model causes a qualitatively different characterization of the regions of main neutrino emission. The temperature increase by adiabatic compression is no longer fully balanced by neutrino cooling. The temperature at a given density starts to increase. The domain of the shock-heated material where the electrons are non-degenerate reaches down to deeper layers close to the place where the μ - and τ -neutrinos are produced. The temperature increase makes these regions to significantly more efficient μ - and τ -neutrino emitters such that the average emission density starts to decrease. In spite of this steep density decrease in graph (a), the temperature in graph (b) still increases at the average emission condition. The electron fraction in graph (c) rises dramatically as the mean neutrino emission region moves out of the Y_e trough in the electron fraction profile. As the production site of heavy neutrinos moves outwards to lower densities, the fraction of directly escaping neutrinos (without neutrino-electron scattering) also increases. Additionally, the forming “density cliff” shortens the escape path for few high energy μ - and τ -neutrinos that may leave the star without thermalization. It can be expected that the not included reactions of μ - and τ -flavor neutrino production by bremsstrahlung and electron flavor neutrino annihilation will more significantly influence the μ - and τ -neutrino spectra in this less opaque density regimes. Unfortunately, we cannot follow the evolution beyond the collapse of the protoneutron star because of the coordinate singularity at the formation of the Schwarzschild horizon. However, the neutrino luminosities are expected to decay on a short timescale (see e.g. (Baumgarte et al. 1996)).

3. Numerical Implementation

In this section we motivate and describe our finite difference representation of spherically symmetric radiation hydrodynamics in numerical computations. The continuous equations of radiation hydrodynamics are unique. But the number of possible finite difference representations is large. We select ours according to the following requirements (with descending priority):

1. In the limit of high resolution, the finite difference representation should converge to the continuous equations.
2. The finite difference representation should lead to a numerically stable solution.
3. The finite difference representation should not be less accurate than simpler schemes in regions where simpler schemes are sufficient.
4. The computed evolution of the particle distribution function should imply an accurate evolution of expectation values like the particle density or the average particle energy.

In our discrete ordinates (S_N) method, we discretize the full transport equation at once. This takes care of requirement (1). In the first place, we choose the finite differencing such that the numerical scheme is stable according to requirement (2). Moreover, we adjust it such that requirement (3) is met with respect to the important diffusion limit. In the finite differencing of the free streaming limit, we focus on accurate particle number luminosities and accurate particle energy luminosities. The accuracy of the angular moments of the radiation field is less essential in this domain because the neutrinos cannot contribute to the supernova mechanism in regions far outside the neutrinospheres. More accurate angular information in the free streaming limit with the S_N method would require a very large number of angular bins, an adaptive grid in angle space (Yamada, Janka, & Suzuki 1999), or a postprocessing step with a ray-tracing tool. All remaining degrees of freedom in the choice of the finite difference representation are used to optimize requirement (4). Of course, point (1) already guarantees that requirement (4) will successfully be approached if the resolution is sufficiently high. However, as we solve the transport equation at once, and with an implicit finite difference representation, resolution is computationally rather expensive. In the spirit of requirement (3), high resolution may only be required where the very details of the complete transport equation are relevant for the physical solution. In order to make low resolution results reliable, important physical laws must be represented accurately independent of the resolution setting. This includes the challenge of conserving lepton number and total energy in the simulations. Indeed, one might say that the power of a specific implementation of the

S_N method is given by the extent to which requirements (3) and (4) can be satisfied at low resolution.

A variable Eddington factor method (VEF) is a different numerical approach than the S_N method. There, requirements (2), (3), and (4) are satisfied by construction. A series of simpler radiation moment equations are solved and combined with an Eddington factor to produce the solution to the equations of radiation hydrodynamics. The quality of the variable Eddington factor method is determined by the capability to meet requirement (1). It depends on the interplay between the different moment equations and the accuracy of the Eddington factor (which may require the numerical solution of a model Boltzmann equation (Burrows et al. 2000; Rampp & Janka 2002; Thompson, Burrows, & Pinto 2003)). With careful implementation, both methods should fulfill requirements (1)-(4) and therefore lead to similar results (Liebendörfer et al. 2003).

3.1. Conservation Laws and Expectation Value Matching

In the S_N approach, the complete dynamics in the phase space of the transported particles is determined by *one* kinetic equation (15). Its integration over the momentum phase space is equivalent to a continuity equation (24), its integration weighed with particle energies, ε , is equivalent to an energy equation (27), and its integration weighed with the particle direction cosine and energy would lead to a momentum equation. These derived equations certainly fulfill the macroscopic conservation laws as given in Eq. (7). But it is a challenge to obtain the same level of consistency in a finite difference representation of the Boltzmann equation. We illustrate this with the following little example:

For simplicity we assume that a distribution function, $f(t, x)$, of particles propagating with speed c only depends on time, t , and on one dimension in the phase space, x . The simplest form of a transport equation would then relate the time derivative of the distribution function to an advection term,

$$\frac{\partial f}{\partial t} + c \frac{\partial f}{\partial x} = 0. \quad (31)$$

If we now ask for the time evolution of the expectation value of the distribution function with respect to an operator, $g(t, x)$, we apply integrations by parts to find

$$\frac{\partial}{\partial t} \int g f dx = \int \left(\frac{\partial g}{\partial t} + \frac{\partial g}{\partial x} \right) f dx - [g f]_{\partial x}. \quad (32)$$

Here, the time evolution of the expectation value is described by other expectation values and the value of $g f$ at the boundary of the domain of integration. This equation has an immediate physical interpretation: The change of the expectation value along the characteristics of the

particle flow is simply given by the change of the weight along the characteristics of the particle flow because the phase space volume stays constant,

$$\left(\frac{\partial}{c\partial t} + \frac{\partial}{\partial x}\right) \int g f dx = \int \left(\frac{\partial g}{c\partial t} + \frac{\partial g}{\partial x}\right) f dx. \quad (33)$$

The second term on the left hand side is equivalent to the boundary term $-[gf]_{\partial x}$ in Eq. (32). Let us now assume that numerical stability requires upwind differencing of the advection term in Eq. (31), and, for simplicity, that the wind is unidirectional. A finite difference representation would then read like

$$\frac{\partial f_{i'}}{\partial t} + c \frac{f_{i'} - f_{i'-1}}{dx_{i'}} = 0. \quad (34)$$

We use the convention that a prime at the index points to the zone center value $i + 1/2$ while an integer index i points to the zone edge. We simplify the example once more and assume that the operator g is not time-dependent. With this, we track above integration by parts in the finite difference representation and calculate the evolution of the expectation value of operator $g(x)$,

$$\begin{aligned} \frac{\partial}{c\partial t} \sum_{i=1}^n g_{i'} f_{i'} dx_{i'} &= \sum_{i=1}^n g_{i'} \frac{\partial f_{i'}}{c\partial t} dx_{i'} = - \sum_{i=1}^n g_{i'} (f_{i'} - f_{i'-1}) \\ &= - \sum_{i=1}^n g_{i'} f_{i'} + \sum_{i=0}^{n-1} g_{i'+1} f_{i'} \\ &= \sum_{i=1}^n \frac{g_{i'+1} - g_{i'}}{dx_{i'}} f_{i'} dx_{i'} - [g_{n'+1} f_{n'} - g_{0'+1} f_{0'}]. \end{aligned} \quad (35)$$

Firstly, we remark that there is a discrete analogue to the integration by parts and that Eq. (35) has exactly the same structure as Eq. (32). Secondly, we note that the choice of finite differencing for the advection term in Eq. (34) determines the finite differencing of the weight function $(g_{i'+1} - g_{i'})/dx_{i'}$ in the expectation value on the right hand side of Eq. (35). In the following, we will frequently use this type of investigation to optimize for requirements (3) and (4): First we choose a stable finite difference representation of a term in the transport equation. Then we evaluate relevant expectation values by performing discrete “integrations by parts”, analogously to this simple example. The emerging finite difference representations of the expectation values along one phase space dimension are then used as prefactors for the finite differencing of terms related to other phase space dimensions in order to build a consistent finite difference representation of the full transport equation.

In order to construct a conservative finite difference representation of Eq. (15), we analyze the structure of the conservation equations in the continuum world, where insight

is not buried in discretization indices. The emergence of lepton number conservation in Eq. (24) is straightforward, because the observer corrections are already written in a form that allows an immediate integration over energy or the angle cosine. Number conservation will also emerge naturally in the finite difference representation when we finite difference the same basic structure of the equation. The energy conservation equation in the frame of a distant observer, however, introduces the weight $g(t, a, \mu, E) = E(\Gamma + u\mu)$ in Eq. (26). It depends on all four phase space dimensions and leads to the contribution of several expectation values of the distribution function in the evaluation of the energy conservation equation,

$$\int (\Gamma + u\mu) E [C_t + D_a + D_\mu + D_E + O_E + O_\mu - C_c] d\mu E^2 dE = 0. \quad (36)$$

All terms in the Boltzmann equation (15), C_t , D_a , D_μ , D_E , O_E , and O_μ , are written as the derivative of an expression with respect to time, rest mass, angle cosine, or particle energy. We now perform an integration by parts with respect to these integration variables x along the lines of Eq. (32). A multitude of correction terms proportional to $\partial(\Gamma + u\mu)E/\partial x$ arise. As in Eq. (33), they describe the evolution of the weight $g(t, x) = (\Gamma + u\mu)E$ along the characteristic of the particle flow. However, we showed in (Liebendörfer, Mezzacappa, & Thielemann 2001) that $(\Gamma + u\mu)E$ is nearly a constant of motion along the characteristics. Therefore, it is natural that most of the partial terms $\partial(\Gamma + u\mu)E/\partial x$ actually cancel in the total evolution of the radiation energy in the frame of a distant observer. If, like in Eq. (35), the integrations by parts are also carefully followed in the finite difference representation, mutual cancellations of important expectation values can be forced to be exact—independently of the resolution. Because these canceling terms individually reach large values around and after bounce, this expectation value matching is an essential step for the conservation of energy in the finite difference representation. We perform the integrations by parts in Eq. (36) and start with the identification of canceling contributions in the following overview of contributions from C_t , D_a , D_μ , D_E , O_E , O_μ , C_c in the transport equation (15):

$$\begin{aligned} C_t : & \quad \frac{\partial}{\alpha \partial t} (\Gamma J) - \frac{\partial \Gamma}{\alpha \partial t} J + \frac{\partial}{\alpha \partial t} (uH) - \frac{\partial u}{\alpha \partial t} H \\ D_a : & \quad \frac{\partial}{\alpha \partial a} [4\pi r^2 \alpha \rho \Gamma H] - 4\pi r^2 \rho \frac{\partial \Gamma}{\partial a} H \\ & \quad + \frac{\partial}{\alpha \partial a} [4\pi r^2 \alpha \rho u K] - 4\pi r^2 \rho \frac{\partial u}{\partial a} K \\ D_\mu : & \quad -\Gamma \frac{u}{r} (J - K) + \Gamma u \frac{\partial \Phi}{\partial r} (J - K) \\ D_E : & \quad \Gamma \frac{\partial \Phi}{\partial r} (\Gamma H + uK) \end{aligned}$$

$$\begin{aligned}
O_E : \quad & - \left[\frac{\partial \ln \rho}{\alpha \partial t} + \frac{2u}{r} \right] (\Gamma K + uQ) + \Gamma \frac{u}{r} (J - K) + \frac{u^2}{r} (H - Q) \\
O_\mu : \quad & - \left[\frac{\partial \ln \rho}{\alpha \partial t} + \frac{2u}{r} \right] u (H - Q) - \frac{u^2}{r} (H - Q) \\
C_c : \quad & \Gamma \int \left(\frac{j}{\rho} - \chi F \right) E^3 dE d\mu - u \int \chi F E^3 dE d\mu.
\end{aligned} \tag{37}$$

We will neglect terms that are nonlinear in the radiation field, i.e. terms that describe a gravitational interaction of the radiation field with itself. From the hydrodynamics equations in (Misner & Sharp 1964; May & White 1966) we then derive the following useful relationships for the coefficients in Eq. (37).

$$\frac{1}{\Gamma} \frac{\partial \Gamma}{\alpha \partial t} = u \frac{\partial \Phi}{\partial r} \tag{38}$$

$$- \left(\frac{\partial \ln \rho}{\alpha \partial t} + \frac{2u}{r} \right) = \frac{4\pi r^2 \rho}{\Gamma} \frac{\partial u}{\partial a} \tag{39}$$

$$\frac{\partial u}{\alpha \partial t} = \Gamma^2 \frac{\partial \Phi}{\partial r} - \frac{m}{r^2} - 4\pi r p. \tag{40}$$

We may now identify cancellations in Eq. (37) and label them for later reference: The fourth term of D_a cancels with the first term of O_E ($D_a^4 O_E^1$) by Eq. (39). The first and second term of D_μ cancel with the third and fourth term in O_E ($D_\mu^{12} O_E^{34}$). These are the only $O(v/c)$ cancellations and therefore the most important ones. In an analogous notation, we find the following higher order cancellations: ($C_t^2 D_\mu^3$) by Eq. (38), ($D_\mu^4 D_E^2$), ($O_E^2 O_\mu^2$), ($O_E^{56} O_\mu^{34}$). The remaining terms, ($C_t^4 D_a^2 D_E^1 O_\mu^1$), reduce by Eq. (40) and the definition of Γ to the general relativistic term,

$$\left(-\frac{\partial u}{\alpha \partial t} - \Gamma \frac{\partial \Gamma}{\partial r} + \Gamma^2 \frac{\partial \Phi}{\partial r} + u \frac{\partial u}{\partial r} \right) H = 4\pi r \rho (1 + e + p/\rho) H. \tag{41}$$

They enter in this form the radiation energy conservation equation (27).

We will adopt the following strategy in the finite differencing of Eq. (15) (the reader is invited to draw lines in Eq. (37) to visualize the relationship between the different terms): (i) The finite differencing of C_t and C_c are straightforward. (ii) Appreciable experience has been gathered in previous work (see e.g. (Lewis & Miller 1984)) with the finite differencing of the $O(v/c)$ terms in D_a and D_μ . They are assumed to be well-chosen in (Mezzacappa & Bruenn 1993a) and therefore not subject to changes. (iii) Based on this, the cancellation ($D_a^4 O_E^1$) dictates the finite difference representation of $(\partial \ln \rho / \alpha \partial t + 2u/r)$ in O_E^1 and O_E^2 . The cancellation ($O_E^2 O_\mu^2$) sets the finite difference representation of $(\partial \ln \rho / \alpha \partial t + 2u/r)$ in O_μ^2 and O_μ^1 . (iv) The cancellation ($D_\mu^{12} O_E^{34}$) dictates the finite difference representation of u/r in O_E^{34} and O_E^{56} . The cancellation ($O_E^{56} O_\mu^{34}$) propagates the finite difference representation to

u/r in O_μ^{34} . (v) The evaluation of $(C_t^4 D_a^2 D_E^1 O_\mu^1)$ according to Eq. (41) constrains the finite difference representation of $\Gamma \partial \Phi / \partial r$ in D_E^1 and therewith defines D_E^2 . (vi) And finally we choose a different finite difference representation for $\Gamma u \partial \Phi / \partial r$ in D_μ^3 and D_μ^4 , as suggested by the cancellation $(C_t^2 D_\mu^{34} D_E^2)$. By these six chains, all terms in Eq. (15) become constrained.

3.2. Adaptive Grid

AGILE-BOLTZTRAN has the capability to dynamically adapt the computational grid to the evolution of the stellar profile. Each radial zone contributes to the computationally expensive implicit solution of the Boltzmann equation. The adaptive grid allows the concentration of these zones to domains where radiation transport is actually active and important. It also allows a proper shock capturing and propagation. The fundamental ideas of the dynamically adaptive grid have been developed in (Winkler, Norman, & Mihalas 1984; Dorfi & Drury 1987). The first reference describes how the continuous equations of radiation hydrodynamics are formulated on an adaptive grid and the second reference provides a numerically stable prescription how to adapt the local grid point concentration to steep gradients in the solution vector. The details of our implementation of the adaptive grid are described in (Liebendörfer, Rosswog & Thielemann 2002). Here we resume the key points and describe the extension of the approach from the hydrodynamics code AGILE to the radiation quantities.

We concentrate on observers at rest in their slice. They reside in local orthogonal reference frames which we assume to be collinear with global coordinates A . Consequently, coordinates A have vanishing shift vectors everywhere. We introduce another system of global coordinates, B , having arbitrary shift vectors on the same time slices. Let us select fixed grid labels in coordinates B : $\{q_i \in \mathbb{R}, i = 1 \dots n\}$. The fixed labels in coordinates B define a moving grid in coordinate system A : $\{a(t, q_i)\}$. The grid labels in coordinate system B cut the continuum into zones Δq on each time slice. These zones contain a time dependent selection of observers in coordinate system A : $\Delta a = \{a(t, q), q \in \Delta q\}$. We define a zone integral of the observations

$$\langle y(t, a) \rangle = \int_{\Delta a} y(t, a) da \quad (42)$$

that is based on the observations y of single observers a in the zone. In coordinate system A , the borders of the zones change with time according to the shift vectors in coordinate system B . In Newtonian parlance, one can identify the moving zones in coordinate system A with the motion of an adaptive grid. The important point is that the adaptive grid only regroups the observers into new zones. As stated already by (Winkler, Norman, & Mihalas

1984), the adaptive grid never changes the reference frame of the observations. It solely determines the width and location of a zone on the time slice for the zone-integration of the observations y in the comoving frame A .

In order to formulate time evolution equations, we are interested in the time change of the zone-integrated quantity $\langle y(t, a) \rangle$ in a specific zone Δq . Taking into account that the boundaries of the integration over Δa are time-dependent, this leads to

$$\frac{\partial}{\partial t} \int_{a(t, q_i)}^{a(t, q_{i+1})} y da = \int_{a(t, q_i)}^{a(t, q_{i+1})} \frac{dy(t, a)}{dt} da + \left[y \frac{\partial a(t, q)}{\partial t} \right]_{a(t, q_i)}^{a(t, q_{i+1})} \quad (43)$$

The notation $\partial/\partial t$ is used for time derivatives at constant grid label q while Lagrangian derivatives, d/dt , are evaluated at constant baryon mass a . The left hand term is the time change of the zone-integrated variable y between fixed grid labels in the numerically accessible coordinate system B . The first term on the right hand side is the time derivative in orthogonal coordinates A as used in the physical equations, e.g. on the left hand side of Eqs. (6)-(8). The second term on the right hand side of Eq. (43) is due to the motion of the grid. It is evaluated at the zone boundaries and accounts for the observers that fall into or drop out of the zone during an infinitesimal time step. The rate of coordinate change at a fixed grid label, $u^{\text{rel}} = -\partial a(t, q)/\partial t$, defines a “grid velocity” with respect to coordinates A . Note that the adaptive grid corrections in Eq. (43) enter in a conservative form of fluxes from zone to zone. If the time change of the variable y is integrated over the whole domain, all grid corrections at intermediate zone boundaries cancel. The adaptive grid does not affect conservation properties of the variable y . This important feature is maintained in the finite difference representation of Eq. (43),

$$\frac{y_{i'} \Delta a_{i'} - \bar{y}_{i'} \bar{\Delta a}_{i'}}{\Delta t} = \left(\frac{dy}{dt} \right)_{i'} \Delta a_{i'} + y_{i+1} \frac{a_{i+1} - \bar{a}_{i+1}}{\Delta t} - y_i \frac{a_i - \bar{a}_i}{\Delta t}. \quad (44)$$

The overbars in this equation mark the quantities that are evaluated at the old time, before the time step Δt .

The application of Eq. (44) for the evaluation of Lagrangian time derivatives on the adaptive grid is usually straightforward. However, a side-remark concerning our ad hoc “burning” of silicon to nuclear statistical equilibrium (NSE) at the edge of the iron core should be made here. In a Lagrangian scheme, we would simply convert zone $i + 1$ to NSE during infall as soon as the burning time scale becomes considerably smaller than the evolution time scale. The conversion from a given composition to NSE is handled such that energy remains conserved with the respective equations of state. If the adaptive grid is applied to the energy equation, it automatically performs this conversion also to the continuous mass advection between zone i and $i + 1$. This is perfect if the grid moves

outwards such that advected silicon is continuously converted to NSE. It is less perfect if the grid moves inwards, because this leads to the advection of material labelled with “NSE” from zone i to “silicon” in zone $i + 1$ until the whole zone $i + 1$ carries the label “NSE”. At this point the whole zone is converted back to NSE. Without additional measures, the advected NSE material would therefore transiently be treated as “silicon”. By energy conservation, the temperature of zone $i + 1$ would drop because energy would be invested to unphysically “unburn” the advected NSE material. We eliminate this effect by externally feeding the zone with the difference in the nuclear binding energy between advected and internal material such that no sudden changes in the thermodynamical state will take place. As soon as the zone is converted back to NSE, we extract the same amount of energy from the burning energy to restore the balance.

If the adaptive grid technique is applied to radiation quantities that depend on momentum phase space variables like the particle energy, E , or the angle cosine, μ , further considerations are required. A particle, that is observed in the comoving frame of zone one with an energy E and a propagation angle μ , is observed in the comoving frame of an adjacent zone two with energy $E' \neq E$ and $\mu' \neq \mu$ because of frequency shift and angular aberration. If the moving zone boundary sweeps over the particle such that it is assigned to the adjacent zone two, the momentum phase space state of the particle in zone two should be changed to E' and μ' in order to describe the same physical state the particle had when it was a member of zone one. The motion of the zone boundary has a second effect: The location of the center of zone two moves towards zone one and fluid momentum is advected from zone one to zone two. This means that the particles that do not change the zone are as well subject to frequency shift and angular aberration corrections in order to maintain their exact original state after the redefinition of the zones. In the more general derivation of the adaptive grid equations in Winkler and Norman (Winkler, Norman, & Mihalas 1984), these two corrections do not appear. In order to convince ourselves that they cancel, we calculate them explicitly.

We assume that we have a global description of the particle state in the momentum phase space that does not depend on the location of the particle or the velocity of the fluid element. We call these global parameters “impact parameter”, b , and “energy at infinity”, ε , because the quantities

$$\begin{aligned} b &= r \frac{\sqrt{1 - \mu^2}}{\Gamma + u\mu} \\ \varepsilon &= (\Gamma + u\mu) E. \end{aligned} \tag{45}$$

are in good approximation constants of motion along the general relativistic particle trajectory (Liebendörfer, Mezzacappa, & Thielemann 2001). Once the description of the particle

momentum phase space is invariant, it is safe to reassign neutrinos between zones according to the adaptive grid equation (43). We substitute the general variable $y(t, a)$ by the distribution function $\hat{F}(t, a, b, \varepsilon)$,

$$\frac{\partial}{\partial t} \int_{a(q_1)}^{a(q_2)} \hat{F} da + \left[-\hat{F} \frac{\partial a}{\partial t} \right]_{q_1}^{q_2} = \int_{a(q_1)}^{a(q_2)} \frac{d\hat{F}}{dt} da. \quad (46)$$

Evaluating the first term by the chain rule gives

$$\begin{aligned} \frac{\partial}{\partial t} \int_{a(q_1)}^{a(q_2)} \hat{F} da &= \frac{\partial}{\partial t} \int_{a(q_1)}^{a(q_2)} F da \\ &+ \int_{a(q_1)}^{a(q_2)} \left[\frac{\partial F}{\partial \mu} \frac{\partial \mu}{\partial t} + \frac{\partial F}{\partial E} \frac{\partial E}{\partial t} \right] da + \int_{q_1}^{q_2} \left(\hat{F} - F \right) \frac{\partial}{\partial t} \left(\frac{\partial a}{\partial q} \right) dq. \end{aligned} \quad (47)$$

The second term can be written as

$$\begin{aligned} \left[\hat{F} \frac{\partial a}{\partial t} \right]_{q_1}^{q_2} &= \left[F \frac{\partial a}{\partial t} \right]_{q_1}^{q_2} \\ &+ \int_{a(q_1)}^{a(q_2)} \left[\frac{\partial F}{\partial \mu} \frac{\partial \mu}{\partial a} + \frac{\partial F}{\partial E} \frac{\partial E}{\partial a} \right] \frac{\partial a}{\partial t} da + \int_{a(q_1)}^{a(q_2)} \left(\hat{F} - F \right) \frac{\partial}{\partial a} \left(\frac{\partial a}{\partial t} \right) da. \end{aligned} \quad (48)$$

Finally, the term on the right hand side evaluates to

$$\int_{a(q_1)}^{a(q_2)} \frac{d\hat{F}}{dt} da = \int_{a(q_1)}^{a(q_2)} \frac{dF}{dt} da + \int_{a(q_1)}^{a(q_2)} \left[\frac{\partial F}{\partial \mu} \frac{d\mu}{dt} + \frac{\partial F}{\partial E} \frac{dE}{dt} \right] da. \quad (49)$$

Substitution of expressions (47)-(49) into Eq. (46) shows that the correction terms indeed cancel. Hence, we can as well directly apply Eq. (43) to the neutrino distribution functions, $F(t, a, \mu, E)$, defined in the comoving frame

$$\frac{\partial}{\partial t} \int_{a(q_1)}^{a(q_2)} F da = \int_{a(q_1)}^{a(q_2)} \frac{dF}{dt} da + \left[F \frac{\partial a}{\partial t} \right]_{q_1}^{q_2}. \quad (50)$$

We note however, that energy conservation in the adaptive grid corrections will become resolution dependent if we finite difference Eq. (50) instead of the much more complicated Eq. (46). Particle number conservation is still guaranteed at machine precision. We quantify this effect in our energy conservation test in section 4.6.

The implementation of an adaptive grid consists of two parts: We discussed above how the physical equations are evolved on a dynamically moving grid. Here we summarize how the motion of the grid itself is controlled. On the one hand, it has to increase the local grid point concentration where steep gradients in the solution vector need to be resolved.

On the other hand, it has to capture self-similar flows and to propagate them through the computational domain. If there are traveling features in the flow, it is advantageous if the adaptive grid can just change the zone locations instead of significantly changing all the physical variables describing the state in the zones. A useful grid equation has been found in (Dorfi & Drury 1987). We transferred the approach from Eulerian coordinates in Newtonian space to comoving coordinates in general relativistic time slices such that we retrieve a Lagrangian scheme if the adaptive grid is switched off. The grid equation of Dorfi and Drury is based on a resolution function,

$$R(t, a) = \left(1 + \sum \left(\frac{a^{\text{scl}}}{y^{\text{scl}}} \frac{\partial y(t, a)}{\partial a} \right)^2 \right)^{\frac{1}{2}}, \quad (51)$$

where the sum includes a selection of relevant variables y . Currently, our grid position is guided by gradients in the velocity and logarithmic density profiles. The velocity contribution focuses on shocks and the density contribution draws grid points to steep density gradients where the resolution is important for the radiation transport. We set the global scale in this equation according to the total variation, $y^{\text{scl}} = \sum_i |y_{i+1} - y_i|$. If we define a grid point concentration, $n = a^{\text{scl}}(\partial a(t, q)/\partial q)^{-1}$, the grid equation requires that the the grid point concentration is proportional to the requested resolution (51),

$$\frac{\partial}{\partial q} \left(\frac{n}{R} \right) = 0. \quad (52)$$

After the substitution of

$$\frac{n}{R} = \left(\left(\frac{\partial a(t, q)}{a^{\text{scl}} \partial q} \right)^2 + \sum \left(\frac{\partial y(t, q)}{y^{\text{scl}} \partial q} \right)^2 \right)^{-\frac{1}{2}}, \quad (53)$$

we note that this prescription enforces a constant generalized arc length per grid point interval Δq . In the same way as Dorfi & Drury (1987), we apply operators for space smoothing and time retardation to the grid point concentration before solving Eq. (52) implicitly with the hydrodynamics equations. As the adaptive grid requires corrections in the evaluation of time derivatives, we have payed attention to reduce the occurrence of time derivatives to a minimum in the implementation of the Boltzmann equation on the adaptive grid. Therefore, we can relax the notation in the following: We will use the notation $\partial/\partial t$ for the time derivatives at constant enclosed mass. This makes the discussion of the radiation transport equation more consistent because the enclosed mass is just one of four dimensions in the phase space, and the derivatives will always be partial. The few time differences at constant zone labels will explicitly be written out in the finite difference expressions.

3.3. Finite differencing of the transport equation

We split the description of the finite differencing of the Boltzmann equation (15) into separate terms according to the list in Eq. (16)-(22). Each term is prepared in its own subsection. In section 3.5 we describe how all the individual terms are gathered to form one implicit solution of the complete transport equation and an operator split implicit solution of the hydrodynamics equations.

The knowledge of a complete set of primitive variables at a certain time allows the derivation of all other quantities of interest. Our choice of primitive variables is listed in table (2). The discretization in space is indicated by the index i . We adopt the convention that integer values of i point to zone edges while $i + 1/2$ refers to the mass center of the zone between edge i and $i + 1$. We abbreviate half-valued indices with a prime, $i' \equiv i + 1/2$, in order to not further challenge the readability of the finite difference equations. Of order 100 spatial zones are used on a dynamically adaptive grid. The particle distribution functions, $F_{i',j',k'}$, additionally depend on the particle momentum phase space, i.e. the angle cosine of the particle propagation direction, μ , and the particle energy, E , measured in the comoving frame. Both momentum phase space dimensions are discretized with zone center values, $\mu_{j'}$ and $E_{k'}$, in compliance with the above-mentioned conventions. We use Gaussian quadrature in the angles $\mu_{j'}$ with weights $w_{j'}$. They are derived from Legendre polynomials and normalized such that $\int_{-1}^1 d\mu = \sum w_{j'} = 2$. The range from inwards to outwards propagation is currently resolved with 6 different propagation angles, but we are free to choose a larger number of directions for higher resolution (see section 4.5). The energy grid is set by geometrically increasing zone edge values E_k . Following Bruenn (2002), we define the zone center energies by

$$E_{k'} = \sqrt{\frac{E_{k+1}^2 + E_{k+1}E_k + E_k^2}{3}}.$$

This choice implements the phase space volume $E_{k'}^2 dE_{k'} = (E_{k+1}^3 - E_k^3)/3$ in an exact manner. The zone center energies also form a geometric series. We currently use 12 zone center energies ranging from 3 MeV to 300 MeV, but this number can also be increased for higher resolution (see section 4.5). Thermodynamical and compositional quantities are obtained from the primitive variables ρ , T , and Y_e by the equation of state. Properties of the particle radiation field are obtained by the evaluation of the expectation value of the corresponding particle property with the primitive particle distribution function F .

3.3.1. Time derivative of the particle distribution function

The time derivative of the particle distribution function, Eq. (16), is implemented in the following way:

$$C_t = \frac{1}{\alpha_{i'} da_{i'}} \left\{ \frac{F_{i',j',k'} da_{i'} - \bar{F}_{i',j',k'} \bar{da}_{i'}}{dt} + [u_{i+1}^{\text{rel}} F_{i+1,j',k'}^* - u_i^{\text{rel}} F_{i,j',k'}^*] \right\}. \quad (54)$$

The quantities with an overbar refer to the previous value of the variables. All other quantities refer to the updated values after the time step $dt = t - \bar{t}$. On a Lagrangian grid, the mass in a spherical shell, $da_{i'} = a_{i+1} - a_i$, is a constant and the relative velocity (in mass) between the matter and the grid $u_i^{\text{rel}} = -(a_i - \bar{a}_i)/dt$ vanishes. In this case the expression would simply reduce to $C_t = \alpha_i^{-1} (F_{i',j',k'} - \bar{F}_{i',j',k'})/dt$. On the adaptive grid, however, we apply Eq. (44) and obtain Eq. (54). The additional particle fluxes across moving zone edges, $u_i^{\{\text{rel}\}} F_{i,j',k'}^*$, are evaluated by upwind differencing in order to guarantee numerical stability:

$$F_{i,j',k'}^* = \begin{cases} F_{i'-1,j',k'} & \text{if } u_i^{\text{rel}} \geq 0 \\ F_{i',j',k'} & \text{otherwise.} \end{cases} \quad (55)$$

Note that this particle advection is determined by the grid velocity alone, and not by any physical particle speed. The grid velocity can in principle become arbitrarily large. Unlike the advection due to particle propagation, it does not depend on the particle mean free path.

3.3.2. Particle propagation in space

The term D_a in Eq. (17) accounts for the particles that are propagating into and out of a spherical mass shell. From first considerations it is evident that this term has to be

	primitive variable		primitive variable
a_i	enclosed rest mass	$\rho_{i'}$	rest mass density
r_i	radius	$T_{i'}$	temperature
u_i	velocity	$Y_{e,i'}$	electron fraction
m_i	enclosed gravitational mass	$\alpha_{i'}$	lapse function
		$F_{i',j',k'}$	neutrino distribution function

Table 2: The primitive variables are listed with an index i if they live on zone edges and an index i' if they live on zone centers. The momentum phase space for the neutrino distribution function is labelled with an index j' for the angle cosine of the propagation direction and an index k' for the neutrino energy.

proportional to the dot product between the particle propagation direction and the shell boundary, i.e. the angle cosine μ . By this property, the contribution becomes proportional to the gradient of the first angular moment of the particle distribution function when the Boltzmann equation (15) is integrated over the propagation angles. In the free streaming limit, the advected particle number in a time step (always in the perspective of a comoving observer) is large with respect to the particle number in the zone. Upwind differencing of the advection terms is appropriate to limit destabilizing errors in the advection fluxes. For discrete angle cosines, $\mu_{j'}$, the direction of the particle “wind” is simply given by the sign of $\mu_{j'}$ (A particle with $\mu = 0$ propagates tangential to the mass shell). In diffusive conditions, an asymmetric differencing can lead to an overestimate of the first angular moment because of improper cancellations among the contributions of the isotropic component of the particle field. Based on transport coefficients $\beta_{i,k'}$, we therefore interpolate between upwind differencing in free streaming regimes ($\beta_{i,k'} = 1$) and centered differencing ($\beta_{i,k'} = 1/2$) in diffusive regimes (Mezzacappa & Bruenn 1993a). The chosen transport coefficients, however, have the disadvantage, that they are not perfectly one half in the diffusive regime inside the neutrino sphere. This can cause a spurious numerical contribution to the diffusion flux in the hydrodynamic limit where the particle density, multiplied by the propagation speed, exceeds the particle flux by orders of magnitude. In order to satisfy the equilibrium constraint (73) in (Mezzacappa & Bruenn 1993a) everywhere inside the neutrinosphere, we use transport coefficients according to

$$\beta_{i,k'} = \begin{cases} 1/2 & \text{if } 2dr_i > \lambda_i, \\ (2dr_i/\lambda_{i,k'} + 1)^{-1} & \text{otherwise.} \end{cases} \quad (56)$$

That is, the transport coefficients at zone edges depend on the ratio between the distance dr_i between zone centers and the neutrino energy dependent mean free path $\lambda_{i,k'}$. We finite difference the propagation term as in (Mezzacappa & Bruenn 1993a):

$$D_a = \frac{\mu_{j'}}{\alpha_{i'} da_{i'}} \left[4\pi r_{i+1}^2 \alpha_{i+1} \rho_{i+1} F_{i+1,j',k'} - 4\pi r_i^2 \alpha_i \rho_i F_{i,j',k'} \right] \quad (57)$$

with

$$\alpha_i \rho_i F_{i,j',k'} = \beta_{i,j',k'} \alpha_{i'-1} \rho_{i'-1} F_{i'-1,j',k'} + (1 - \beta_{i,j',k'}) \alpha_{i'} \rho_{i'} F_{i',j',k'}$$

for outwards propagating particles ($\mu_{j'} > 0$), and

$$\alpha_i \rho_i F_{i,j',k'} = (1 - \beta_{i,j',k'}) \alpha_{i'-1} \rho_{i'-1} F_{i'-1,j',k'} + \beta_{i,j',k'} \alpha_{i'} \rho_{i'} F_{i',j',k'} \quad (58)$$

for inwards propagating particles ($\mu_{j'} < 0$).

Based on this finite difference representation, we calculate now the expectation value D_a^4 in Eq. (37) for a later match with the observer corrections described in subsections 3.3.4 and

3.3.5. For D_a^4 we identify in Eq. (37) the weight $u_{i+1}\mu_{j'}E_{k'}$ in front of the space derivative in Eq. (57). As in Eq. (35), we perform an integration by parts over da in the finite difference representation,

$$\begin{aligned} & \frac{\mu_{j'}^2 E_{k'}}{\alpha_{i'} da_{i'}} \left[4\pi r_{i+1}^2 \alpha_{i+1} \rho_{i+1} u_{i+1} F_{i+1,j',k'} - 4\pi r_i^2 \alpha_i \rho_i u_{i+1} F_{i,j',k'} \right] \\ &= \frac{\mu_{j'}^2 E_{k'}}{\alpha_{i'} da_{i'}} \left[4\pi r_{i+1}^2 \alpha_{i+1} \rho_{i+1} u_{i+1} F_{i+1,j',k'} - 4\pi r_i^2 \alpha_i \rho_i u_i F_{i,j',k'} \right] \\ &- \frac{4\pi r_i^2}{\alpha_{i'}} \frac{u_{i+1} - u_i}{da_{i'}} \mu_{j'}^2 E_{k'} \alpha_i \rho_i F_{i,j',k'}. \end{aligned}$$

If we would additionally integrate over the momentum phase space, with $E_{k'}^2$ as the usual measure of integration, the last term would correspond to $D_a^4 = -4\pi r^2 \rho \frac{\partial u}{\partial a} K$. We insert in this term the interpolation prescription (58) for $\alpha_i \rho_i F_{i,j',k'}$ on zone edges and collect the two contributions with the zone center index i' in the distribution function to obtain a finite difference representation for $A = -4\pi r^2 \rho / \Gamma \cdot \partial u / \partial a$:

$$A_{i',k'} = \frac{4\pi \rho_{i'}}{\Gamma_{i+1} da_{i'}} \left(r_{i+1}^2 (u_{i+2} - u_{i+1}) (1 - \beta_{i+1,k'}) + r_i^2 (u_{i+1} - u_i) \beta_{i,k'} \right)$$

if $\mu_{j'} \leq 0$, and

$$A_{i',k'} = \frac{4\pi \rho_{i'}}{\Gamma_{i+1} da_{i'}} \left(r_{i+1}^2 (u_{i+2} - u_{i+1}) \beta_{i+1,k'} + r_i^2 (u_{i+1} - u_i) (1 - \beta_{i,k'}) \right) \quad (59)$$

if $\mu_{j'} > 0$. We use exactly the same analysis to evaluate the finite difference representation of $D_a^2 = -4\pi r^2 \rho \frac{\partial \Gamma}{\partial a} H$ in Eq. (37). The weight for this term in front of Eq. (57) is $\Gamma_{i+1} E_{k'}$. The result is a finite difference representation for $\Lambda = -4\pi r^2 \rho / \Gamma \cdot \partial \Gamma / \partial a$:

$$\Lambda_{i',k'} = \frac{4\pi \rho_{i'}}{\Gamma_{i+1} da_{i'}} \left(r_{i+1}^2 (\Gamma_{i+2} - \Gamma_{i+1}) (1 - \beta_{i+1,k'}) + r_i^2 (\Gamma_{i+1} - \Gamma_i) \beta_{i,k'} \right)$$

if $\mu_{j'} \leq 0$, and

$$\Lambda_{i',k'} = \frac{4\pi \rho_{i'}}{\Gamma_{i+1} da_{i'}} \left(r_{i+1}^2 (\Gamma_{i+2} - \Gamma_{i+1}) \beta_{i+1,k'} + r_i^2 (\Gamma_{i+1} - \Gamma_i) (1 - \beta_{i,k'}) \right) \quad (60)$$

otherwise. These definitions allow to write the contribution of space propagation to the total energy conservation, $\sum_{j,k} (\Gamma_{i+1} + u_{i+1}\mu_{j'}) D_{a,i'} w_{j'} E_{k'}^3 dE_{k'}$, in the form of Eq. (37),

$$\begin{aligned} D_a^{1-4} : & \quad \frac{1}{\alpha_{i'} da_{i'}} \left[4\pi r_{i+1}^2 \alpha_{i+1} \rho_{i+1} \Gamma_{i+1} H_{i+1} - 4\pi r_i^2 \alpha_i \rho_i \Gamma_i H_i \right] \\ & + \sum_{j,k} \Gamma_{i+1} \Lambda_{i',k'} F_{i',j',k'} \mu_{j'} w_{j'} E_{k'}^3 dE_{k'} \\ & + \frac{1}{\alpha_{i'} da_{i'}} \left[4\pi r_{i+1}^2 \alpha_{i+1} \rho_{i+1} u_{i+1} K_{i+1} - 4\pi r_i^2 \alpha_i \rho_i u_i K_i \right] \\ & + \sum_{j,k} \Gamma_{i+1} A_{i',k'} F_{i',j',k'} \mu_{j'}^2 w_{j'} E_{k'}^3 dE_{k'}. \end{aligned} \quad (61)$$

3.3.3. Angular advection from spatial propagation

If a particle propagates in outwards direction, its direction cosine increases towards unity. Hence, particle propagation causes angular advection relative to a fixed grid of particle direction cosines $\mu_{j'}$. This contribution to the time evolution of the particle distribution function is described in the term D_μ in Eq. (18). The finite difference representation of this term is chosen such that an equilibrium between an isotropic radiation field and stationary matter remains undisturbed (Lewis & Miller 1984; Mezzacappa & Bruenn 1993a). Following this approach, we set

$$D_\mu = \left(\Gamma_{i+1} \frac{3 [r_{i+1}^2 - r_i^2]}{2 [r_{i+1}^3 - r_i^3]} - G_{i+1}^\mu \right) \frac{1}{w_{j'}} (\zeta_{j+1} F_{i',j+1,k'} - \zeta_j F_{i',j,k'}). \quad (62)$$

Characteristic for the general relativistic equation is the gravitational term $G^\mu = \Gamma \partial \Phi / \partial r$ in Eq. (62). It implements gravitational bending. We outline its finite difference representation below in Eq. (68). The differencing of the coefficients, $\zeta = 1 - \mu^2$, is defined by

$$\zeta_{j+1} - \zeta_j = -2\mu_{j'} w_{j'}. \quad (63)$$

The angular integration of the term D_μ produces the zeroth and second angular moments of the particle distribution function. Its finite difference representation is therefore not as sensitive to cancellations in the diffusive limit as in the case of the spatial advection term D_a . Upwind differencing can be justified. The angular "wind" always points towards $\mu = 1$. However, for reasons of completeness and consistency, we also use centered differencing in the diffusive regime. With angular transport coefficients $\gamma_{i',k'} := \beta_{i',k'}$, we interpolate the values of the neutrino distribution function on angular zone edges by

$$F_{i',j,k'} = \gamma_{i',k'} F_{i',j'-1,k'} + (1 - \gamma_{i',k'}) F_{i',j,k'}. \quad (64)$$

Again, the terms D_μ^{1-4} in Eq. (37) arise from an integration by parts of the Boltzmann equation (15) with weight $(\Gamma_{i+1} + u_{i+1} \mu_{j'}) E_{k'}$. But this time the integration is over the angle cosines, μ . The part with the weight $\Gamma_{i+1} E_{k'}$ does not depend on the angle cosine, its contribution vanishes. For the calculation of the other part we introduce the abbreviation

$$\Upsilon_{i+1} = \Gamma_{i+1} \frac{3 [r_{i+1}^2 - r_i^2]}{2 [r_{i+1}^3 - r_i^3]} - G_{i+1}^\mu$$

for the prefactor in Eq. (62) and perform the integration by parts again in its finite difference representation:

$$\sum_{j,k} u_{i+1} \Upsilon_{i+1} (\zeta_{j+1} \mu_{j'} F_{i',j+1,k'} - \zeta_j \mu_{j'} F_{i',j,k'}) E_{k'}^3 dE_{k'}$$

$$\begin{aligned}
&= \sum_{j,k} u_{i+1} \Upsilon_{i+1} (\zeta_{j+1} \mu_{j'} F_{i',j+1,k'} - \zeta_j \mu_{j'-1} F_{i',j,k'}) E_{k'}^3 dE_{k'} \\
&- \sum_{j,k} u_{i+1} \Upsilon_{i+1} \zeta_j F_{i',j,k'} (\mu_{j'} - \mu_{j'-1}) E_{k'}^3 dE_{k'} \\
&= - \sum_{j,k} u_{i+1} \Upsilon_{i+1} F_{i',j',k'} E_{k'}^3 dE_{k'} \\
&\times [\gamma_{i',k'} \zeta_{j+1} (\mu_{j'+1} - \mu_{j'}) + (1 - \gamma_{i',k'}) \zeta_j (\mu_{j'} - \mu_{j'-1})]. \tag{65}
\end{aligned}$$

The expression in the second line vanishes because of mutual cancellations in the sum and $\zeta_1 = \zeta_{j_{\max}+1} = 0$. With $\zeta = 1 - \mu^2$, we can identify the result as a special finite difference representation of the terms D_μ^{12} and D_μ^{34} in Eq. (37). Following the strategy of the previous paragraph, we extract from Eq. (65) a finite difference expression for the expression $B = (1 - \mu^2) u/r$,

$$B_{i',j',k'} = \frac{3 r_{i+1}^2 - r_i^2}{2 r_{i+1}^3 - r_i^3} \frac{u_{i+1}}{w_{j'}} [\gamma_{i',k'} \zeta_{j+1} (\mu_{j'+1} - \mu_{j'}) + (1 - \gamma_{i',k'}) \zeta_j (\mu_{j'} - \mu_{j'-1})]. \tag{66}$$

With this definition, we write the contribution $\sum_{j,k} (\Gamma_{i+1} + u_{i+1} \mu_{j'}) D_{\mu,i'} w_{j'} E_{k'}^3 dE_{k'}$ to the total energy evolution in the form of its continuous analogue in Eq. (37),

$$\begin{aligned}
D_\mu : &- \Gamma_{i+1} \sum_{j,k} B_{i',j',k'} F_{i',j',k'} w_{j'} E_{k'}^3 dE_{k'} + u_{i+1} G_{i+1}^\mu \sum_{j,k} F_{i',j',k'} E_{k'}^3 dE_{k'} \\
&\times [\gamma_{i',k'} \zeta_{j+1} (\mu_{j'+1} - \mu_{j'}) + (1 - \gamma_{i',k'}) \zeta_j (\mu_{j'} - \mu_{j'-1})]. \tag{67}
\end{aligned}$$

The finite difference representation of G_{i+1}^μ for the gravitational bending still needs to be defined. We make its definition depend on the finite differencing of $G^E = \Gamma \partial \Phi / \partial r$ in Eq. (84), which will account for the gravitational frequency shift of the particle energies. In the term D_E^2 in Eq. (37) it contributes with $u_{i+1} G_{i+1}^E K_{i'}$ to total energy conservation. If we define

$$G_{i+1}^\mu = \frac{3}{2} \frac{\Gamma_{i+1}}{\alpha_{i'}} \frac{\alpha_{i'+1} - \alpha_{i'}}{r_{i'+1} - r_{i'}} - \frac{1}{2} G_{i+1}^E, \tag{68}$$

this will support the desired cancellation $C_t^2 + D_\mu^{34} + D_E^2 = 0$ under two conditions: (i) The hydrodynamics equations should accurately implement Eq. (38), i.e.

$$C_t^2 \equiv - \frac{\partial \Gamma_{i+1}}{\alpha_{i'} \partial t} J_{i'} = - u_{i+1} \frac{\Gamma_{i+1}}{\alpha_{i'}} \frac{\alpha_{i'+1} - \alpha_{i'}}{r_{i'+1} - r_{i'}} J_{i'}. \tag{69}$$

If this is not the case, an alternative discretization based on the time derivative of Γ as a function of the velocity and the gravitational potential has also provided satisfactory results (see Eq. (85) for the evaluation of $\partial u / \partial t$ on the adaptive grid),

$$C_t^2 \equiv - \frac{\partial \Gamma_{i+1}}{\alpha_{i'} \partial t} J_{i'} = \frac{u_{i+1}}{\Gamma_{i+1}} \left(\frac{\partial u}{\alpha_{i'} \partial t} + 4\pi r_{i+1} p_{i'+1} + \frac{m_{i+1}}{r_{i+1} \bar{r}_{i+1}} \right) J_{i'}.$$

(ii) The particle distribution function should be close to isotropic. In the isotropic limit we can use the relation $J = 3K$ and obtain from Eq. (65) a simplified contribution to energy conservation

$$\begin{aligned}
 D_\mu^{34} : & \quad -u_{i+1} G_{i+1}^\mu \sum_k F_{i',k'} E_{k'}^3 dE_{k'} \sum_j \mu_{j'} (\zeta_{j+1} - \zeta_j) \\
 & = u_{i+1} G_{i+1}^\mu \sum_k F_{i',k'} E_{k'}^3 dE_{k'} \sum_j \mu_{j'}^2 w_{j'} \\
 & = \frac{2}{3} u_{i+1} G_{i+1}^\mu J_{i'}.
 \end{aligned}$$

Note that the Gaussian quadrature in the angle discretization provides the exact integral for $\int \mu^2 d\mu = 2/3$. Both conditions are fulfilled in the high density domain of the protoneutron star where discretization errors most dramatically affect energy conservation because of the large radiation energy densities. Of course, Eq. (68) provides also a valid finite differencing of gravitational bending outside of the protoneutron star, where the effect is physically important. But the finite differencing is not specially tuned to enforce the cancellation $C_t^2 + D_\mu^{34} + D_E^2 = 0$ outside of the diffusive regime.

3.3.4. Frequency shift from observer motion

We continue our description with the observer correction O_E in Eq. (20). We start with a review of the finite differencing procedure presented in (Mezzacappa & Bruenn 1993a) in order to extend it from local to global energy conservation. Global energy conservation requires the cancellation of observer correction terms in Eq. (37) with terms from space propagation and angular advection. Therefore, it is convenient to express the observer corrections in terms of the same physical quantities A and B we have used before,

$$\begin{aligned}
 A &= \left(\frac{\partial \ln \rho}{\alpha \partial t} + \frac{2u}{r} \right) \\
 B &= (1 - \mu^2) \frac{u}{r}. \\
 O_E &= (\mu^2 A - B) \frac{1}{E^2} \frac{\partial}{\partial E} [E^3 F].
 \end{aligned} \tag{70}$$

In the following, we solve the equation for the frequency shift correction, $C_t + O_E = 0$, by the method of characteristics. We convert the time derivative at constant energy to a time derivative along the characteristic in the energy dimension of the momentum phase space. This eliminates the partial derivative with respect to energy and facilitates a conservative finite differencing of O_E . Note that the characteristic used in this section implements the

frequency shift correction alone, it differs from the free propagation characteristic prescribed by the full Boltzmann equation. As in (Bruenn 1985; Mezzacappa & Bruenn 1993a) we write the prefactor of the correction as a time derivative of a quantity $R_f = r^{(3\mu^2-1)}\rho^{(\mu^2)}$,

$$\frac{\partial \ln R_f}{\alpha \partial t} = \mu^2 A - B,$$

such that $C_t + O_E = 0$ becomes

$$0 = E^3 \left(\frac{\partial F}{\partial t} \right)_E + \frac{\partial \ln R_f}{\partial t} E \frac{\partial}{\partial E} [E^3 F]. \quad (71)$$

It is now possible to transform from the “Eulerian” variable, $x \equiv E$, to a “Lagrangian” variable, $y \equiv E/R_f$, along the characteristic by the chain rule $(\partial/\partial t)_x = (\partial/\partial t)_y + (\partial y/\partial t)_x (\partial/\partial y)$ (the subscript of the bracket denotes the variable that is kept constant for the differentiation). Eq. (71) simplifies to

$$\begin{aligned} 0 &= \left(\frac{\partial}{\partial t} [E^3 F] \right)_E + \frac{\partial R_f}{R_f^2 \partial t} E \times R_f \frac{\partial}{\partial E} [E^3 F] \\ &= \left(\frac{\partial}{\partial t} [E^3 F] \right)_E - \left(\frac{\partial [E/R_f]}{\partial t} \right)_E \frac{\partial [E^3 F]}{\partial [E/R_f]} = \left(\frac{\partial}{\partial t} [E^3 F] \right)_{E/R_f}. \end{aligned}$$

For a small section of the energy phase space $E^2 \Delta E = (E_2^3 - E_1^3)/3$, this relationship leads to

$$\left(\frac{\partial}{\partial t} [E^2 F \Delta E] \right)_{E/R_f} = 0. \quad (72)$$

The validity of Eq. (72) for arbitrary distribution functions F leads to the following interpretation: The observer correction shifts the particles that initially reside in the energy interval $E^2 \Delta E$ along the characteristic with constant E/R_f in the energy phase space. This allows us to determine the evolution of any other particle property in analogy to Eq. (33). For example, the specific energy of the particles in this phase space interval, $d\epsilon = E^3 F \Delta E$, evolves according to

$$\left(\frac{\partial}{\partial t} [E^3 F \Delta E] \right)_{E/R_f} = E^2 F \Delta E \left(\frac{\partial E}{\partial t} \right)_{E/R_f} = \frac{\partial \ln R_f}{\partial t} d\epsilon. \quad (73)$$

A finite difference representation of Eqs. (72) and (73) has been given in (Mezzacappa & Bruenn 1993a). Consider a particle energy group k' , with a neighbor group $k' + dk$, $dk = \pm 1$. Eq. (72) tells us that the number of particles before the correction, $F_{i',j',k'} E_{k'}^2 dE_{k'}$, is equal to the number of particles after the correction. The distribution after the correction

is represented by a diminished number of particles $F_{i',j',k'} E_{k'}^2 dE_{k'} - n_{i',j',k'}^-$ in group k' and an additional number of particles $n_{i',j',k'+dk}^+$ in the neighbor group $k' + dk$,

$$F_{i',j',k'} E_{k'}^2 dE_{k'} - [(F_{i',j',k'} E_{k'}^2 dE_{k'} - n_{i',j',k'}^-) + n_{i',j',k'+dk}^+] = 0. \quad (74)$$

Eq. (73) now defines a similar relationship for the particle energies

$$\begin{aligned} F_{i',j',k'} E_{k'}^3 dE_{k'} &= [(F_{i',j',k'} E_{k'}^3 dE_{k'} - E_{k'} n_{i',j',k'}^-) + E_{k'+dk} n_{i',j',k'+dk}^+] \\ &= -(\mu_{j'}^2 A_{i',k'} - B_{i',j',k'}) F_{i',j',k'} E_{k'}^3 dE_{k'} \alpha_{i'} dt, \end{aligned} \quad (75)$$

where $A_{i',k'}$ and $B_{i',j',k'}$ stand for a finite difference representation of Eq. (70). Eqs. (74) and (75) uniquely define the solution

$$\begin{aligned} n_{i',j',k'}^- &= (\mu_{j'}^2 A_{i',k'} - B_{i',j',k'}) \frac{dE_{k'}}{E_{k'+dk} - E_{k'}} E_{k'}^3 F_{i',j',k'} \alpha_{i'} dt \\ n_{i',j',k'}^+ &= n_{i',j',k'-dk}^-, \end{aligned} \quad (76)$$

which leads, by the update $F_{i',j',k'} = \bar{F}_{i',j',k'} + (n_{i',j',k'}^+ - n_{i',j',k'}^-) / (E_{k'}^2 dE_{k'})$, to the following finite difference representation of the frequency shift term in the Boltzmann equation (15):

$$\begin{aligned} O_E &= \frac{1}{E_{k'}^2 dE_{k'}} \\ &\times \left[(\mu_{j'}^2 A_{i',k'-dk} - B_{i',j',k'-dk}) \frac{dE_{k'-dk}}{E_{k'} - E_{k'-dk}} E_{k'-dk}^3 F_{i',j',k'-dk} \right. \\ &\quad \left. - (\mu_{j'}^2 A_{i',k'} - B_{i',j',k'}) \frac{dE_{k'}}{E_{k'+dk} - E_{k'}} E_{k'}^3 F_{i',j',k'} \right]. \end{aligned} \quad (77)$$

Finally, we calculate the contribution of the frequency shift to energy conservation,

$$\sum_{j,k} (\Gamma_{i+1} + u_{i+1} \mu_{j'}) O_{E,i} w_{j'} E_{k'}^3 dE_{k'}.$$

The summation over k in Eq. (77) with weight $E_{k'}$ and measure of integration $E_{k'}^2$ can be simplified with a discrete “integration by parts” as in Eq. (35). If we neglect for the time being the boundary terms because of a small E_1^3 in the lowest energy group and a small $F_{i',j',k'_{\max}}$ in the highest energy group (a correction for these terms will be made later in subsection 3.3.7), the energy contribution from O_E becomes

$$O_E^{1-4} : \quad - \sum_{j,k} (\Gamma_{i+1} + u_{i+1} \mu_{j'}) (\mu_{j'}^2 A_{i',k'} - B_{i',j',k'}) F_{i',j',k'} w_{j'} E_{k'}^3 dE_{k'}. \quad (78)$$

If we use the finite difference representations (59) and (66) for $A_{i',k'}$ and $B_{i',j',k'}$ respectively, we find in the comparison of Eq. (78) with Eqs. (61) and (67) that we have indeed matched the terms $(D_a^4 O_E^1)$ and $(D_\mu^{12} O_E^{34})$ to machine precision (Liebendörfer 2000).

3.3.5. Angular aberration from observer motion

Motivated by this success, we try the method of characteristics also on the angular aberration corrections. In this case, the characteristic is described by $C_t + O_\mu = 0$. We write the prefactor of the angular aberration correction in Eq. (21) as a function of the quantities A and B defined in Eq. (70) to obtain with $\zeta = 1 - \mu^2$,

$$O_\mu = (A + B/\zeta) \frac{\partial}{\partial \mu} [\zeta \mu F].$$

As before, we try to eliminate the partial derivative with respect to the angle cosine with a time derivative along the characteristic in the angle part of the momentum phase space (Liebendörfer 2000). For the quantity $R_a = r^3 \rho$, we find the relation

$$\frac{\partial \ln R_a}{\alpha \partial t} = A + B/\zeta.$$

With this, we transform from the “Eulerian” variable $x \equiv \mu$ to the “Lagrangian” variable $y \equiv \zeta^{-1/2} \mu / R_a$. After a multiplication with $\zeta \mu$, the angular aberration correction $0 = C_t + O_\mu$ becomes:

$$\begin{aligned} 0 &= \zeta \mu \left[\left(\frac{\partial F}{\partial t} \right)_\mu + \frac{\partial \ln R_a}{\partial t} \frac{\partial}{\partial \mu} [\zeta \mu F] \right] \\ &= \left(\frac{\partial}{\partial t} [\zeta \mu F] \right)_\mu + \zeta^{-1/2} \mu \frac{\partial R_a}{R_a^2 \partial t} \times \zeta^{3/2} R_a \frac{\partial}{\partial \mu} [\zeta \mu F] \\ &= \left(\frac{\partial}{\partial t} [\zeta \mu F] \right)_\mu - \left(\frac{\partial [\zeta^{-1/2} \mu / R_a]}{\partial t} \right)_\mu \frac{\partial [\zeta \mu F]}{\partial [\zeta^{-1/2} \mu / R_a]} = \left(\frac{\partial}{\partial t} [\zeta \mu F] \right)_{\zeta^{-1/2} \mu / R_a}. \end{aligned}$$

The particles initially residing in the angular interval $(1 - 3\mu^2) \Delta\mu = \zeta_2 \mu_2 - \zeta_1 \mu_1$ are shifted by angular aberration along characteristics with constant $\mu / (\sqrt{\zeta} R_a)$:

$$\left(\frac{\partial}{\partial t} [(1 - 3\mu^2) F \Delta\mu] \right)_{\zeta^{-1/2} \mu / R_a} = 0. \quad (79)$$

We have to keep in mind that any correction to the particle propagation direction also affects the energy conservation in the frame of a distant observer. Therefore, it is desirable to construct a numerical implementation of angular aberration that prescribes the changes in the specific luminosity $\sum_j \mu_{j'} F_{i',j',k'} w_{j'}$ to machine precision. Hence, we evaluate the change of the specific luminosity, $d\ell = (1 - 3\mu^2) \mu F \Delta\mu$, along the characteristic in analogy to Eq. (33),

$$\left(\frac{\partial}{\partial t} [(1 - 3\mu^2) \mu F \Delta\mu] \right)_{\zeta^{-1/2} \mu / R_a} = (1 - 3\mu^2) F \Delta\mu \left(\frac{\partial \mu}{\partial t} \right)_{\zeta^{-1/2} \mu / R_a} = \zeta \frac{\partial \ln R_a}{\partial t} d\ell. \quad (80)$$

We identify the bin size $(1 - 3\mu_{j'}^2) \Delta\mu_{j'} = w_{j'}$ with our Gaussian quadrature weights. In the finite difference representation, Eq. (79) leads to the condition for number conservation

$$F_{i',j',k'} w_{j'} - [(F_{i',j',k'} w_{j'} - n_{i',j',k'}^-) + n_{i',j'+dj,k'}^+] = 0$$

and Eq. (80) to a prescription for the numerical evolution of the specific luminosity

$$\begin{aligned} F_{i',j',k'} \mu_{j'} w_{j'} &= [(F_{i',j',k'} \mu_{j'} w_{j'} - \mu_{j'} n_{i',j',k'}^-) + \mu_{j'+dj} n_{i',j'+dj,k'}^+] \\ &= -(\zeta_{j'} A_{i',k'} + B_{i',j',k'}) F_{i',j',k'} \mu_{j'} w_{j'} \alpha_{i'} dt. \end{aligned}$$

The direction of the differencing can be chosen by $dj = \pm 1$. The change in the neutrino distribution function from angular aberration is then:

$$F_{i',j',k'} = \bar{F}_{i',j',k'} + (n_{i',j',k'}^+ - n_{i',j',k'}^-) / w_{j'}$$

with

$$\begin{aligned} n_{i',j',k'}^- &= (A_{i',k'} + B_{i',j',k'} / \zeta_{j'}) \frac{w_{j'}}{\mu_{j'+dj} - \mu_{j'}} \zeta_{j'} \mu_{j'} F_{i',j',k'} \alpha_{i'} dt \\ n_{i',j',k'}^+ &= n_{i',j'-dj,k'}^- \end{aligned}$$

Combined into one update, this leads to the following finite difference representation of the angular aberration term in the Boltzmann Eq. (15):

$$\begin{aligned} O_\mu &= \frac{1}{w_{j'}} \left[(A_{i',k'} + B_{i',j'-dj,k'} / \zeta_{j'-dj}) \frac{w_{j'-dj}}{\mu_{j'} - \mu_{j'-dj}} \zeta_{j'-dj} \mu_{j'-dj} F_{i',j'-dj,k'} \right. \\ &\quad \left. - (A_{i',k'} + B_{i',j',k'} / \zeta_{j'}) \frac{w_{j'}}{\mu_{j'+dj} - \mu_{j'}} \zeta_{j'} \mu_{j'} F_{i',j',k'} \right]. \end{aligned} \quad (81)$$

We apply the aberration corrections with $dj = +1$ for $\mu \leq 0$ and $dj = -1$ for $\mu > 0$. This is not upwind differencing and, therefore, runs the risk of producing negative particle distribution functions. However, there are two good reasons to accept this shortcoming: (i) The angular aberration correction is generally small, with the exception of aberration in the vicinity of strong shocks with large velocity gradients. (ii) The chosen direction of dj guarantees that no particles are shifted off the grid. This is a prerequisite for number and energy conservation. If we calculate the contribution of O_μ to the energy evolution, $\sum_{j,k} (\Gamma_{i+1} + u_{i+1} \mu_{j'}) O_{\mu,i'} w_{j'} E_k^3 dE_{k'}$, along the lines of Eq. (35), this choice of dj causes the perfect vanishing of boundary terms in the discrete “integration by parts” with respect to the angle cosine. We obtain

$$O_\mu^{1-4} : \quad \sum_{j,k} u_{i+1} \mu_{j'} (-A_{i',k'} + \mu_{j'}^2 A_{i',k'} - B_{i',j',k'}) F_{i',j',k'} w_{j'} E_k^3 dE_{k'}. \quad (82)$$

The second and third terms in the parenthesis cancel exactly with the yet unmatched terms from O_E^{1-4} in Eq. (78). Thus, also the cancellations $(O_E^2 O_\mu^2)$ and $(O_E^{56} O_\mu^{34})$ are guaranteed in Eq. (37). However, in failed supernova simulations, the shock recedes at late time to very small radii and becomes very strong because of high infall velocities. We have encountered numerical fluctuations in the neutrino distribution function at the shock position at this late time that are due to this fixed choice of differencing in the angular advection in the aberration terms. They disturb the progress of the simulation with large time steps. In future long term simulations, we will use strict upwind differencing also in the angular aberration terms and allow a deviation from perfect energy conservation in these terms (we still conserve particle number). In section 4.6, we demonstrate that the expected energy violations from angular aberration are unlikely to dominate the violations of energy conservation by the adaptive grid or a mismatch in $(C_t^2 D_\mu^{34} D_E^2)$.

3.3.6. Frequency shift in the gravitational potential

The action of the gravitational potential on the propagation of the particles, $C_t + D_E = 0$, in Eq. (19), is finite differenced in full analogy with Eq. (77),

$$D_E = -\frac{\mu_{j'} G_{i+1}^E}{E_{k'}^2 dE_{k'}} \left[\frac{dE_{k'-dk}}{E_{k'} - E_{k'-dk}} E_{k'-dk}^3 F_{i',j',k'-dk} - \frac{dE_{k'}}{E_{k'+dk} - E_{k'}} E_{k'}^3 F_{i',j',k'} \right]. \quad (83)$$

This is a valid finite difference representation of $D_E = -\mu G^E / E^2 \cdot \partial(E^3 F) / \partial E$. We apply the corrections from Eqs. (77) and (83) with $dk = +1$ (blueshift) if the two following conditions are met: (i) $\sum_{j,k} (\mu_{j'}^2 A_{i',k'} - B_{i',j',k'}) w_{j'} E_{k'}^2 dE_{k'}$ is positive, and (ii), its absolute value is larger than $\left| \sum_{j,k} \mu_{j'} G_{i+1}^E w_{j'} E_{k'}^2 dE_{k'} \right|$. Otherwise, we choose $dk = -1$ for a frequency redshift. With this, the chosen sign of dk in Eqs. (77) and (83) implements upwind differencing for the angle-integrated distribution function. Note, that the direction of the finite differencing in energy space must not depend on the individual angle bins. An angle dependence would destroy the important cancellation of redshift and blueshift in the limit of an isotropic distribution function.

In Eq. (68), we have introduced the placeholder $G^E = \Gamma \frac{\partial \Phi}{\partial r}$, whose finite differencing we will now define. Eq. (41) describes how the terms $(C_t^4 D_a^2 D_E^1 O_\mu^1)$ should combine to the expression $4\pi r \rho (1 + e + p/\rho) H$. The latter is used in the equation for the total energy evolution. A matching of the energy changes in C_t^4 , D_a^2 , O_μ^1 , and D_E^1 to this expression is the last constraint of the list in Eq. (37) that we have not yet implemented. The term C_t^4 is determined by $\alpha^{-1} \partial u / \partial t$ in the hydrodynamics equations. The finite differencing of the terms D_a^2 and O_μ^1 has also been determined in the second line of Eq. (61) and in the first

term of Eq. (82) respectively. We simply resolve for G^E and obtain

$$\begin{aligned} G_{i+1}^E &= \frac{1}{\Gamma_{i+1}} \left(\frac{\partial u}{\alpha_{i'} \partial t} + 4\pi r_{i+1} \rho_{i'} (1 + e_{i'} + p_{i'+1}/\rho_{i'}) \right) \\ &+ \frac{1}{H_{i'}} \sum_{j,k} (A_{i',k'} - \Lambda_{i',k'}) F_{i',j',k'} \mu_{j'} w_{j'} E_{k'}^3 dE_{k'}. \end{aligned} \quad (84)$$

The evaluation of the Lagrangian time derivative $\partial u / \partial t$ on the adaptive grid requires the appropriate corrections. The application of Eq. (44) to the velocity leads to

$$\frac{\partial u}{\partial t} = \frac{1}{da_i} \left\{ \frac{u_i da_i - \bar{u}_i \bar{d}a_i}{dt} + [u_{i'}^{\text{rel}} u_{i'}^* - u_{i'-1}^{\text{rel}} u_{i'-1}^*] \right\}, \quad (85)$$

where we have once more used the grid velocity with respect to mass, $u_{i'}^{\text{rel}} = -(a_{i'} - \bar{a}_{i'}) / dt$. The advected velocity is evaluated by upwind differencing:

$$u_{i'}^* = \begin{cases} u_i & \text{if } u_{i'}^{\text{rel}} \geq 0 \\ u_{i+1} & \text{otherwise.} \end{cases}$$

3.3.7. Boundary corrections and the enforcement of Fermi statistics

k_{max} energy groups are subject to a frequency shift, but there are only $k_{\text{max}} - 1$ enclosed group edges to shift particles across. In the energy phase space, upwind differencing is necessary for the stability. Therefore, the straightforward application of Eqs. (77) and (83) leads to particles that fall aside the grid. The lost particle number is proportional to the particle population in the energy groups at the boundaries of the grid. At the lower boundary it is small because the phase space volume $E^2 dE$ is small. At the upper boundary it is small because the neutrino distribution function is small. The particle loss at both boundaries would approach zero when the coverage of the energy grid would be extended. Nevertheless, we want to correct for this effect and avoid that particles and energy unaccountedly disappear from the radiation field. On the one hand, we would like to support requirement (iii) in the introduction of this section with an accurate evolution of the radiation moments, even and especially at low energy resolution. On the other hand, conservation to machine precision in wellknown terms is an existential practical asset in the hunt of unknown energy leaks in a complex code. To resolve this issue, we simply do not apply the energy shift to the boundary group if this would advect particles off the grid. This exception fixes particle number conservation. The induced error in the energy balance of the radiation field is then restored by the application of minimal energy shifts to the population of all other energy groups.

Before we describe the details of this correction, we mention another exceptional correction to the frequency shift. It is applied when the Fermi statistics of the radiation particles is violated by numerical effects. The collision term C_c includes all necessary blocking factors to avoid the overpopulation of states in the fermionic particle gas by emission or inscattering. If inelastic interactions occur on a very short time scale, they will efficiently restore numerical deviations from perfect Fermi statistics in the radiation field. However, an overpopulation of energy groups can still occur in the numerical implementation. Consider for example a hydrostatic situation with a collisionless degenerate particle gas. The Boltzmann equation (15) reduces in this case to $D_a + D_\mu + D_E = 0$. It is straightforward to demonstrate that $\rho F = 1$ is a solution of this equation. In the numerical implementation, however, it is unlikely that the redshift towards low energy groups, D_E , is to machine precision compensated by the space propagation term, D_a , and angular advection term, D_μ . Even if the collision term is large, overpopulated energy groups may occur as a consequence of operator splitting. Our previous code version (Mezzacappa & Bruenn 1993a) implemented the observer corrections in Eq. (77), (81), and (83) in an operator split explicit update to the implicit solution of the transport equation $C_t + D_a + D_\mu = C_c$. In this case, overpopulation is more likely to occur. The scheme described below has been developed for this context. For simulations with massive progenitors in general relativity, however, we have expanded the implicit solver to include all terms of the transport equation (Liebendörfer et al. 2002). For cosmetic reasons we still strictly enforce Fermi statistics when necessary. We performed a control run with both corrections switched off. At any time before and including bounce, deviations in the luminosity are smaller than 2%. Differences in the rms energies are smaller than 0.5%, and in any hydrodynamic quantity smaller than 0.2%. When the shock propagates through the neutrino-degenerate core, the 2% differences in the luminosity cause transient differences of the same size in parts of the velocity and the density profile. Later, the differences are smaller than 1% in any quantity and at any time.

As in (Mezzacappa & Bruenn 1993a), we recursively shift overpopulated particles into the next higher energy group. This procedure is number conservative, but it introduces an artificial increase of the internal energy of the radiation field. The details of the correction scheme for low resolution boundary effects and overpopulation are the following: First, we quantify the energy correction:

$$R_{i',j'} = (\mu_{j'}^2 A_{i',k'} - B_{i',j',k'} - \mu_{j'} G_{i+1}^E) \bar{F}_{i',j',k'} E_{k'}^3 dE_{k'},$$

with $k = k_{\max}$, if $dk = 1$ (blueshift); and $k = 1$, if $dk = -1$ (redshift). The corrections stem in most cases from an energy redshift. Thus, we set $dk = -1$ and initialize the accumulation of corrections in $\Delta_{i',j',k'}$ with $\Delta = 0$. Then, we loop over k in ascending order and carry out the following procedure: (i) Distribute the correction $R_{i',j'}$ over all groups ℓ'

with $k + 1 \leq \ell \leq k_{\max}$ according to

$$\Delta_{i',j',\ell'} = \Delta_{i',j',\ell'} + \frac{R_{i',j'}}{\sum_{s=k+1,k_{\max}} \bar{F}_{i',j',s'} E_{s'}^3 dE_{s'}}.$$

(ii) Apply the correction $\Delta_{i',j',k'+1}$ according to the conservative finite differencing used in Eq. (76)

$$n_{i',j',k'}^+ = -\Delta_{i',j',k'+1} \frac{dE_{k'+1}}{E_{k'+1} - E_{k'}} E_{k'+1}^3 \bar{F}_{i',j',k'+1}$$

and update the particle distribution function

$$\frac{F_{i',j',k'} - \bar{F}_{i',j',k'}}{\alpha_{i'} dt} = \frac{n_{i',j',k'}^+ - n_{i',j',k'-1}^+}{E_{k'}^2 dE_{k'}}. \quad (86)$$

(iii) If the distribution function $F_{i',j',k'}$ is larger than $1/\rho_{i'}$, correct the particle flux into this group by the amount of overpopulation, $n_{i',j',k'}^+ = n_{i',j',k'}^+ + (1/\rho_{i'} - F_{i',j',k'}) E_{k'}^2 dE_{k'}$, and evaluate the energy change owing to this flux correction,

$$R_{i',j'} = (1/\rho_{i'} - F_{i',j',k'}) (E_{k'+1} - E_{k'}) E_{k'}^2 dE_{k'}.$$

Set $F_{i',j',k'}$ to the maximum value, $1/\rho_{i'}$ and apply the energy correction $R_{i',j'}$ with the next iteration of the loop over k .

3.3.8. Collision term

The finite difference representation of the collision term, Eq. (22), is described in detail in (Mezzacappa & Bruenn 1993b,c; Mezzacappa & Messer 1999; Messer 2000). We represent it here with a simple placeholder, namely emissivity $j_{i',k'}$ and opacity $\chi_{i',k'}$ as a function of the thermodynamical state of the fluid,

$$C_c = \frac{j_{i',k'}(\rho_{i'}, T_{i'}^*, Y_{e,i'}^*)}{\rho_{i'}} - \chi_{i',k'}(\rho_{i'}, T_{i'}^*, Y_{e,i'}^*) F_{i',j',k'}. \quad (87)$$

The quantities with a star refer to quantities that have consistently been updated with the particle distribution functions before the actual hydrodynamics update. We outline the time sequence of the evaluation of equations in section 3.5.

3.4. Coupling between the radiation field and the fluid

The neutrino radiation field in the supernova is tightly coupled to the high density fluid. In order to obtain a well defined link between the evolution of radiation quantities

and the evolution of hydrodynamical quantities, we recall that the solution of the microscopic Boltzmann equation updates the radiation moments according to Eqs. (28)-(30). We may now subtract these updates from the global evolution equations (6)-(12) to find the hydrodynamical part of the evolution equations

$$\frac{\partial}{\partial t} \left[\frac{\Gamma}{\rho} \right] = \frac{\partial}{\partial a} [4\pi r^2 \alpha u] \quad (88)$$

$$\begin{aligned} \frac{\partial}{\partial t} [\Gamma (1 + e)] &= -\frac{\partial}{\partial a} [4\pi r^2 \alpha u p] \\ &\quad - \alpha \Gamma \int \left(\frac{j}{\rho} - \chi F \right) E^3 dE d\mu + \alpha u \int \chi F E^3 dE \mu d\mu \end{aligned} \quad (89)$$

$$\begin{aligned} \frac{\partial}{\partial t} [u (1 + e)] &= -4\pi r^2 \frac{\partial}{\partial a} [\alpha \Gamma p] \\ &\quad - \frac{\alpha}{r} \left[(1 + e) \left(1 + \frac{6Vp}{m} \right) \frac{m}{r} + 4\pi r^2 ((1 + e) \rho K + pJ) \right. \\ &\quad \left. + \left(2u^2 - \frac{m}{r} \right) \frac{2p}{\rho} \right] \\ &\quad + \alpha \Gamma \int \chi F E^3 dE \mu d\mu - \alpha u \int \left(\frac{j}{\rho} - \chi F \right) E^3 dE d\mu \end{aligned} \quad (90)$$

$$\frac{\partial}{\partial t} Y_e = \mp \alpha \int \left(\frac{j}{\rho} - \chi F \right) E^2 dE d\mu \quad (91)$$

$$\frac{\partial V}{\partial a} = \frac{\Gamma}{\rho} \quad (92)$$

$$\frac{\partial m}{\partial a} = \Gamma (1 + e + J) + uH \quad (93)$$

$$\rho (1 + e) \frac{\partial \alpha}{\partial a} = -\frac{\partial}{\partial a} [\alpha p] + \frac{\alpha}{4\pi r^2} \int \chi F E^3 dE \mu d\mu \quad (94)$$

$$\frac{\partial e}{\partial t} = -p \frac{\partial}{\partial t} \left(\frac{1}{\rho} \right) - \alpha \int \left(\frac{j}{\rho} - \chi F \right) E^3 dE d\mu. \quad (95)$$

The equations are written such that the presence of the radiation field only enters in terms of energy and momentum exchange. In the limit of a decoupled radiation and matter flow we therefore solve for ideal hydrodynamics and free streaming in an independent and numerically stable manner, no matter what the size of the radiation field is. The only remaining interactions between the radiation field and the fluid are of a gravitational nature, for example in the contribution of the radiation field to the common gravitational mass in Eq. (93), or in the term $4\pi r^2 ((1 + e) \rho K + pJ)$ in the momentum equation (90). The detailed discretization of Eqs. (88)-(95) has been described in (Liebendörfer, Rosswog & Thielemann

2002). The interaction terms between the radiation field and the fluid are

$$\begin{aligned}
e_{i'}^{\{\text{ext}\}} &= \sum_{j',k'} \left(\frac{j_{k'}(\rho_{i'}, T_{i'}^*, Y_{e,i'}^*)}{\rho_{i'}} - \chi_{k'}(\rho_{i'}, T_{i'}^*, Y_{e,i'}^*) F_{i',j',k'} \right) E_{k'}^3 dE_{k'} w_{j'} \\
S_{i+1}^{\{\text{ext}\}} &= - \sum_{j',k'} \chi_{k'}(\rho_{i'}, T_{i'}^*, Y_{e,i'}^*) F_{i',j',k'} E_{k'}^3 dE_{k'} \mu_{j'} w_{j'} \\
Y_{e,i'}^{\{\text{ext}\}} &= \mp \sum_{j',k'} \left(\frac{j_{k'}(\rho_{i'}, T_{i'}^*, Y_{e,i'}^*)}{\rho_{i'}} - \chi_{k'}(\rho_{i'}, T_{i'}^*, Y_{e,i'}^*) F_{i',j',k'} \right) E_{k'}^2 dE_{k'} w_{j'}, \quad (96)
\end{aligned}$$

where the minus sign in the Y_e -term is used for electron neutrinos and the plus sign for electron antineutrinos. Emission and absorption of μ - and τ -neutrinos do not change the electron fraction. The star superscript for the temperature and electron fraction variables indicates again an evaluation of the cross sections for emission and absorption with a consistently updated thermodynamical state as described in the next section.

3.5. Implicit Solution

We have now a finite difference representation for every term of the transport equation. In this section we join them to one implicitly determined solution. Each time step cycles through an implicitly finite differenced update of the neutrino distribution functions and the thermodynamic state of the matter, an implicitly finite differenced update of the hydrodynamics variables and the adaptive grid, and an explicitly finite differenced cosmetic correction. The intermediately updated values do not belong to uniquely defined physical times. We denote them by fractional values of the cycle counter n . In detail, the update of the primitive variables for one cycle proceeds as follows:

1. We start with the old neutrino distribution functions $\bar{F} := F(n-1/2)$ for the electron flavor neutrinos. They are given on a Lagrangian mass grid \bar{a} . We assume that we know the old hydrodynamic variables, $\{\bar{a}, \bar{r}, \bar{u}, \bar{m}, \bar{\rho}, \bar{T}, \bar{Y}_e, \bar{\alpha}\} := H(n-1)$, and that the new hydrodynamic variables, $\{a, r, u, m, \rho, T, Y_e, \alpha\} := H(n)$, have been calculated in step (3) of the previous cycle. In one implicitly finite differenced update, we solve for $F(n) := F$ as prescribed by the transport equation $C_t + D_a + D_\mu + D_E + O_E + O_\mu - C_c = 0$. The finite differencing is chosen according to Eqs. (54), (57), (62), (77), (81), (83), and (87). This implicit update additionally includes equations for the evolution of the temperature and electron fraction due to particle-fluid interactions. These quantities are strongly coupled to the radiation field. We solve for

$$\frac{e_{i'}^* - e_{i'}}{dt} = \alpha_{i'} e_{i'}^{\text{ext}} \quad (97)$$

$$\frac{Y_{e,i'}^* - Y_{e,i'}}{dt} = \alpha_{i'} Y_{e,i'}^{\text{ext}}, \quad (98)$$

where the source terms are given in Eq. (96). Note that Eq. (97) also determines the temperature because the internal energy and temperature in the implicit update are always consistent with the equation of state, $e^*(\rho, T^*, Y_e^*)$ and $e(\rho, T, Y_e)$. We repeat step (1) for the muon flavor neutrinos. The tauon flavor neutrinos are included by counting the appropriate muon quantities twice. But we always distinguish neutrinos from antineutrinos.

2. In this minor second update, we correct for discretization errors caused by the advection scheme in the energy phase space and for numerical violations of Fermi statistics. This update is not related to any physical terms and only relevant in low resolution simulations. We set $\bar{F} := F(n)$, and update $F(n+1/2) := F$ as described by Eq. (86).
3. In the update of the hydrodynamics variables, the primitives $\{\bar{a}, \bar{r}, \bar{u}, \bar{m}, \bar{\rho}, \bar{T}, \bar{Y}_e, \bar{\alpha}\} := H(n)$ are evolved to $H(n+1) := \{a, r, u, m, \rho, T, Y_e, \alpha\}$ in a fully implicit step according to Eqs. (88)-(95). Note that we use the neutrino distribution function $F(n)$ rather than $F(n+1/2)$ to evaluate the moments J , H , and K for the gravitational coupling. The former are the direct result from the implicit solution of the transport equation and represent more accurately the quasi-stationary radiation quantities. The hydrodynamics update is based on the transfer of internal energy, e^{ext} , electron fraction, Y_e^{ext} , and the neutrino stress, S^{ext} , as evaluated in the first step of this cycle. The detailed finite difference representation in AGILE has been outlined in (Liebendörfer, Rosswog & Thielemann 2002).

Steps 1, 2, and 3 form literally a cycle; there is no position where *all* data are consistently updated. After step 1, the neutrino distribution functions $F(n)$ are in accurate equilibrium with the matter. After step 2, the energy conserving corrections from energy advection are included and the distribution functions $F(n+1/2)$ obey Fermi statistics exactly. After step 3, the overall energy conservation is balanced, but the new hydrodynamic variables $H(n+1)$ already live on a different spatial grid than the neutrino distribution function. We chose to set the integer value of n at the instance we dump the result into files. This is between step 1 and step 2, where all quantities live on the same grid positions and where all rates and neutrino distribution functions accurately reflect equilibrium conditions if the mean free paths are small.

Above description is complete with respect to what we compute. It does not address the question of how we compute. We apply a Newton-Raphson scheme to solve the implicitly finite differenced nonlinear equations in step (1) and step (3). The solution vectors for the

two updates are

$$y_{i'}^{\text{rad}} = \begin{pmatrix} F_{i',j=1'-j'_{\text{max}},1'}^\nu \\ \cdot \\ \cdot \\ F_{i',1'-j'_{\text{max}},k'_{\text{max}}}^\nu \\ F_{i',j=1'-j'_{\text{max}},1'}^{\bar{\nu}} \\ \cdot \\ \cdot \\ F_{i',1'-j'_{\text{max}},k'_{\text{max}}}^{\bar{\nu}} \\ T_{i'} \\ Y_{e,i'} \end{pmatrix}, \quad y_{i'}^{\text{hyd}} = \begin{pmatrix} a_i \\ r_i \\ u_i \\ m_i \\ \rho_{i'} \\ T_{i'} \\ Y_{e,i'} \\ \alpha_{i'} \end{pmatrix}. \quad (99)$$

At the present resolution with 103 zones, 6 angular bins, and 12 energy groups, the radiation solution vector in step (1), y^{rad} , has the length $i_{\text{max}} \times (2 \times j_{\text{max}} \times k_{\text{max}} + 2) = 15038$ and the hydrodynamics solution vector in step (3), y^{hyd} , has the length $(i_{\text{max}} + 1) \times 8 = 832$. The radiation system is much larger than the hydrodynamics system and dominates the computational effort. The hydrodynamics system with the adaptive grid, however, shows a more complicated coupling between the variables. Common to both cases is that, in one time step, we have to determine the vector y^{n+1} at time $t^{n+1} = t^n + dt$ which solves a nonlinear system of equations, $R(y^n, y^{n+1}; dt) = 0$. The Newton-Raphson scheme is based on the linearization of the system of equations around a guessed solution vector, \tilde{y}^{n+1} ,

$$R(y^n, \tilde{y}^{n+1} + \Delta y; dt) = R(y^n, \tilde{y}^{n+1}; dt) + \frac{\partial R(y^n, \tilde{y}^{n+1}; dt)}{\partial y^{n+1}} \Delta y + O((\Delta y)^2). \quad (100)$$

The residual on the right hand side of Eq. (100) can be neutralized by a specific choice of corrections,

$$\widetilde{\Delta y} = - \left(\frac{\partial R(y^n, \tilde{y}^{n+1}; dt)}{\partial y^{n+1}} \right)^{-1} R(y^n, \tilde{y}^{n+1}; dt). \quad (101)$$

$\tilde{y}^{n+1} + \widetilde{\Delta y}$ is then a better guess because it fulfills

$$R(y^n, \tilde{y}^{n+1} + \Delta y; dt) = 0 + O((\Delta y)^2).$$

This procedure is iterated until a norm of the correction vector $|\Delta y|/y^{n,\text{scl}}$ becomes sufficiently small. In the solution of the radiation system we stop the iterations when the corrections $\Delta(\rho F_{i',j',k'})$, $\Delta e_{i'}/e_{i'}$, and $\Delta Y_{e,i'}/Y_{e,i'}$ are smaller than 10^{-10} . If the radiation is rather stationary, (e.g. in early phases of the gravitational collapse or some time after bounce during neutrino heating), the solution of the transport equation requires about three iterations. Around bounce, the iteration count is typically 4 and may only occasionally reach 6.

Convergence problems appear only at very late time (around a second after bounce, depending on the progenitor model) when the adaptive grid demands tiny mass zones (smaller than $\sim 10^{-4}M_{\odot}$) to resolve the steep density gradient developing at the surface of the protoneutron star. Of order half of the computation time is spent on the construction of the Jacobian $\partial R(y^n, \tilde{y}^{n+1}; dt)/\partial y^{n+1}$, while the other half is required to solve the linear system in Eq. (101). We solve the linear system by direct Gauss elimination. The zone-wise arrangement of the solution vector in Eq. (99) leads to a block-tridiagonal Jacobi matrix because every equation depends on input from at most three adjacent zones. A straightforward solver for band-diagonal matrices (e.g. from Press et al. (1992) or from the LAPACK linear algebra package) works perfectly if the variables and equations are scaled such that the maximum element in each row of the Jacobian is of order unit. A solver for band matrices is not only simpler than a solver for block-tridiagonal matrices, but it adapts even better to the boundary of the off-diagonal blocks because the latter have nonzero coefficients only on their diagonal. Iterative solvers require careful preconditioning to solve the described equations satisfactorily (D’Azevedo et al. 2002). In order to calculate the exact Jacobi matrix, we need derivatives of the equations with respect to all primitive variables. Different methods are used to build the Jacobi matrix for the derivatives with respect to the particle distribution functions, the derivatives with respect to temperature and electron fraction, and the derivatives of the hydrodynamics equations:

The left hand side of the Boltzmann equation (15) is a linear operator on the particle distribution function. Thus, one can inquire Eqs. (54), (57), (62), (77), (81), and (83) for the occurrences of $F_{i'\pm 1, j', k'}$, $F_{i', j'\pm 1, k'}$, and $F_{i', j', k'\pm 1}$. The corresponding prefactors, separately collected, form the contribution to the Jacobian for this part of the transport equation. There are no other dependencies on the left hand side of the transport equation. It requires more tedious efforts to gather the derivatives of the collision term. On the one hand, the interactions can in principle couple all angle bins and energy groups within one zone. On the other hand, blocking factors lead to nonlinear dependencies in some reactions. This applies as well to the derivatives of Eqs. (97) and (98) with respect to particle distribution functions. The coefficients for the Jacobian have to be read off from extensive listings of summations over angle bins and energy groups, as outlined for example in Eq. (67) and (94) in (Mezzacappa & Messer 1999).

Too complicated to be handled manually are the derivatives of the collision term in Eq. (87), Eq. (97), and (98) with respect to temperature and electron fraction. The dynamic table developed in (Mezzacappa & Bruenn 1993a) helps in this case. We illustrate its mechanism with the most simple example, the derivative of the left hand side of Eq. (97)

with respect to temperature,

$$\frac{\partial}{\partial T_{i'}} \left(\frac{e_{i'}^* (\rho_{i'}, T_{i'}, Y_{e,i'}) - \bar{e}_{i'}}{dt} \right). \quad (102)$$

We discretize the three-dimensional space with dimensions ρ , T , Y_e into cubes around the thermodynamical states of the fluid zones $(\rho_{i'}, T_{i'}, Y_{e,i'})$. The eight cube corners

$$\{(\rho_l, T_m, Y_{e,n}), \quad l, m, n = 1, 2\}$$

satisfy

$$\begin{aligned} \log_{10} (\rho_2/\rho_1) &= N_\rho^{-1} \\ \log_{10} (T_2/T_1) &= N_T^{-1} \\ Y_2 - Y_1 &= N_Y^{-1}. \end{aligned}$$

The numbers N_ρ , N_T , N_Y define the resolution of the cube. In our applications, we use $N_\rho = 10$, $N_T = 40$, $N_Y = 50$. If a quantity has to be evaluated as a function of $\rho_{i'}$, $T_{i'}$, and $Y_{e,i'}$, we fetch the cube for zone i' and evaluate the quantity on all eight cube corners if this has not already been done in an earlier cycle. For the evaluation of the internal energy, for example, eight calls to the interactive Lattimer-Swesty equation of state (Lattimer & Swesty 1991) would be required to store the internal energy on the cube corners. The internal energy of the zone is then found by tri-linear interpolation in the logarithmic internal energy,

$$\begin{aligned} \log_{10} e_{i'} &= (1 - C_\rho)(1 - C_T)(1 - C_Y) \log_{10} e(\rho_1, T_1, Y_{e,1}) \\ &+ (1 - C_\rho)(1 - C_T) C_Y \log_{10} e(\rho_1, T_1, Y_{e,2}) \\ &+ (1 - C_\rho) C_T (1 - C_Y) \log_{10} e(\rho_1, T_2, Y_{e,1}) \\ &+ (1 - C_\rho) C_T C_Y \log_{10} e(\rho_1, T_2, Y_{e,2}) \\ &+ C_\rho (1 - C_T)(1 - C_Y) \log_{10} e(\rho_2, T_1, Y_{e,1}) \\ &+ C_\rho (1 - C_T) C_Y \log_{10} e(\rho_2, T_1, Y_{e,2}) \\ &+ C_\rho C_T (1 - C_Y) \log_{10} e(\rho_2, T_2, Y_{e,1}) \\ &+ C_\rho C_T C_Y \log_{10} e(\rho_2, T_2, Y_{e,2}) \end{aligned} \quad (103)$$

where

$$\begin{aligned} C_\rho &= \frac{\log_{10} (\rho_{i'}/\rho_1)}{\log_{10} (\rho_2/\rho_1)} \\ C_T &= \frac{\log_{10} (T_{i'}/T_1)}{\log_{10} (T_2/T_1)} \\ C_Y &= \frac{Y_{e,i'} - Y_{e,1}}{Y_{e,2} - Y_{e,1}}. \end{aligned}$$

The linearity of Eq. (103) makes the determination of the derivatives straightforward. For example, in Eq. (102) we need

$$\frac{\partial e_{i'}}{\partial T_{i'}} = \frac{e_{i'}}{T_{i'}} \frac{\partial \log_{10} e_{i'}}{\partial \log_{10} T_{i'}} = N_T \frac{e_{i'}}{T_{i'}} \frac{\partial \log_{10} e_{i'}}{\partial C_T} \quad (104)$$

where $\partial \log_{10} e_{i'}/\partial C_T$ can simply be read off from Eq. (103). This scheme has important advantages. First, the relation between the values of the interpolated variable and its derivatives inside the cube is exact, both being derived from the same interpolation formula. This helps convergence in the multidimensional Newton-Raphson scheme. Second, the subroutine generating the variable on the cube corners need not be used at each time step, but only if the point $(\rho_{i'}, T_{i'}, Y_{e,i'})$ moves outside the cube, in which case a new, adjacent, cube is generated. As the complexity of the scheme does not depend on the complexity of the function that generates the variable on the cube corner, we apply the scheme to all reaction rates and scattering kernels, whose derivatives with respect to $\rho_{i'}$, $T_{i'}$, and $Y_{e,i'}$ are then straightforward to determine as in the example of Eq. (104). Given that only a few percent of the cubes have to be regenerated during one time step, these dynamic tables enhance the computational efficiency of our method by a factor of ~ 50 . Third, we avoid discontinuous changes in the variables and any of its derivatives, which can be traumatic for a Newton-Raphson scheme. Note, that we occasionally allow extrapolation if the thermodynamic state leaves the cube during the iterations for the solution of the radiation equation in step (1). The cube boundaries are only updated afterwards in the hydrodynamics step (3). In the solution of the hydrodynamics equations, however, we update the cube boundaries for every iteration of the Newton-Raphson scheme. As the hydrodynamics equations only rely on the pressure and internal energy from the equation of state, this is not a computationally expensive measure, although it occasionally deteriorates the convergence behavior of the implicit solution. It is necessary because an extrapolated energy in the converged solution would not necessarily match the interpolated energy after a postponed cube update. This would lead to a violation of energy conservation. This problem does not arise with the internal energy in the solution of the transport equation because only the energy exchange rate, $e_{i'}^{\text{ext}}$, from Eq. (98) is transferred to the hydrodynamics equations in step (3). The extrapolated energy, $e_{i'}^*$, is discarded after step (1).

The Jacobian of the hydrodynamics equations is much smaller. But it has a less regular structure due to the strong nonlinearities in the equations of general relativistic hydrodynamics. Furthermore, the adaptive grid couples changes of all variables to the grid motion, which itself depends on the gradients of the variables. The spatial smoothing operator in the adaptive grid equation couples variables from five adjacent zones. In order to eliminate the considerable risk of producing an erroneous Jacobian in lengthy manual derivations, the hydrodynamics code AGILE constructs the Jacobian automatically by taking numerical

derivatives (Liebendörfer, Rosswog & Thielemann 2002). We start with the evaluation of the residuum vector $R = R(y^n, \tilde{y}^{n+1}; dt)$ based on an initial guess \tilde{y}^{n+1} and define, based on machine precision, a small number ε for the calculation of the numerical derivatives, (Press et al. 1992). Next, we sort the components of the state vector, denoted with label i , into J distinct groups g_j according to the rule that none of the equations R may depend on more than one state vector component out of the same group. We try to choose these groups such that the number of distinct groups is minimized. We select a group g_j and create a variation $\tilde{y}^{var, n+1}$,

$$\begin{aligned}\tilde{y}[i]^{var, n+1} &= \tilde{y}[i]^{n+1} + \varepsilon y[i]^{n, scl} \\ \Delta[i] &= \frac{\tilde{y}[i]^{var, n+1} - \tilde{y}[i]^{n+1}}{y[i]^{n, scl}},\end{aligned}\tag{105}$$

for all components $i \in g_j$. The residuum vector $R^{var} = R(y^n, \tilde{y}^{var, n+1}; dt)$ is then evaluated based on the varied guess. From the two residuals we can extract the components of the Jacobian

$$A[k, i] = y[i]^{n, scl} \frac{\partial R[k](y^n, \tilde{y}^{n+1}; dt)}{\partial y[i]^{n+1}} = \frac{R[k]^{var} - R[k]}{\Delta[i]}\tag{106}$$

for all $i \in g_j$. The Jacobian is complete when this procedure has been performed for all groups J . Finally, we scale the rows of A and the right hand side residuum vector by the maximum component in the row and solve the linear system

$$\sum_i A[k, i] \left(\Delta y[i] / y[i]^{n, scl} \right) = -R[k].\tag{107}$$

to get the corrections Δy for the update of the guess. Again, we use direct Gauss elimination for band-diagonal matrices. Before the next iteration, all zeros in the Jacobian are detected and the sparsity structure is refined. This allows further reduction of the number of required groups for all following time steps. The evaluation of $R^{var} = R(y^n, \tilde{y}^{var, n+1}; dt)$ for a group j is completely independent from the corresponding calculation for a different group $j' \neq j$. In order to compose a complete Jacobian, the system of equations has to be calculated once with the actual guess, and J times in parallel with varied guesses. The hydrodynamics solution usually converges in 3 iterations.

The actual time step is set such that the hydrodynamics variables don't change by more than a percent per time step. For the neutrino distribution functions, it has been most efficient to apply the weak condition $(\rho F - \bar{\rho} \bar{F}) / (\bar{\rho} \bar{F} + 0.1) < 0.1$ combined with a general upper limit of the time step to 0.1 ms. Both radiation transport and hydrodynamics proceed with the minimum time step compatible with any of these conditions. A simulation from 100 ms before bounce to about 600 ms after bounce takes about 12000 time steps. The time steps are smallest around bounce, where they show typical values of 10^{-4} ms.

4. Code Verification

In this section we present a test of the terms and finite difference representations introduced since (Mezzacappa & Bruenn 1993a). First, we investigate the diffusion limit in our finite difference representation and demonstrate that a small diffusive flux is accurate in the presence of a large, nearly isotropic radiation field. We also check the other extreme, the evolution of the radiation moments in a free streaming situation in spherically symmetric geometry. Another test in stationary space-time investigates the implementation of gravitational terms, such as number luminosity conservation, gravitational frequency shift, and gravitational bending. The frequency shift and angular aberration of the radiation field are probed at the shock front, where we relate the discontinuity in radiation quantities in the comoving frame to the smooth radiation field in the view of stationary observers. Then, we investigate the resolution dependence of our results and perform a detailed energy and lepton number conservation analysis to check the overall consistency of our code. Finally, in the intended application of stellar core collapse and postbounce evolution, we compare our results with the independently developed multi-group flux-limited diffusion (MGFLD) code of Bruenn, DeNisco, & Mezzacappa (2001). The latter is based on a sophisticated but approximative treatment of radiative transfer in spherical symmetry and uses a different hydrodynamics code.

4.1. Diffusion limit

The neutrinos in the interior region of the protoneutron star are almost completely trapped. Because of the high electron chemical potential, they equilibrate with matter at high root mean square energies. The neutrino number density multiplied by the speed of light exceeds the neutrino number flux by orders of magnitude. It is therefore essential that the finite difference representation of the Boltzmann equation does not allow errors in the large particle density and pressure to swamp the markedly smaller particle flux. A derivation of the analytical diffusion equation from the Boltzmann equation is the first step in the derivation of a multi-group flux-limited diffusion scheme (Bruenn 1985). We perform here exactly the same procedure, but apply all operations to the finite difference representation of the Boltzmann equation. For simplicity, we assume a stationary background. The particle distribution function is split into an isotropic and a flux component,

$$F_{i',j',k'} = \psi_{i',k'}^0 + \mu_{j'} \psi_{i',k'}^1.$$

We further assume that the flux component is stationary, i.e., that its time dependence in the radiation momentum equation is negligible. We substitute this approximation for

the neutrino distribution function into the finite difference representation of the stationary-state Boltzmann equation, $C_t + D_a + D_\mu + D_E = C_c$, and obtain the radiation momentum equation by the application of the operator $(3/2) \sum_j \mu_{j'} w_{j'}$ and the use of the identity $(3/2) \sum_j \mu_{j'}^2 w_{j'} = 1$:

$$R_a^0 + R_a^1 + R_\mu^0 + R_\mu^1 + R_E^0 = R_c$$

with

$$\begin{aligned} R_a^0 &= \frac{2\pi}{\alpha_{i'} da_{i'}} \left[r_{i+1}^2 (\alpha_{i'} \rho_{i'} \psi_{i',k'}^0 + \alpha_{i'+1} \rho_{i'+1} \psi_{i'+1,k'}^0) \right. \\ &\quad \left. - r_i^2 (\alpha_{i'-1} \rho_{i'-1} \psi_{i'-1,k'}^0 + \alpha_{i'} \rho_{i'} \psi_{i',k'}^0) \right] \\ R_a^1 &= \frac{-3\pi}{2\alpha_{i'} da_{i'}} \left[r_{i+1}^2 (1 - 2\beta_{i+1,k'}) (\alpha_{i'} \rho_{i'} \psi_{i',k'}^1 - \alpha_{i'+1} \rho_{i'+1} \psi_{i'+1,k'}^1) \right. \\ &\quad \left. - r_i^2 (1 - 2\beta_{i,k'}) (\alpha_{i'-1} \rho_{i'-1} \psi_{i'-1,k'}^1 - \alpha_{i'} \rho_{i'} \psi_{i',k'}^1) \right] \\ R_\mu^0 &= -2\Upsilon_{i+1} \psi_{i',k'}^0 \\ R_\mu^1 &= 3\Upsilon_{i+1} \sum_j \mu_{j'} [(1 - \gamma_{i',k'}) \zeta_{j+1} (\mu_{j'+1} - \mu_{j'}) + \gamma_{i',k'} \zeta_j (\mu_{j'} - \mu_{j'-1})] \psi_{i',k'}^1 \\ R_E^0 &= -\frac{G_{i+1}^E}{E_{k'}^2 dE_{k'}} \left(\frac{dE_{k'-dk}}{E_{k'} - E_{k'-dk}} E_{k'-dk}^3 \psi_{i',k'-dk}^0 - \frac{dE_{k'}}{E_{k'+dk} - E_{k'}} E_{k'}^3 \psi_{i',k'}^0 \right) \\ R_c^1 &= -\chi_{i',k'} (\rho_{i'}, T_{i'}^*, Y_{e,i'}^*) \psi_{i',k'}^1. \end{aligned} \tag{108}$$

The simple expression R_μ^0 results from the specific property (63) of the angular difference coefficients. The radial dependence of $\beta_{i,k'}$ in Eq. (56) can lead to an asymmetric treatment of ingoing and outgoing particles, producing the numerical term R_a^1 . Also R_μ^1 arises as an unwanted term with no analytical correspondence. It is therefore essential to set the transport coefficients in the diffusive regime precisely to $\beta_{i,k'} = 1/2$. With the choice in Eq. (56) we immediately find $R_a^1 = 0$. Also R_μ^1 vanishes because the term under the sum over j becomes antisymmetric with $\gamma_{i',k'} = \beta_{i',k'} = 1/2$. For the next step, we need a more concise notation for the difference and average of a zone edge variable, V :

$$\begin{aligned} d\langle V \rangle_{i'} &= V_{i+1} - V_i \\ \langle V \rangle_{i'} &= \frac{1}{2} (V_{i+1} + V_i). \end{aligned}$$

For zone center variables, we use the analogous definitions, e.g. $d\langle \alpha \rho \psi_{k'}^0 \rangle_i = \alpha_{i'} \rho_{i'} \psi_{i',k'}^0 - \alpha_{i'-1} \rho_{i'-1} \psi_{i'-1,k'}^0$. With these, we may rewrite the terms R_a^0 and R_μ^0 as

$$\begin{aligned} R_a^0 &= \frac{d\langle 4\pi r^2 \rangle_{i'}}{da_{i'}} \rho_{i'} \psi_{i',k'}^0 + \frac{4\pi}{da_{i'}} \frac{1}{2\alpha_{i'}} \left[r_{i+1}^2 d\langle \alpha \rho \psi_{k'}^0 \rangle_{i+1} + r_i^2 d\langle \alpha \rho \psi_{k'}^0 \rangle_i \right] \\ R_\mu^0 &= -\left(\Gamma_{i+1} \frac{3d\langle r^2 \rangle_{i'}}{2d\langle r^3 \rangle_{i'}} - G_{i+1}^\mu \right) 2\psi_{i',k'}^0. \end{aligned} \tag{109}$$

If the hydrodynamics equations relate the rest mass element to the volume element by $\Gamma_{i+1} da_{i'} = (4\pi/3) \rho_{i'} d\langle r^3 \rangle_{i'}$, the first term in R_a^0 cancels with the first term in R_μ^0 . Finally we try to extract the lapse function α from the gradient in the remainder of R_a^0 ,

$$\frac{4\pi}{da_{i'}} \frac{1}{\alpha_{i'}} \langle r^2 d\langle \alpha \rho \psi_{k'}^0 \rangle \rangle_{i'} = \frac{1}{da_{i'} \alpha_{i'}} \langle 4\pi r^2 \langle \rho \psi_{k'}^0 \rangle d\alpha \rangle_{i'} + \frac{1}{da_{i'} \alpha_{i'}} \langle 4\pi r^2 \alpha d\langle \rho \psi_{k'}^0 \rangle \rangle_{i'},$$

and find for the diffusion limit in the finite difference representation

$$R_a'^0 + R_\mu'^0 + R_E^0 = R_c$$

with

$$\begin{aligned} R_a'^0 &= \frac{1}{\alpha_{i'} da_{i'}} \langle 4\pi r^2 \alpha d\langle \rho \psi_{k'}^0 \rangle \rangle_{i'} \\ R_\mu'^0 &= \frac{1}{\alpha_{i'} da_{i'}} \langle 4\pi r^2 \langle \rho \psi_{k'}^0 \rangle d\alpha \rangle_{i'} + G_{i+1}^\mu 2\psi_{i',k'}^0 \\ R_E^0 &= -\frac{G_{i+1}^E}{E_{k'}^2 dE_{k'}} \left(\frac{dE_{k'}-dk}{E_{k'} - E_{k'-dk}} E_{k'-dk}^3 \psi_{i',k'-dk}^0 - \frac{dE_{k'}}{E_{k'+dk} - E_{k'}} E_{k'}^3 \psi_{i',k'}^0 \right) \\ R_c^1 &= -\chi_{i',k'}(\rho_{i'}, T_{i'}^*, Y_{e,i'}^*) \psi_{i',k'}^1. \end{aligned} \quad (110)$$

If we compare this to the analytic radiation momentum equation in the diffusion limit,

$$4\pi r^2 \frac{\partial}{\partial a} (\rho K^N(E)) + 4\pi r^2 \frac{1}{\alpha} \frac{\partial \alpha}{\partial a} \rho J^N(E) - \frac{\Gamma}{\alpha} \frac{\partial \alpha}{\partial r} \frac{\partial}{E^2 \partial E} (E^3 K^N(E)) = -\chi H^N(E), \quad (111)$$

where we have set $J - 3K = 0$, we can identify the physical meaning of all remaining terms. The diffusive flux ψ^1 appearing in R_c^1 is determined by the opacity χ and operators acting on the particle density. The term in $R_a'^0$ describes the flux generated by a gradient in the particle density. It is the only term that survives in the Newtonian limit. In full general relativity, we have an additional gravitational force acting on the radiation particles. It contributes to the particle flux and is described in the term $R_\mu'^0$. Its analytical analogue is $R_\mu'^0 = 3(\Gamma/\alpha)(\partial\alpha/\partial r)\psi^0$. The factor of three stems from our choice $3\psi^0 = 3K = J$.

The term R_E^0 corrects for the fact that the gradient in $R_a'^0$ has been taken at constant local particle energy instead of constant particle energy at infinity. The terms $R_a'^0$ and R_c^1 emerge in a perfect way from our finite difference representation because of the special measures taken in the finite difference representation of the propagation terms D_a and D_μ in (Mezzacappa & Bruenn 1993a). However, the requirement of global energy conservation ties the finite difference representation of this basic choice to many other terms, as outlined in table (37). These constraints impose a rather obscure finite differencing in the diffusive limit for the general relativistic corrections $R_\mu'^0$ and R_E^0 . However, each term is recognizable as a finite difference representation of a physical term. If we integrate the corrections over energy,

the contributions from R_E^0 are guaranteed to vanish. We therefore focus on the remaining correction R_μ^0 . In order to ensure a vanishing flux in equilibrium, it remains to be shown that the results from our finite difference representation do not significantly deviate from a natural finite difference representation of Eq. (111), which becomes after an integration over energy,

$$\frac{4\pi r^2}{\alpha^3} \frac{\partial}{\partial a} (\alpha^3 \rho K^N) = -\chi H^N. \quad (112)$$

To this purpose, we collect from Eq. (110) the finite difference representations

$$\begin{aligned} \frac{\rho_{i'}}{\Gamma_{i+1}} dr_{i'} R_a^0 &= \frac{3}{4\pi (r_{i+1}^2 + r_{i+1} r_i + r_i^3) \alpha_{i'}} \langle 4\pi r^2 \alpha d \langle \rho \psi^0 \rangle \rangle_{i'} \\ \frac{\rho_{i'}}{\Gamma_{i+1}} dr_{i'} R_\mu^0 &= \frac{3}{4\pi (r_{i+1}^2 + r_{i+1} r_i + r_i^3) \alpha_{i'}} \langle 4\pi r^2 \langle \rho \psi^0 \rangle d\alpha \rangle_{i'} \\ &+ (r_{i+1} - r_i) G_{i+1}^\mu 2 \frac{\rho_{i'} \psi_{i'}^0}{\Gamma_{i+1}} \end{aligned} \quad (113)$$

and compare their sum with the natural finite difference representation of Eq. (112),

$$\frac{1}{\alpha_i^3} d \langle \alpha^3 \rho \psi_{k'}^0 \rangle_i. \quad (114)$$

The comparison is performed in a time slice in the evolution of the 40 M_\odot progenitor of (Woosley & Weaver 1995) at 400 ms after bounce. We force the hydrodynamics to be static and evaluate the finite difference expressions (113) and (114) in the high density region, where the diffusion limit is valid and gravitational terms sizeable. We find in Figure (10) that the terms stemming from R_a^0 (dashed line) and R_μ^0 (dash-dotted line) compose a sum (solid line) that agrees well with the more accurate finite difference representation given in Eq. (114). Thus, we conclude that the opacities safely determine the diffusive flux in our finite difference representation of the Boltzmann equation.

4.2. Redshift, gravitational bending, and the evolution of angular moments

In this subsection we test free streaming in spherically symmetric geometry. This is the opposite limit to the diffusion investigated in the previous subsection. For the time being, we stay with our stationary time slice at 400 ms after bounce, but focus on radii larger than 40 km. Outside this radius, we switch all interactions between the radiation field and matter off. This facilitates the comparison of the neutrino density, neutrino number flux, and neutrino luminosity with the analytical behavior. Unlike in the Newtonian limit, they are subject to time lapse, gravitational frequency shift, and gravitational bending.

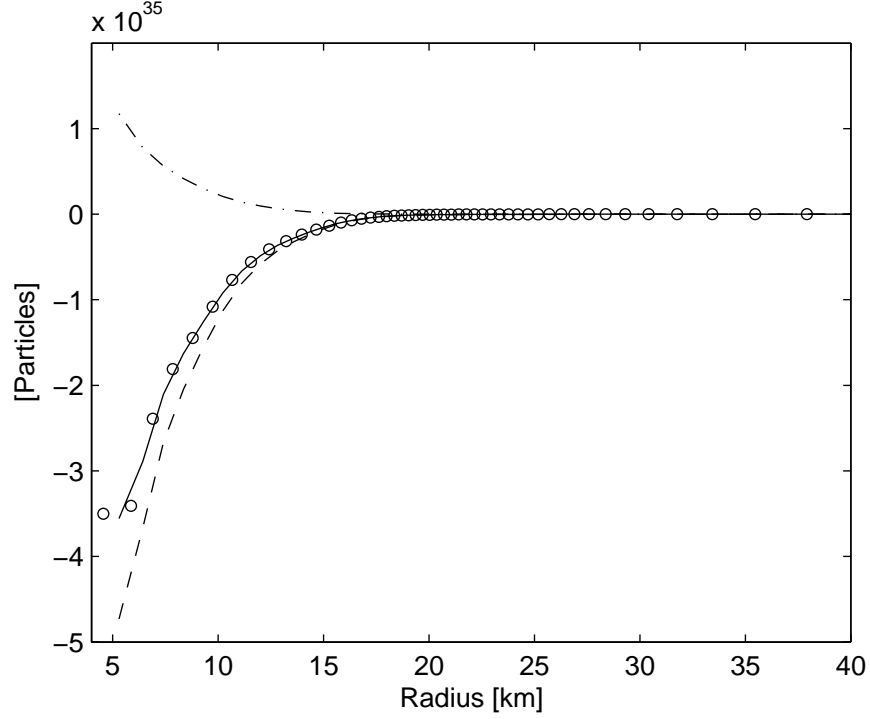


Fig. 10.— The sum of the terms R_a^0 and R_μ^0 in Eq. (110) determines the diffusive flux in the discrete Boltzmann equation. We check these terms in a stationary-state situation at 400 ms after bounce in the 40 M_\odot model. Plotted are the contributions from R_a^0 (dashed line) and R_μ^0 (dash-dotted line) as determined in Eq. (113) from our finite differencing of the Boltzmann equation. Their sum (solid line) is compared with a straightforward finite difference representation of the same quantity (circles) according to Eq. (114) (The circle at 5 km radius is the zone edge of our innermost zone, the other quantities are evaluated on zone centers). The agreement demonstrates that we obtain an accurate diffusion flux in the numerical solution of the Boltzmann equation.

For a stationary neutrino flux in the free streaming limit, Eq. (24) expresses particle number conservation

$$\frac{\partial}{\partial a} [4\pi r^2 \alpha \rho H^N] = 0. \quad (115)$$

Figure (11) shows the radial dependence of the locally observed neutrino number luminosity $4\pi r^2 \rho H^N$ (dashed line) and the conserved number luminosity $4\pi r^2 \alpha \rho H^N$ (solid line). We find that the latter is constant to machine precision as required by Eq. (115). This is the direct result of our finite differencing of the term D_a , because we have placed the lapse function α inside the space derivative. The lapse function in the bracket converts the locally advected particle number per proper time to the particle advection per global coordinate time. There is a similar equation for the conservation of the energy luminosity. Eq. (30) for the particle energy carries a second lapse function inside the spatial derivative from the gravitational frequency shift,

$$\frac{\partial}{\partial a} [4\pi r^2 \alpha^2 \rho H] = 0. \quad (116)$$

Figure (12) shows the radial dependence of the locally observed luminosity $4\pi r^2 \rho H$ (dashed line), the luminosity with the time lapse correction only, $4\pi r^2 \alpha \rho H$ (dash-dotted line), and the conserved luminosity, $4\pi r^2 \alpha^2 \rho H$, with the gravitational redshift included. We see again, that the latter is fairly constant in the interaction free region. Unlike the number luminosity, the conservation of energy luminosity is not automatically fulfilled by the finite difference representation, and small deviations can be observed. As the local mean energies of the moving particles are determined by the ratio of energy and number flux, we may conclude from the fulfillment of Eqs. (115) and (116) that, in this regime, the gravitational energy shift of the particles is accurately implemented.

In order to fully constrain the redshift, gravitational bending, and evolution of the angular moments, we need to test the radial dependence of a third quantity. Most appropriate is the particle number density. However, some special care is necessary to clearly separate the following three effects on the angular neutrino distribution: (i) gravitational bending, (ii) the changing opening angle as a function of the geometric distance from the source, (iii) the numerical bending caused by limited angular resolution in our finite difference method. We find an analytical expression for the radial dependence of the particle density by applying the operator $\int dE d\mu E^2 \mu^{-1}$ to the interaction-free stationary state limit of the Boltzmann equation (15),

$$\begin{aligned} & \frac{\partial}{\alpha \partial a} (4\pi r^2 \alpha \rho J^N) + \Gamma \left(\frac{1}{r} - \frac{1}{\alpha} \frac{\partial \alpha}{\partial r} \right) \times \\ & \left(4 \int F(\mu = 0) E^2 dE - \int [F - F(\mu = 0)] E^2 dE \frac{1 - \mu^2}{\mu^2} d\mu \right) = 0. \end{aligned} \quad (117)$$

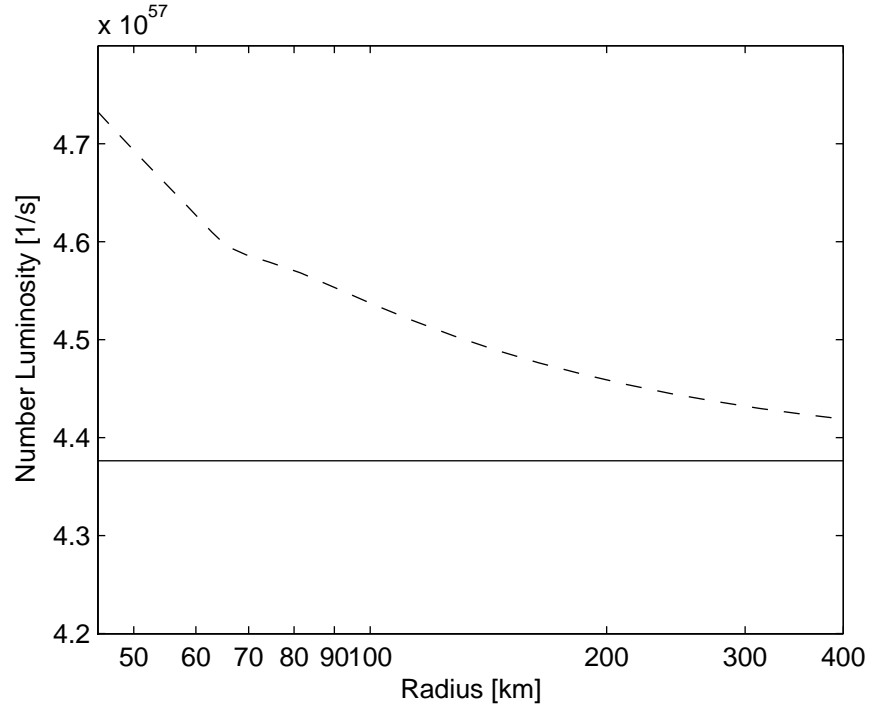


Fig. 11.— Shown are the radial variations in the locally observed neutrino number luminosity $4\pi r^2 \rho H^N$ (dashed line) and the conserved number luminosity $4\pi r^2 \alpha \rho H^N$ (solid line) in a stationary-state situation at 400 ms after bounce in the 40 M_\odot model. Eq. (115) is fulfilled by construction.

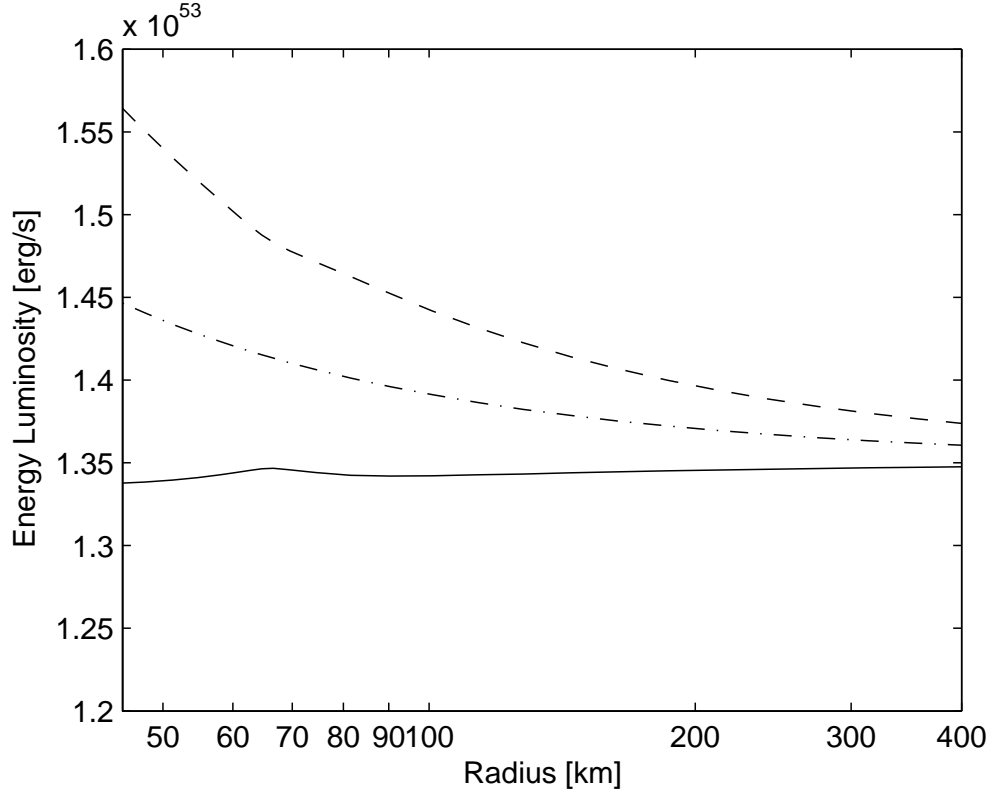


Fig. 12.— Shown are the energy luminosities $4\pi r^2 \rho H$ (dashed line), $4\pi r^2 \alpha \rho H$ (dash-dotted line), and $4\pi r^2 \alpha^2 \rho H$ (solid line) as functions of radius in a stationary-state situation at 400 ms after bounce in the $40 M_\odot$ model. Deviations from Eq. (116) do not exceed 1.5% in the third expression for the luminosity, which is expected to be conserved. The other two expressions illustrate that the gravitational effects contribute substantially in this test.

As before, we may compare this to our finite difference representation. The application of the operator $\sum dE_{k'} w_{j'} E_{k'}^2 \mu_{j'}^{-1}$ to the finite difference representation of the Boltzmann equation leads to

$$\begin{aligned} & (4\pi r_{i+1}^2 \alpha_{i+1} \rho_{i+1} J_{i+1}^N - 4\pi r_i^2 \alpha_i \rho_i J_i^N) = \\ & -\alpha_{i'} \Upsilon_{i+1} \sum F_{i',j,k'} da_{i'} E_{k'}^2 dE_{k'} \frac{\zeta_j}{\mu_{j'} \mu_{j'-1}} (\mu_{j'} - \mu_{j'-1}). \end{aligned} \quad (118)$$

Here, $\alpha_i \rho_i J_i^N$ is interpolated according to Eq. (58) and $F_{i',j,k'}$ according to Eq. (64). Figure (13) compares the left hand side of Eq. (118) (circles) to the right hand side (solid line), evaluated in our 400 ms post bounce time slice. The match is to machine precision; it demonstrates that we made no errors in the derivation of Eq. (118) or its implementation. We split this quantity into the contribution from geometric changes according to the opening angle of the source, proportional to Γ/r , (dashed line) and the gravitational bending, proportional to $(\Gamma/\alpha)(\partial\alpha/\partial r)$, (dash-dotted line). Because the latter is much smaller, we exclude the gravitational bending contribution to Υ as a primary source of uncertainties. We can then focus on the comparison of the analytical integral in Eq. (117) with its finite difference representation in Eq. (118). We start with a more accurate numerical evaluation of the integral in Eq. (117) in order to compare with Eq. (118) in our time slice. The application of a Gaussian quadrature in Eq. (117) converts the integral to the sum

$$-\alpha_{i'} \Upsilon_{i+1} \left(4 \sum F(0)_{i',k'} E_{k'}^2 dE_{k'} - \sum [F_{i',j',k'} - F(0)_{i',k'}] da_{i'} E_{k'}^2 dE_{k'} \frac{1 - \mu_{j'}^2}{\mu_{j'}^2} w_{j'} \right) \quad (119)$$

The result of Eq. (119) depends quite sensitively on the choice of the distribution function in the tangential direction, $F(0)_{i',k'}$. We determine it here by the maximum entropy model for Maxwell-Boltzmann statistics in angle space,

$$F_{j'} = A \exp(B\mu_{j'}), \quad (120)$$

(see e.g. (Smit, van den Horn, & Bludman 2000) for an overview on maximum entropy closures). The zeroth and second moments of Eq. (120) define the flux factor, $h = H/J$, as a function of the parameters A and B ,⁸

$$\begin{aligned} J &= \frac{2A}{B} \sinh(B) \\ h &= \coth(B) - \frac{1}{B}, \end{aligned} \quad (121)$$

⁸Note that our definition of moments in Eq. (23) is twice as large as in standard references because this leads to more consistency between our code and its description.

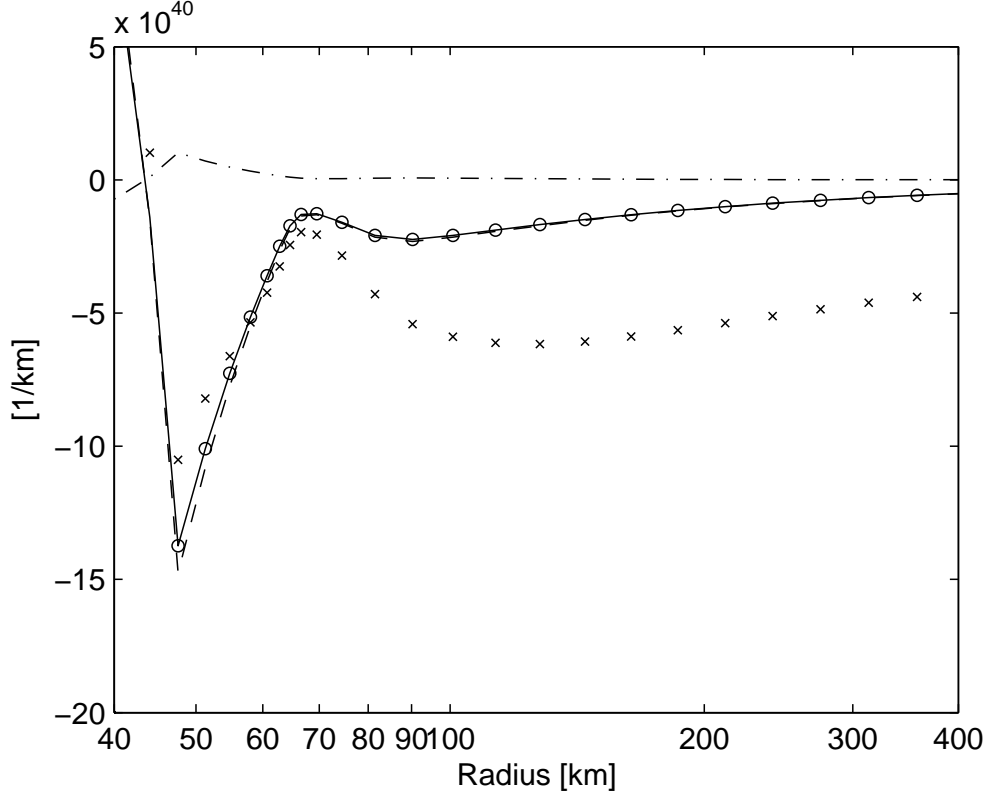


Fig. 13.— This figure shows radial increments of the particle number density (actually plotted is the difference in the particle density across a zone, multiplied by $4\pi r^2$). The particle number luminosity is constant in the free streaming limit and the changes in the particle density depends on the angular distribution of the radiation field. The dashed line shows the changes induced by the increasing distance to the neutrino source in Newtonian geometry. The dash-dotted line shows the contribution from gravitational bending. The sum (solid line) represents the right hand side of Eq. (118). It exactly matches the left hand side (circles). This indicates a correct derivation and implementation. However, the crosses mark a more accurate solution to the right hand side of Eq. (117) than the finite differencing imposed by the discrete Boltzmann equation. It has been evaluated according to Eq. (119). The discrepancy is moderate at flux factors $h < 0.75$ and large far from the source where h should converge to 1.

We derive the free parameters A and B by the inversion of Eq. (121) from the zeroth and first angular moments of the numerically obtained neutrino distribution function and define $F(0)_{i',k'} = A_{i',k'}$. The result is shown with cross markers in Fig. (13). We observe comparable values between the two finite difference representations (118) and (119) at smaller radius, where the flux factor is smaller (~ 0.75). Large differences are found at larger radii, where the flux factor would be expected to be close to one. I.e., the primary source of inaccuracy in the particle density stems from the fact that the sum over angles on the right hand side of the finite difference Eq. (118) is a poor representation of the angle integral in the analytic Eq. (117).

In order to study this discrepancy in more detail, we construct a series of analytical particle distribution functions according to the maximum entropy model in Eq. (120) with $B = \{0, 1, 2, 5, 10\}$. This corresponds to flux factors of $h = \{0, 0.31, 0.54, 0.8, 0.9\}$. Then, we evaluate the integral on the right hand side of Eq. (118) in different ways. First, as given by the finite differencing in Eq. (118) itself, then, with the more natural Gauss quadrature in Eq. (119), and finally by an analytic integration. The analytic integration yields

$$\begin{aligned} & \frac{1}{J} \int_{-1}^1 \frac{1}{\mu} \frac{\partial}{\partial \mu} [(1 - \mu^2) A \exp(B\mu)] d\mu = \\ & -2 - Bh + \frac{B^2}{\sinh(B)} \left(B + \frac{B^3}{3 \cdot 3!} + \frac{B^5}{5 \cdot 5!} + \frac{B^7}{7 \cdot 7!} + \dots \right). \end{aligned} \quad (122)$$

The result for different flux factors and angular resolutions is shown in Table (3). We find quite poor convergence for the evaluation of the integral as it emerges from the finite differencing in the Boltzmann equation. The comparison with the center block, where no upwind differencing was used for the advection terms, demonstrates that the advective terms play a major rôle in the accuracy of the representation of this integral. A forward peaked radiation field shows a steep gradient in the angular distribution. The choice of upwind differencing always underestimates the advective flux at the edge of the angular zone. This is necessary for the stability of the scheme for arbitrary large time steps, but can lead to a substantial underestimation of the integral in Eq. (117). The most populated forward bin, for example, never contributes to the integral. The distribution function asymptotically approaches a highly populated forward bin while all other angular bins are emptied. The maximum achievable flux factor is smaller than one. Although higher angular resolution improves the situation, it does not eliminate this systematic effect. The choice of a higher order advection scheme in angular space might be promising. More rigorous, however, appears the implementation of an adaptive angular grid in the transparent regime (Yamada, Janka, & Suzuki 1999). It would be designed to minimize the advective flow in angle space such that the undesired effects are eliminated at the root. This difficulty with angular advection does not occur in methods that solve a model Boltzmann equation along particle characteristics to

	B	flux factor	$j_{\max}=6$	$j_{\max}=12$	$j_{\max}=48$	analytical
Eq. (118)	0	0	-2.00	-2.00	-2.00	-2.00
	1	0.31	-1.10	-1.23	-1.36	-1.41
	2	0.54	-0.21	-0.22	-0.28	-0.32
	5	0.80	0.28	0.47	0.68	0.77
	10	0.90	0.06	0.14	0.26	0.31
Eq. (118),	0	0	-2.00	-2.00	-2.00	-2.00
but no	1	0.31	-1.48	-1.43	-1.41	-1.41
upwind	2	0.54	-0.47	-0.36	-0.32	-0.32
diff.	5	0.80	0.66	0.74	0.77	0.77
	10	0.90	0.27	0.30	0.31	0.31
Eq. (119)	0	0	-2.00	-2.00	-2.00	-2.00
	1	0.31	-1.41	-1.41	-1.41	-1.41
	2	0.54	-0.32	-0.32	-0.32	-0.32
	5	0.80	0.77	0.77	0.77	0.77
	10	0.90	0.32	0.31	0.31	0.31

Table 3: This table investigates the accuracy of the integral on the right hand side of Eq. (117) in a parameter study based on analytic distribution functions with different flux factors. The result of the numerical integrations are given for discretizations with $j_{\max} = 6$, $j_{\max} = 12$, and $j_{\max} = 48$ angular bins. The uppermost block shows the evaluation according to Eq. (118). It emerges from the chosen finite differencing of the term D_μ in Eq. (62) and converges only slowly to the exact solution. The center block shows the same evaluation without upwind differencing for the advected F (i.e. with $\gamma_{i',k'} = 0.5$). The convergence is much better in this case. The lowermost block shows the evaluation based on the more natural Gauss quadrature (119), which converges very rapidly to the exact result.

close the system of radiation moments equations with a variable Eddington factor (Burrows et al. 2000; Rampp & Janka 2002). An independent and much smaller source of inaccuracy stems from the fact that the integral in Eq. (118) is not written as a sum over a function evaluated at Gaussian quadrature points and multiplied with Gaussian weights. Hence, it does not take profit from the fast convergence of Gaussian quadrature. This can be seen if the result is compared with the evaluation based on the Gaussian quadrature as shown in the third block in Table (3).

In our supernova application, however, stationary-state convergence tests have shown that 6 angle Gaussian quadrature produces physically reasonable results (Messer et al. 1998; Messer 2000). We confirm this in section 4.5 in a comparison with a dynamical run discretized with 12 angular bins. In the regions of free streaming, where numerical angular diffusion becomes apparent, the neutrino field is already decoupled from the matter and does not influence the dynamical evolution anymore.

4.3. Observer corrections

For the check of the observer corrections, we go back to the original solution at 400 ms after bounce. Both, the neutrino luminosities and rms energies show a discontinuity across the shock front because of the Doppler effect and angular aberration. In the laboratory frame of a distant observer, however, the radiation field should not be affected by the shock. We may therefore test the implementation of the observer corrections by transforming the electron neutrino luminosity and rms energy from our comoving frame to the rest frame. In (Liebendörfer, Mezzacappa, & Thielemann 2001) we determined for the particle propagation angle, μ^S , and particle energy, E^S , in Schwarzschild coordinates the relationship

$$\begin{aligned} (1 - \mu^{S2}) (\Gamma^S)^{-2} &= (1 - \mu^2) (\Gamma + u\mu)^{-2} \\ \Gamma^S E^S &= (\Gamma + u\mu) E, \end{aligned} \quad (123)$$

where $\Gamma^S = (1 - 2m/r)^{1/2}$. Assuming free outwards streaming with transport coefficients $\beta = 1$ in the interesting region around the shock, we evaluate for the luminosity, L^S , and rms energy, $\langle E^S \rangle$, the finite difference expression

$$\begin{aligned} L_i^S &= 4\pi r_i^2 \frac{2\pi}{(hc)^3} \sum_{j,k} \rho_{i'-1} F_{i'-1,j,k} E_{i',j',k'}^S E_{k'}^2 dE_{k'} \mu_{i',j'}^S c w_{j'} \\ \langle E^S \rangle_{i'} &= \left(\sum_{j,k} (E_{i',j',k'}^S)^2 F_{i',j',k'} E_{k'}^2 dE_{k'} w_{j'} \right)^{\frac{1}{2}} \left(\sum_{j,k} F_{i',j',k'} E_{k'}^2 dE_{k'} w_{j'} \right)^{-\frac{1}{2}}. \end{aligned} \quad (124)$$

The result is shown in Figure (14). The solid line is the luminosity in the rest frame according

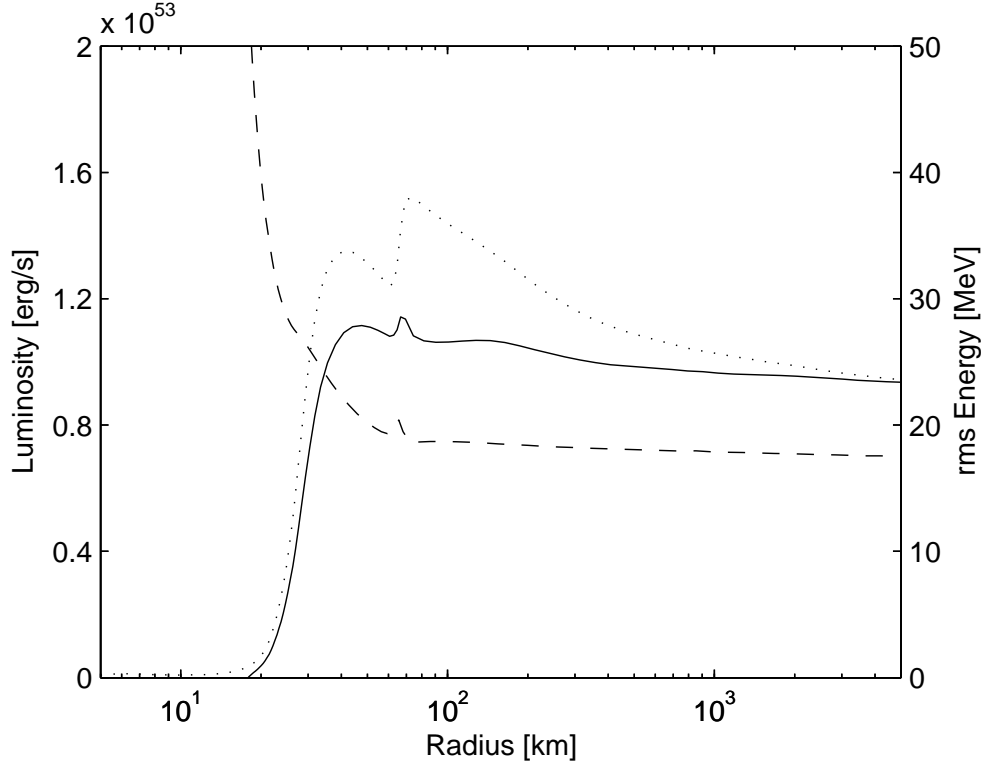


Fig. 14.— Shown are the electron neutrino luminosity (solid line) and rms energy (dashed) line after the transformation from the comoving frame to the rest frame of a distant observer in the evolution of the $40 M_{\odot}$ model at 400 ms after bounce. Aside of a local bump, the two profiles show the expected continuous transition at the shock front. Also shown is the luminosity in the comoving frame (dotted line) to illustrate the effect of the transformation.

to Eq. (124). The dotted line shows the luminosity in the comoving frame for comparison. We find that the luminosity profile shows a numerical local distortion on top of the shock front. However, if we compare the left hand side values with the right hand side values, we find the expected disappearance of the discontinuity, indicating that the observer corrections in the comoving frame are well represented. The same behavior can be seen in the rms energies.

4.4. Radiation pulse propagation

We have now performed many checks of the particle transport in stationary-state situations. In this subsection, we check the dynamics of the radiation field itself. The neutrino transport in the supernova is most dynamic when the shock crosses the neutrinosphere. As soon as the shock has propagated to densities where the opacities are low enough that neutrinos can escape from the hot material behind the shock, immediate electron capture will occur to refill the emptied phase space with new electron neutrinos. A neutrino burst carries an energy of order 10^{51} erg throughout the star towards the distant observer. Although the neutrino burst is not completely interaction free, it is an excellent example for a time-dependent radiation field where pulse propagation can be studied. We do this by plotting the luminosity profiles at selected times after the launch of the neutrino burst. We shift the radial coordinate, r , in each time slice by the amount a free massless neutrino would have propagated during the time t since bounce, $r' = r - ct$. With an ideal numerical solution to free propagation (and assuming a point source), we would expect congruent pulse shapes from each time slice at the same positions r' . Figure (15) shows the neutrino burst with the described radius adjustment in the evolution of the $40 M_{\odot}$ progenitor. We first observe, that the position of the pulse is fairly stationary. Therefore, the pulse indeed travels with speed of light through the star. However, we also observe that the shape of the pulse broadens considerably with ongoing time. From the check of the neutrino number luminosity conservation in Fig. (11), we already know that the number and energy of the emitted neutrinos is conserved during their propagation to larger radii. The broadening is likely to occur by artificial diffusion in our numerical finite differencing scheme. Indeed, from considerations in (Liebendörfer, Rosswog & Thielemann 2002) we remember that first order upwind differencing introduces a numerical diffusivity proportional to the advection speed and zone width,

$$D_{i'} = c \Delta r_{i'}. \quad (125)$$

We quantify the influence of this effect to the evolution of our neutrino pulse by approximating the diffusion between the time steps with $\Delta L \simeq D (\partial^2 L / \partial r^2) \Delta t$. We evaluate the diffusivity (125) and the second derivative of the luminosity at the pulse peak in the first

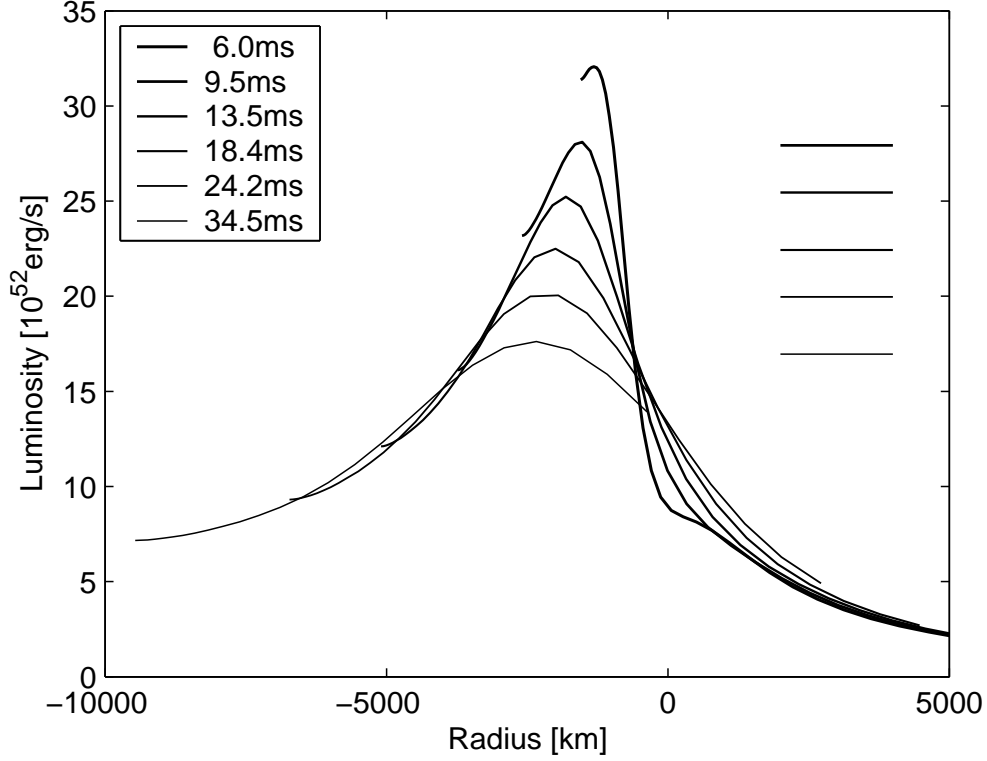


Fig. 15.— Shown is the radial profile of the electron neutrino luminosity at different times when the neutrino burst propagates through the star ($40 M_{\odot}$ model). The radial coordinate of each time slice has been shifted to the left by the distance a signal with light speed would have traveled since bounce. This makes the pulse profile roughly stationary in position. The levels on the right hand side in the graph give estimates of the peak height for the next time slice. The evaluation is based on the estimated numerical diffusion from first order upwind differencing in the free streaming regime in the transport equation. The expected peak heights accurately explain the visible decay in the luminosity pulse.

time slice. The time span Δt to the next time slice gives us an estimate ΔL for the change of the peak luminosity. We subtract ΔL from the pulse height and draw a horizontal line on the right hand side in Fig. (15) at this estimated peak level for the next time slice. The close to perfect agreement with the numerically evolved pulse height leads to the conclusion that the diffusivity (125) introduced with the low order advection scheme fully accounts for the observed pulse broadening. The resolution study in the next section illustrates that this is the dominant effect.

4.5. Resolution

In spite of our ambition to produce accurate results already at low resolution, the reader has been left wondering about the actual resolution dependence of our data. In this subsection, we demonstrate reasonable convergence of our results by separately doubling the resolution in each phase space dimension in otherwise identical simulations. Historically, our standard resolution with 103 adaptive zones, 6 angular bins, and 12 energy groups formed as the minimum resolution where we felt safe about our physical conclusions. In Fig. (16) we compare the results with a simulation that uses 206 adaptive zones, one that uses 12 angular bins, and one that uses 24 energy groups. We focus on the quantities and instances where we find the largest deviations. We start with two limitations that are well-known. Graph (a) shows the mean flux factor at 100 ms after bounce in the neutrino heating phase. It can clearly be seen, that the run with 12 angular bins determines the flux factor with more accuracy in the free streaming limit (Messer et al. 1998; Yamada, Janka, & Suzuki 1999). The angular resolution determines how close to the radial direction the most forward peaked angular bins are. The closer they are the larger is the asymptotic limit of the flux factor. In graph (b), we show another previously documented effect (Mezzacappa & Bruenn 1993b). In the last half of a millisecond before bounce, insufficient resolution of the energy phase space leads to a poor representation of the Fermi energy in the degenerate neutrino gas when the trapped neutrinos are compressed to high densities. The consequence are rapid and transient local displacements of neutrinos. At poor energy resolution, the Fermi energies rather increase in steps than continuously, and the neutrino fluxes try to balance the numerical variations in the Fermi energies between adjacent zones. Therefore, the effect is best seen in the electron neutrino luminosities as shown in graph (b). While the conserved lepton number cannot show numerical variations, the electron fraction and neutrino abundances also reflect the transient steps in the Fermi energies. Variations in these quantities are of order 5%. However, because the neutrinos are trapped and because our scheme is conservative, this transient wiggles do not lead to any differences that survive bounce.

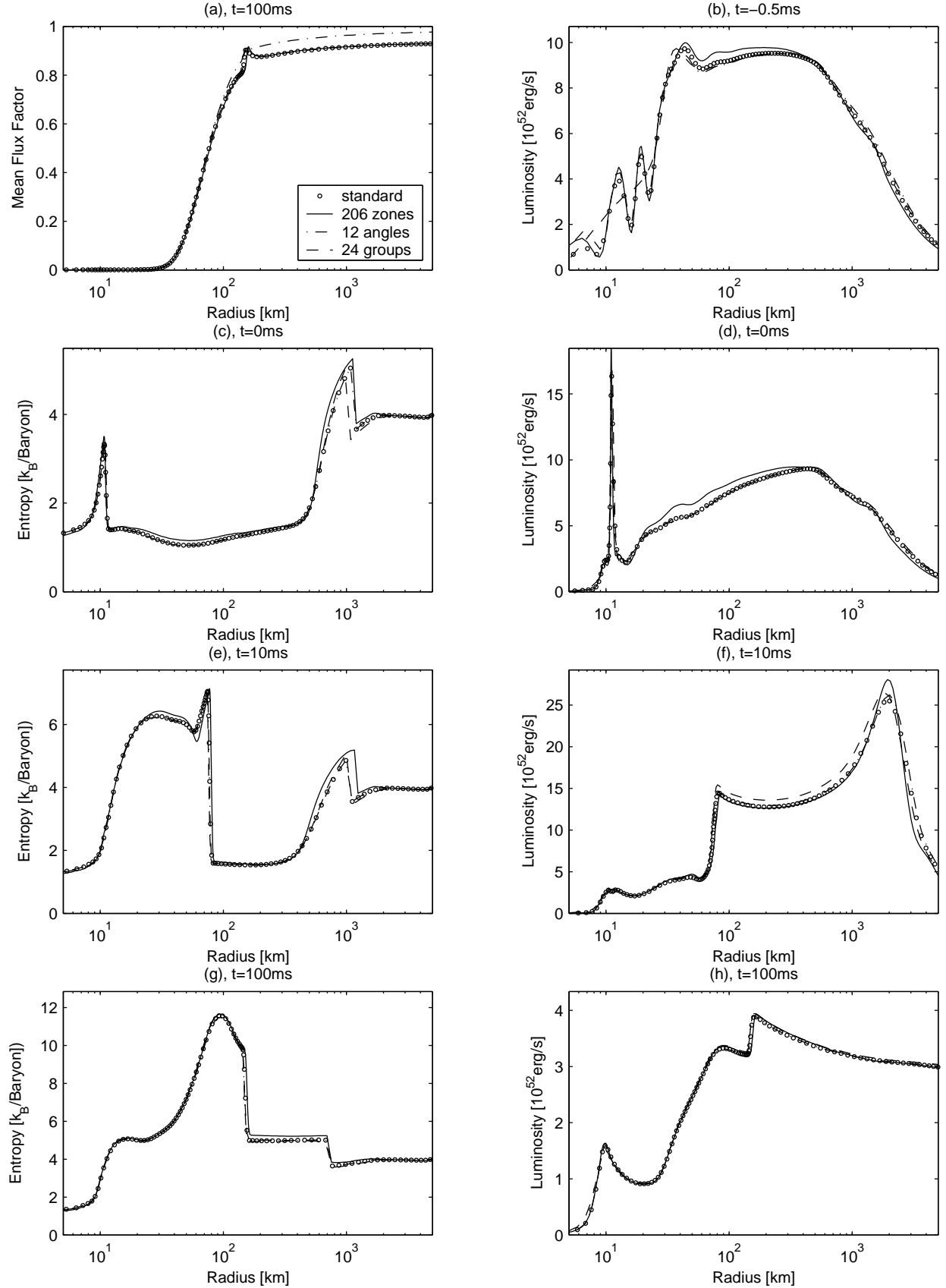


Fig. 16.— Resolution dependence of the results. The standard run (circles) was calculated with 103 adaptive zones, 6 angular bins, and 12 energy groups. We compare with runs with

This is shown in the two graphs (c) and (d) at bounce where the entropy and luminosity profile, respectively, have again converged with respect to energy resolution. At this stage, we detect an influence of the spatial resolution. During collapse, there is no special region with a high concentration of grid points. At bounce, however, the grid points speed inwards to resolve the newborn shock wave. We detect an effect of this rapid grid displacement in the entropy and electron neutrino luminosity profiles to the extent shown in graphs (c) and (d). Differences in the entropies can also be seen at the interface between the silicon layer and nuclear statistical equilibrium at a radius ~ 1000 km. The difference is of no concern because it stems from the granular triggering of zone conversions from silicon to NSE. Each run determines autonomously when output files are dumped. For a given time, we then compare the output with the closest available output files in other runs. Hence, it can happen that the conversion of a zone took already place in one run, but not in another one. The location of the transition to NSE shows an uncertainty of at least one zone width. The first 10 ms after bounce are probably the most dynamical time in the simulations. At this time we find again the most prominent resolution dependencies in the entropy and luminosity profiles. It is still a dependency on the space resolution alone. The entropy in the high energy resolution run carries the slight enhancement from before, overlapped by a slightly narrower and deeper cooling at the launch of the neutrino burst. The higher luminosity peak in graph (f) at higher spatial resolution comes not unexpectedly, as we have seen in subsection 4.4 that the decay of the outwards propagating neutrino burst depends on the zone width. We can also demonstrate by this resolution study, that the described pulse spreading does only marginally depend on the angular resolution. Note that the apparent difference in the run with higher energy resolution is not a real difference, it stems from an insufficient time match between the output files and shows the rapidly decaying luminosity profile at a slightly earlier time.

Finally, we compare the runs with different resolutions during the important neutrino heating phase, e.g. at 100 ms after bounce. Graphs (g) and (h) show again the entropy and luminosity profiles. We are happy to report that the simulations are converged at this stage. With the exception of the slightly higher entropy in the outer layers of the high space resolution run, none of the previously discussed differences has survived to this time. Moreover, the quality of agreement presented in these graphs is similar to what we find in the velocity, logarithmic density, electron fraction, and rms neutrino energy profiles at any time during the simulations. We conclude that convergence issues are far from affecting our physical conclusions from the simulations. Only if one asks for high precision numbers in specific quantities, we may, with descending importance, recommend an increase of space-, energy-, and angle-resolution.

4.6. Energy conservation

After having put much effort into the consistent finite differencing of the transport equation in favor of an accurate evolution of expectation values, we investigate in this section the energy conservation properties in the most challenging run started from the massive $40 M_\odot$ progenitor star. Our scheme preserves lepton numbers to machine precision by construction. In Fig. (17) we show how the total energy in the simulation divides up into different energy forms during the simulation. The gravitational energy (thin solid line in the lower part of the figure) and the internal energy of the fluid (thin solid line in the upper part of the figure) form the largest contributions. For this figure, we have set the undetermined constant in the internal energy such that the total energy vanishes at the start of the simulation. The energy stored in neutrinos (dash-dotted line) grows with respect to the internal fluid energy until bounce. Afterwards, it evolves almost proportionally to the internal fluid energy. The kinetic energy (thin dashed line) also grows during collapse. It peaks at bounce and settles on a lower level afterwards, slightly decaying during the stationary postbounce phase because of the decreasing density of infalling material. The dotted line at the center of the figure is the work exerted on the surface of the computational domain. The thick dashed line is the accumulated energy emitted by neutrinos. Its steep increase around bounce is delayed with respect to the other energy contributions because of the delay in the neutrino burst and the propagation time to the surface of the computational domain at 10^4 km radius. The thick solid line represents the evolution of the total energy in our simulation. It is very accurately conserved during the core collapse phase. It shows a perturbation of order 5×10^{49} erg in the most dynamic phase around bounce when the grid points rush to the center to resolve the shock front. It systematically increases afterwards and reaches the order of an explosion energy at the end of the simulation when the neutron star collapses to a black hole. We further investigate this energy violation in the next two figures.

We would obtain energy conservation to machine precision if we could enforce perfect cancellation in the six chains discussed after Eq. (37), i.e. $(D_a^4 O_E^1)$, $(D_\mu^{12} O_E^{34})$, $(O_E^2 O_\mu^2)$, $(O_E^{56} O_\mu^{34})$, $(C_t^2 D_\mu^{34} D_E^2)$, and $(C_t^4 D_a^2 D_E^1 O_\mu^1) - 4\pi r^2(1 + e + p/\rho)H$. The hydrodynamics scheme is designed to absorb the energy exchange by the collision integral to machine precision and conserve energy perfectly, even on the adaptive grid. By selecting only the positive contributions in the canceling terms we obtain a measure of the importance for an accurate cancellation. After an integration over the computational domain, Fig. (18) illustrates this measure for the six above-mentioned expressions with a thick dashed line, a thick solid line, a dash-dotted line, a dotted line, a thin dashed line, and a thin solid line, respectively. After bounce, the maximum individual contribution to the energy conservation equation in Eq. (27) reaches a typical level of 5×10^{52} erg/s. Fig. (18) makes immediately evident that maintaining accurate energy conservation is more challenging after bounce than before

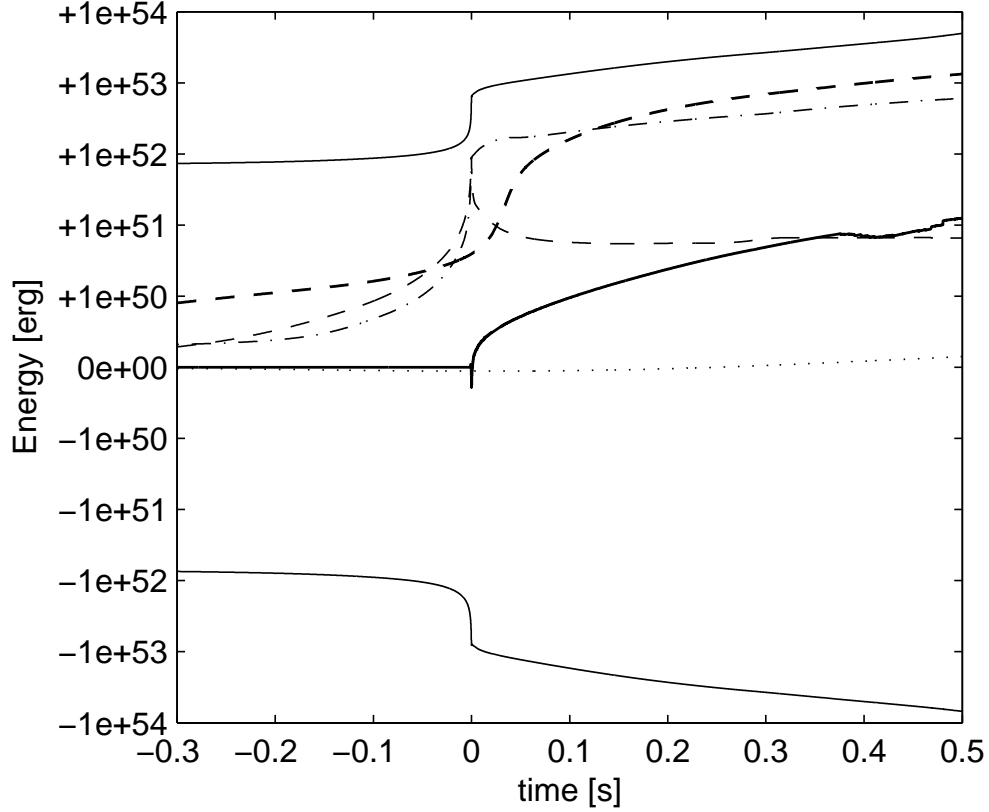


Fig. 17.— The different components of the energy budget are shown. The internal energy of the fluid is represented with a thin solid line in the upper half of the figure. We set the free constant in the internal energy such that we start with zero total energy (thick solid line). Most of the internal energy is balanced by the gravitational energy (thin solid line in the lower half of the figure). We show also the kinetic energy of the fluid (thin dashed line) and the surface work exerted at the border of the computational domain (dotted line). The dash-dotted line represents the energy of the neutrinos in the computational domain and the dashed thick line represents the accumulated energy of the escaped neutrinos. The total energy is nicely conserved during core collapse and exhibits a systematic increase of order 10% of an explosion energy during the crucial phase around 100 ms after bounce.

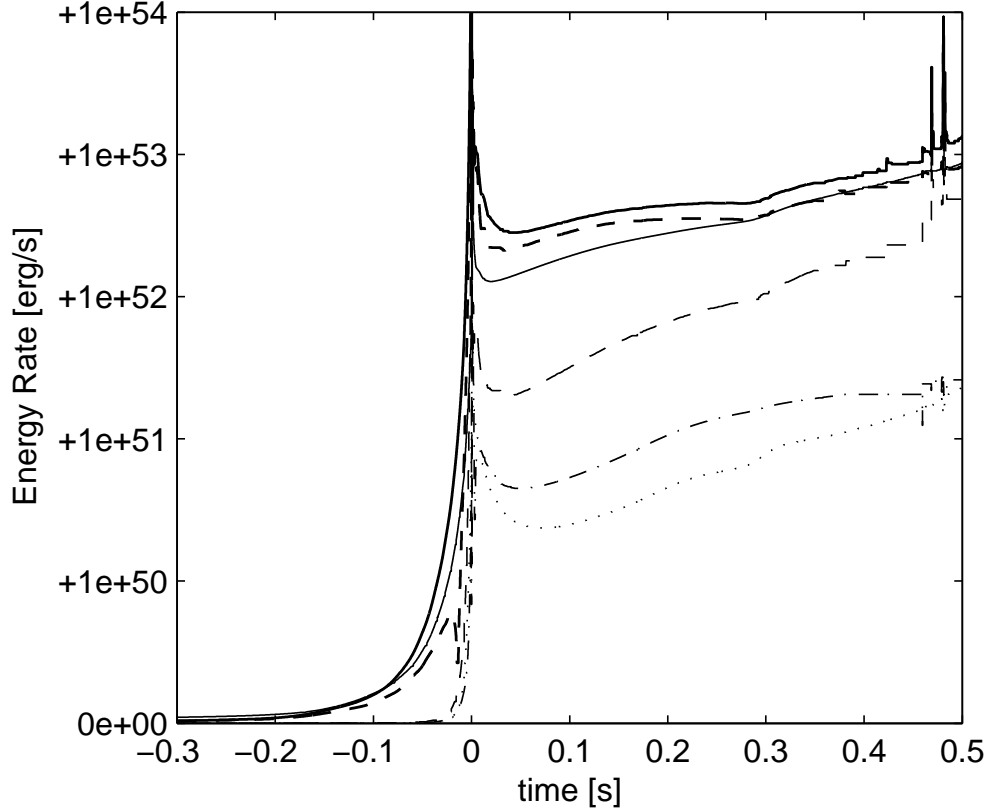


Fig. 18.— For the six chains of terms that are supposed to cancel in Eq. (37) we show the size of all positive contributions to measure the importance of accurate cancellations. The implementation of the $O(v/c)$ cancellations ($D_\mu^{12}O_E^{34}$) and ($D_a^4O_E^1$) are most important (thick solid line and thick dashed line, respectively). Of similar importance is a matching in the general relativistic term ($C_t^4D_a^2D_E^1O_\mu^1$) – $4\pi r(1 + e + p/\rho)H$ (thin solid line). About one order of magnitude less important is the matching ($C_t^2D_\mu^{34}D_E^2$) (thin dashed line). Of lowest importance is the matching among observer corrections themselves in ($O_E^2O_\mu^2$) and ($O_E^{56}O_\mu^{34}$) (dash-dotted and dotted lines, respectively). The figure illustrates the steep increase in the challenge to conserve energy after bounce.

bounce. Moreover, we note that the $O(v/c)$ terms ($D_a^4 O_E^1$) and ($D_\mu^{12} O_E^{34}$) are much larger than the higher order terms ($O_E^2 O_\mu^2$) and ($O_E^{56} O_\mu^{34}$).

Nevertheless, these terms are perfectly matched in our implementation. Violation of energy conservation therefore stems from the terms ($C_t^2 D_\mu^{34} D_E^2$) (the matching is tuned for an isotropic neutrino distribution) and ($C_t^4 D_a^2 D_E^1 O_\mu^1$) – $4\pi r(1 + e + p/\rho)H$ (the matching is based on an energy flux averaging) as discussed in the context of Eqs. (68) and (84) respectively. In section 3.2 we have discussed energy conservation violations by the adaptive grid corrections when they are applied to the radiation quantities. Where do they enter the conservation check? If we evaluate Eq. (27) on the adaptive grid according to the recipe in Eq. (44), we note that the integration of the energy over the whole star reduces the adaptive grid corrections to surface terms. These surface terms vanish because the grid velocity is zero at the center and the surface of the star. If we compare with the more detailed Eq. (37) we find that this time derivative corresponds exactly to the term $C_t^1 + C_t^3$. The energy violations by the adaptive grid show only up in the terms C_t^2 and C_t^4 . If these terms are evaluated with all the grid corrections in the time evolution of Γ , u , J , and H , they will numerically differ from the terms C_t^2 and C_t^4 we have used in Eqs. (69) and (84) for the approximate matching. We check the influence of the adaptive grid corrections by a comparison with a run using a pure Lagrangian grid, where no adaptive grid corrections can compromise energy conservation. However, in order to get enough resolution in the run with the fixed grid, we had to run with 400 spatial zones instead of the 103 we used with the adaptive grid. This run is extremely slow. On the one hand, the solution vector is four times larger. But much more important is that every single zone has to change its value from the preshock conditions to the postshock conditions in the allowed 1%-change steps. This requires an almost 10 times smaller time step than with the adaptive grid, where a zone can follow the shock. In the latter case, the conditions in the zone changes on a much longer time scale determined by the drift between the zone speed and the shock propagation. In order to let a run reach the interesting phase around 100 ms after bounce in reasonable time, we had to reduce the angular resolution to only two angular bins. Both measures, the increase of spatial and time resolution and the decrease of angular resolution can in principle affect energy conservation. Nevertheless, we hope to get the correct impression of the influence of the adaptive grid on the energy conservation. The two terms C_t^2 and C_t^4 of the Lagrangian run are also shown in Fig. (19) (thin lines). We find that the order of magnitude of energy violation in the cancellation ($C_t^2 D_\mu^{34} D_E^2$) does not significantly change on the fixed grid. However, the cancellation in the term ($C_t^4 D_a^2 D_E^1 O_\mu^1$) – $4\pi r(1 + e + p/\rho)H$ is greatly reduced on the fixed grid. This suggests that the adaptive grid corrections of the radiation quantities are the dominant remaining sources of energy violation, about five times larger than the mismatch in ($C_t^2 D_\mu^{34} D_E^2$).

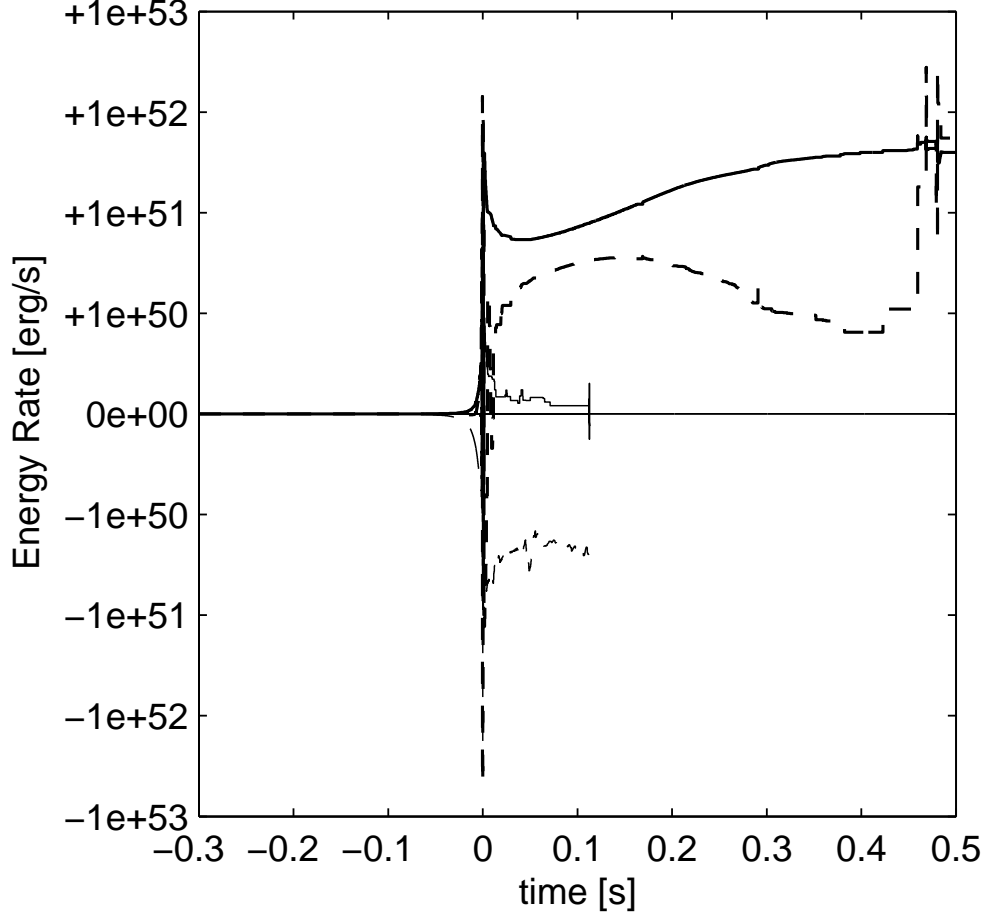


Fig. 19.— The thick solid line and thick dashed line represent the error in the matching of the terms $(C_t^4 D_a^2 D_E^1 O_\mu^1) - 4\pi r(1 + e + p/\rho)H$ and $(C_t^2 D_\mu^{34} D_E^2)$ respectively. All other matches are to machine precision. Therefore, the time integration of these energy rates must reproduce the drift in the total energy represented by a thick solid line in Fig. (17). The two monitored expressions do not allow a distinction of errors induced by approximations in the matching procedure in Eqs. (69) and (84) from errors induced by the application of the adaptive grid to radiation quantities in the comoving frame (see discussion following Eq. (46)). In an attempt to disentangle these two contributions to the violation of energy conservation, we compare the cancellation in the terms $(C_t^4 D_a^2 D_E^1 O_\mu^1) - 4\pi r(1 + e + p/\rho)H$ and $(C_t^2 D_\mu^{34} D_E^2)$ with a Lagrangian run with 400 zones and 2 angular bins (thin solid line and thin dashed line, respectively). The energy violation of the former term is greatly reduced on a fixed grid.

The absolute necessity of accurate energy conservation may be discussed. But certainly, it provided an invaluable check for the congruence between the programmers intention and the actual implementation of the many intricate finite difference expressions in our code.

4.7. Comparison with Multi-Group Flux-Limited Diffusion

Following our tradition (Mezzacappa & Bruenn 1993a), we conclude this paper with a comparison with simulations using the Multi-Group Flux-Limited Diffusion (MGFLD) approximation. We note that, excepting the pioneering Boltzmann solver of (Wilson 1971), codes with MGFLD currently provide the only alternative numerical data for the evolution of a supernova in full general relativity (Myra et al 1987; Schinder & Bludman 1989; Bruenn, DeNisco, & Mezzacappa 2001). We compare the evolution of a $13 M_{\odot}$ progenitor (Nomoto & Hashimoto 1988). This is a stellar model with a small iron core which—in the hope of seeing an explosion in numerical simulations—has been used throughout the supernova literature. Questions concerning the accuracy of the MGFLD approximation in the dynamic semi-transparent region between the neutrino sphere and the heating region have been posed and answered in several studies with different flux limiters (in the supernova context e.g. (Janka 1992; Messer et al. 1998; Yamada, Janka, & Suzuki 1999)). For general relativistic MGFLD simulations (Bruenn, DeNisco, & Mezzacappa 2001) Bruenn developed a new flux limiter that consists of two parts (Bruenn 2002): The first part is a specific implementation of the usual scheme for interpolating between the optically thick diffusion regime and the optically thin free streaming regime, namely

$$\mathcal{F}_{\text{interp}}(E) = \left(1 + \frac{1}{3}\lambda_t(E) \frac{|\partial\psi^0(E)/\partial r|}{\psi^0(E)}\right)^{-1},$$

where $\lambda_t(E)$ is the total energy-dependent transport mean free path. This ensures that

$$\psi^1(E) = -\frac{\lambda_t(E)}{3} \frac{\partial\psi^0(E)}{\partial r}$$

in the diffusion limit, and that $\psi^1(E) = \psi^0(E)$ in the free streaming limit. This part alone suffers from the generic problem of too rapid a transition to the free streaming limit when matter goes from optically thick to optically thin abruptly. To avoid this problem, a second piece of the flux limiter is constructed. It basically prevents the neutrino angular distribution from becoming more forward peaked than the geometrical limit. At radius r , the second part depends on the radius of the neutrinosphere, $R_{\nu}(E)$, and is given by

$$\mathcal{F}_{\text{geom}}(E) = \begin{cases} \frac{\frac{1}{2}(1+\mu_0(E))\psi^0(E)}{\frac{1}{3}\lambda_t(E)|\partial\psi^0(E)/\partial r|} & \text{if } r > R_{\nu}(E) \\ 1 & \text{if } r \leq R_{\nu}(E) \end{cases}$$

where

$$\begin{aligned}\mu_0(E) &= \frac{\mu(E) + v}{1 - \mu(E)v}, \\ \mu(E) &= \sqrt{1 - \left(\frac{R_\nu(E)}{r}\right)^2} \mathcal{G},\end{aligned}$$

and

$$\mathcal{G} = \left(1 - \frac{2m}{r}\right)^{1/2} \left(1 - \frac{2m}{R_\nu(E)}\right)^{-1/2}.$$

The quantity μ is the cosine of the angle from the limb of the neutrinosphere to the point at r , corrected for gravitational bending, and μ_0 is that same angle as seen in the fluid frame. The net diffusivity in the diffusion equation is then set by the minimum of the two parts of the flux limiter,

$$\mathcal{D}(E) = \frac{\lambda_t(E)}{3} \min(\mathcal{F}_{\text{intrp}}(E), \mathcal{F}_{\text{geom}}(E)).$$

In the following, we compare Bruenn’s MGFLD simulation with this flux limiter to the solution we have obtained by the complete solution of the transport equation. Beside of the different methods implemented for the radiation transport, the two codes also use different schemes to solve the hydrodynamics equations. While the code described in this paper adapts to spatial resolution requirements by continuously displacing zones, the MGFLD code adjusts the resolution by occasionally inserting or removing zones. It uses of order 150 zones at bounce and 250 zones half a second after bounce, while AGILE-BOLTZTRAN works with 103 zones throughout. The energy resolution in MGFLD is given by 20 groups which adapt to the general relativistic redshift. In the Boltzmann solver, we used 12 fixed energy groups.

We start with the comparison of a time slice at bounce in Figure (20). The ordinates of graphs (a-h) display the enclosed mass. At the end of core collapse, we find differences in the density profiles in graph (b) of 3% at the center, and less than 1% in the inner core. Differences of up to 80% around the shock front are due to a different resolution of the shock. Outside of the shock, we find a $\sim 30\%$ lower density in AGILE-BOLTZTRAN. The shock position, however, is in reasonable agreement as shown in the velocity profiles in graph (a). This is a consequence of the agreement in the thermodynamical state within the homologous inner core up to the sonic point at an enclosed mass of $\sim 0.54 M_\odot$. Differences in the infall velocities are of order 6%. In the diffusive domain, we find agreement in the entropies of order 5% (graph (c)). Around an enclosed mass of $0.8 M_\odot$, however, the deviations are systematic and of order 10%. At least part of it is due to a narrow choice of the spatial resolution in AGILE-BOLTZTRAN as discussed in section 4.5. Immediately connected to the entropy profile is the temperature profile in graph (f). The temperature is very sensitive to entropy differences in the degenerate high density material. The electron fractions in

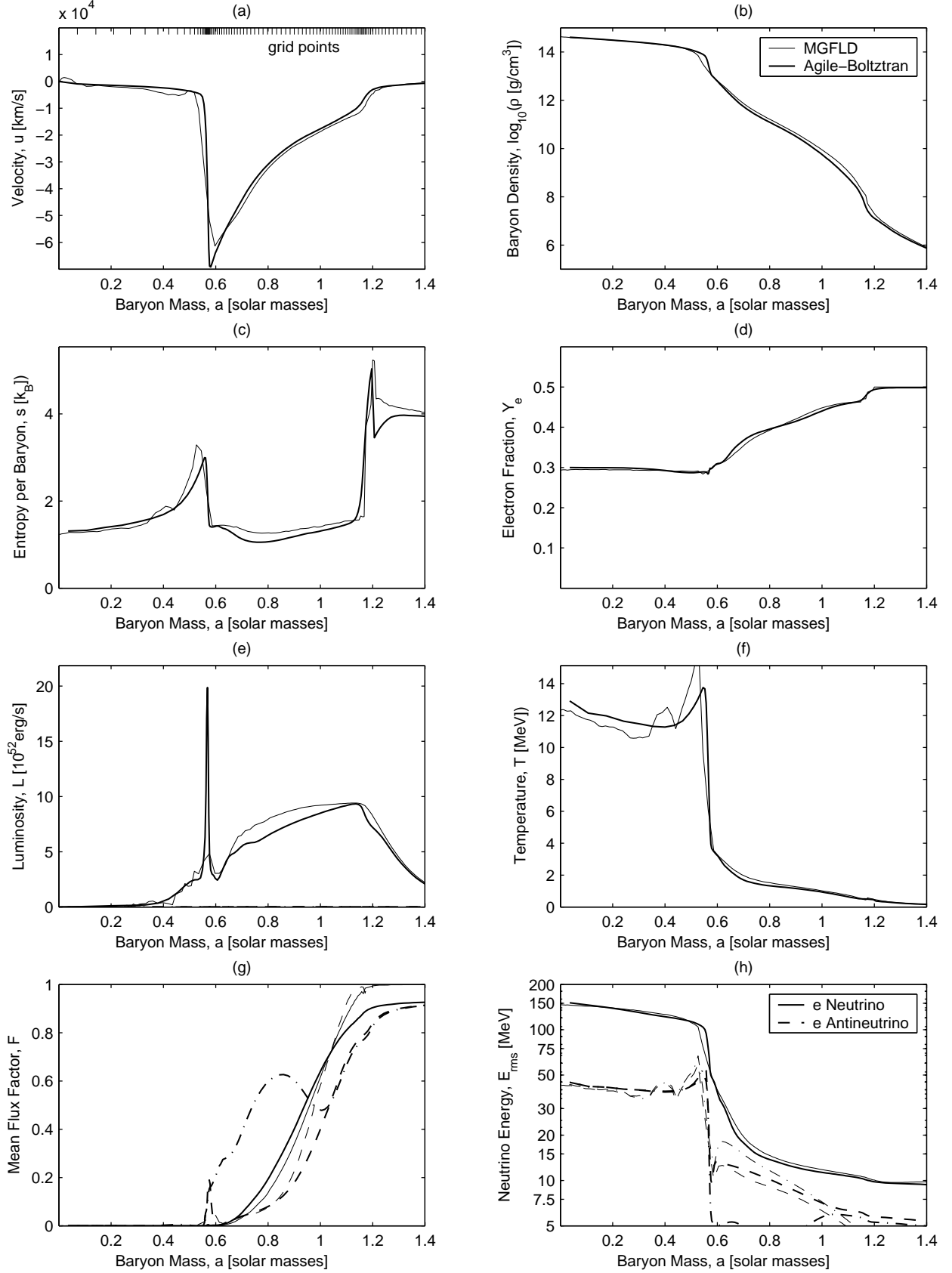


Fig. 20.— Comparison with MGFLD, $13 M_{\odot}$ model at bounce.

graph (d) differ typically by 2%. The maximum deviation of 4% is found where the entropy deviation is largest. At lower densities than $\sim 10^{10}$ g/cm³, the dominant source of neutrinos is provided by electron capture on heavy nuclei. As the mass fraction of heavy nuclei is not very temperature dependent, the entropy difference only affects the deleptonization by the dependence of the electron capture rates. AGILE-BOLTZTRAN finds a slightly lower electron fraction in this regime. At densities exceeding $\sim 10^{10}$ g/cm³, however, standard input physics used to prematurely switch off electron captures on heavy nuclei in the oversimplified independent particle model (Langanke et al. 2003) such that electron captures on free protons became dominant in the simulations compared here. The lower entropy in the simulation with AGILE-BOLTZTRAN leads to a smaller mass fraction of free protons and reduced deleptonization with respect to the MGFLD simulation. The slightly larger electron abundance between 0.65 and 0.8 M_{\odot} is a consequence. The agreement in the luminosities in graph (e) is of order 15%. The solution in the diffusive domain is smoother in AGILE-BOLTZTRAN because the expanding zones of the adaptive grid equilibrate local discontinuities introduced by the equation of state. In contrast to these random fluctuations inside the shock front, we find a systematic deviation of 15% in the luminosities outside of the shock front. This difference might also be a consequence of the lower entropy in AGILE-BOLTZTRAN. The neutrino rms energies (graph (h)) in the inner core are determined by thermal equilibrium. There, the agreement is to 3%. Outside of the shock front, the deviation is initially more around 6%, before it becomes better again towards very large radii. The mean flux factor, the ratio of neutrino flux over neutrino density, $F = H/(cJ)$, in graph (g) shows differences of order 20% at this time. The smaller flux factor of the MGFLD neutrinos at an enclosed mass of about 0.8 M_{\odot} is probably due to increased isotropic neutrino emission at the higher entropy. It leads to slightly higher luminosities and higher rms energies, and is consistent with the smaller electron fraction. We should note here that it is very typical for such comparisons that each code presents an itself consistent picture of the dynamics such that it is sometimes almost impossible to isolate a single cause for a difference in the strongly coupled variables. The smaller flux factor in AGILE-BOLTZTRAN outside 1.1 M_{\odot} stems from the limited angular resolution discussed in section (4.2). It is systematic and visible in all the following figures. Its impact on the dynamics, however, is negligible because of the small coupling between the neutrino flux and matter at large radii.

Figure (21) shows a time slice just after the launch of the neutrino burst. This is the most dynamical phase for the radiation transport. The neutrino burst in graph (e) is evident in both codes as a propagating peak in the luminosity profile. The peak at ~ 2000 km radius is broader and by 25% smaller in AGILE-BOLTZTRAN because of the numerical diffusion we have analyzed in section 4.4. The MGFLD burst changes its shape more slowly because the MGFLD code reverts, in the transparent regime, to centered difference advection (rather than

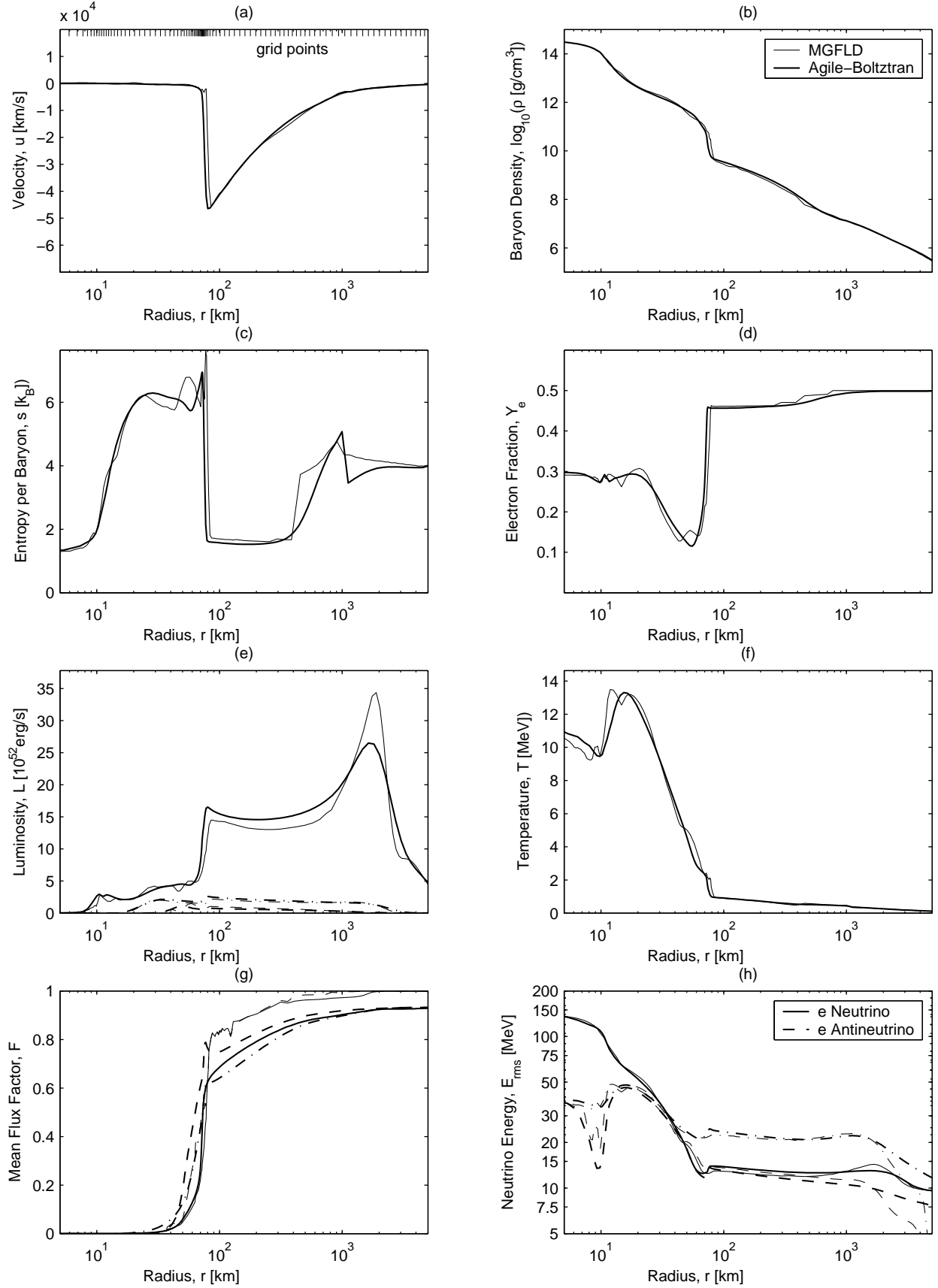


Fig. 21.— Comparison with MGFLD, $13 M_{\odot}$ model, 10 ms after bounce.

first order upwind) which is second order accurate in space (on a uniform spatial grid). The luminosity in the region between the shock and the luminosity peak decays very rapidly. Differences of order 15% are due to a small time mismatch between the two solutions. Inside the shock front, the luminosity is still much noisier in the MGFLD solution. This is also true for the entropy profile in graph (c), where local differences of 20% behind the shock or 50% at 400 km radius, disturb the otherwise nice agreement of order 5%. Note however, that the temperature profiles in graph (f) is less sensitive to this entropy variation. The temperature difference at 400 km radius is 12%. The agreement in the infall velocities in graph (a) has improved to generally 2% agreement with the exception of 9% around 400 km radius, i.e. the region with the entropy differences. The entropy deviations inside the shock front and at 400 km radius cause density differences of 25% in these regions. The central density agrees to 1% and the agreement in the very distant layers is of order 3%. The electron fraction profile is affected by the numerical noise as well. Deviations, however, are only of order 2%, with local exceptions showing differences of 10%. the rms energies in graph (h) typically agree to 5%. The differences in the flux factors in graph (g) show systematic deviations of 10% outside of 100 km radius and random fluctuations of order 20% interior to it. The latter are probably a consequence of the variations in the density and entropy profiles.

Most important for the success or failure of the supernova explosion in our spherically symmetric simulations is the time ~ 100 ms after bounce. Though, we have to state clearly that the general relativistic runs are not failing marginally. They are failing with officious insistence, and differences of the size we have described above are far from changing this, as we will show with the next two time slices. Figure (22) shows the comparison of the two simulations at 100 ms after bounce, when the efficiency of the neutrino heating is close to maximum. The agreement of the data in this phase is remarkable. In this quasi-stationary phase, the position of the stalled shock is in accurate agreement as one can see in graph (a). We note however, that the important infall velocity in the heating region (e.g. at 100 km radius) is 10% larger in MGFLD than in AGILE-BOLTZTRAN. Since this infall velocity determines the time the infalling matter spends in the heating region before being accreted onto the protoneutron star, its value is as relevant as the heating rate. Better visible in the graph are the differences in the infall velocity which have only a size of 3%. Again, they reflect differences in the entropy profile in graph (c). Outside the shock the entropy deviations of order 20% seem large. However, they correspond to temperature variations of only 10% and are explicable by the assumption of instantaneous silicon burning in AGILE-BOLTZTRAN. MGFLD uses a 9 species nuclear network to burn nuclei to iron until the temperature exceeds 5.106×10^9 K, at which point the zone is flashed to NSE. Inside the shock front, the agreement in the entropies is good to 2% (except for some local fluctuations in the MGFLD solution in the heating region). As the rise in entropy between the shock front and the location at

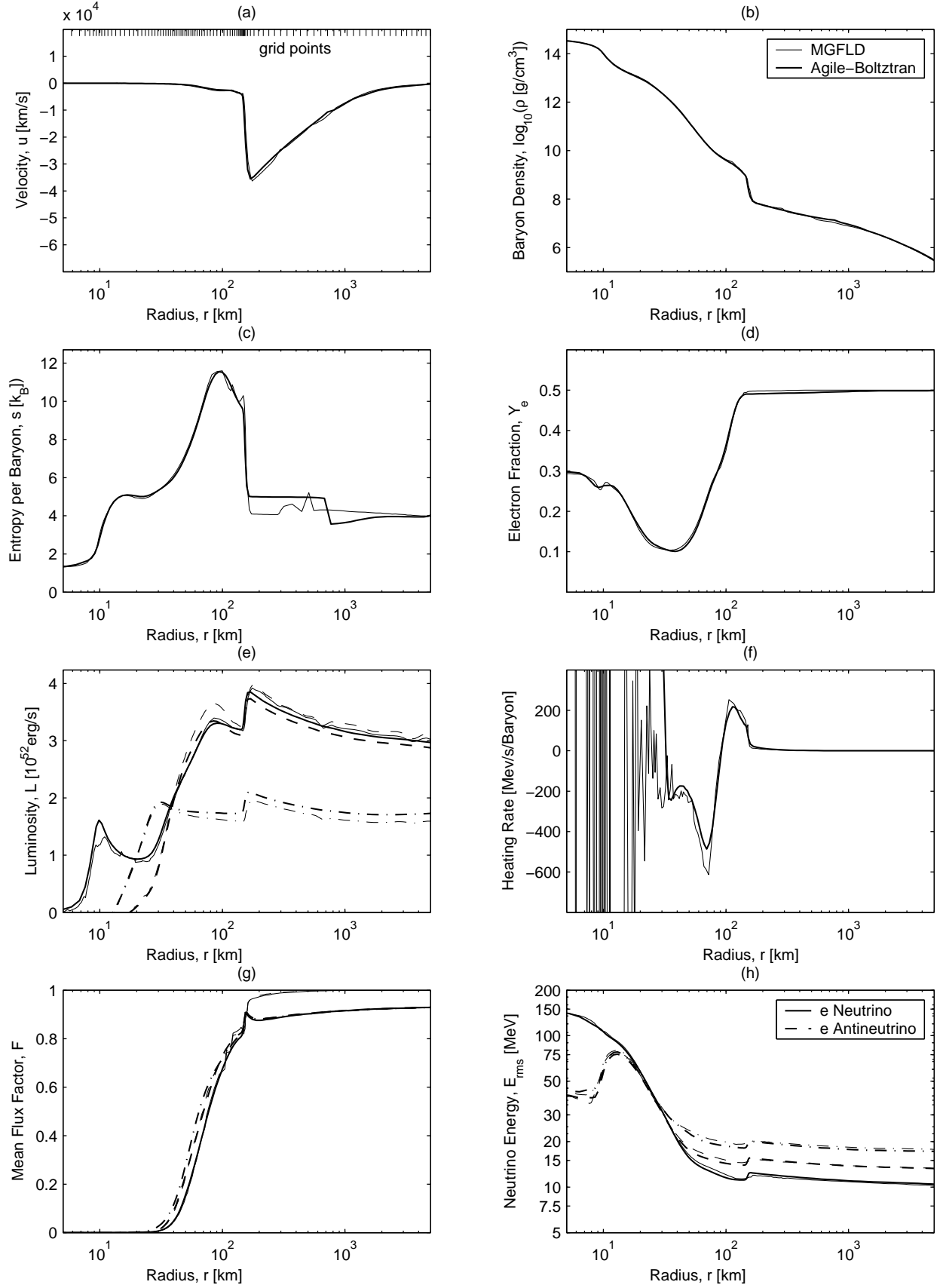


Fig. 22.— Comparison with MGFLD, $13 M_{\odot}$ model, 100 ms after bounce.

100 km radius is entirely due to neutrino heating, this is an encouraging result. In this time slice, we have replaced the temperature graph (f) with a graph of the more important heating rates. Plotted is the sum of the heating rates by electron neutrino absorption and electron antineutrino absorption. The rate is negative in the cooling region, representing cooling rates by the inverse processes, electron capture and positron capture. We find 7% difference in the heating region and 10% difference in the cooling region. The values in the MGFLD simulation are larger. This is perfectly consistent with the larger electron antineutrino luminosity in graph (e) and the larger infall velocity behind the shock in graph (a). The electron fraction profiles in graph (d) agree to 2% accuracy with the exception of two local 6% deviations at 25 km and 45 km radius, where the electron fraction is as small as ~ 0.1 . This close agreement in the entropy and electron fraction leads to a similar thermodynamical state of the fluid in the inner core. Good agreement in the nearly hydrostatic density profile in graph (b) is the consequence. Differences are 0.5% at the center and on average around 5% up to a radius of 400 km. Further out, differences stemming from the silicon/iron layer interface are visible. The good agreement in the density profiles facilitates the comparison of other density-dependent quantities. E.g. the neutrino rms energies in graph (h) agree to 2% in the innermost core, to 6% in the heating regions, and to 3% outside of the shock front in the neutrino signal. In the heating region, the rms energies are lower in AGILE-BOLTZTRAN. At larger radii, the electron neutrino energies are lower in MGFLD, while the μ - and τ -neutrino energies are lower in AGILE-BOLTZTRAN. The electron antineutrino energies do not show a discernible tendency. The electron neutrino luminosities in graph (e) are 5% larger in AGILE-BOLTZTRAN in the diffusive domain and 2% larger in MGFLD in the heating region. The electron antineutrino luminosity is about 6% larger in AGILE-BOLTZTRAN in both domains. In the μ - and τ -neutrino luminosities, deviations start at 20 km radius with 2% and linearly increase to 10% at the shock position. With respect to the neutrino signal, the electron flavor luminosities are larger in the simulation with MGFLD and the μ - and τ -luminosities are larger in the simulation with AGILE-BOLTZTRAN. This is just inverse to the relation between the rms energies. While, for example, an increase in the rms energy contributes only linearly towards a luminosity increase, the neutrino flux, however, is determined by the quadratically decreasing mean free path. Where the flux factors in graph (g) are below 0.5, they are typically 5% lower in MGFLD. Between this domain and the shock front (including the heating region) the flux factors show on average no discernible deviation, but fluctuations of $\pm 5\%$ are evident. The flux factors in AGILE-BOLTZTRAN disagree with the asymptotic limit, $F = 1$, by 8% at distant radii due to the limitation in angular resolution as discussed in subsections 4.2 and 4.5.

Similar agreements and differences are found in later stages of the quasistationary phase, e.g. at 400 ms after bounce (Fig. (23)). We find again hotter neutrinos between the neutrino

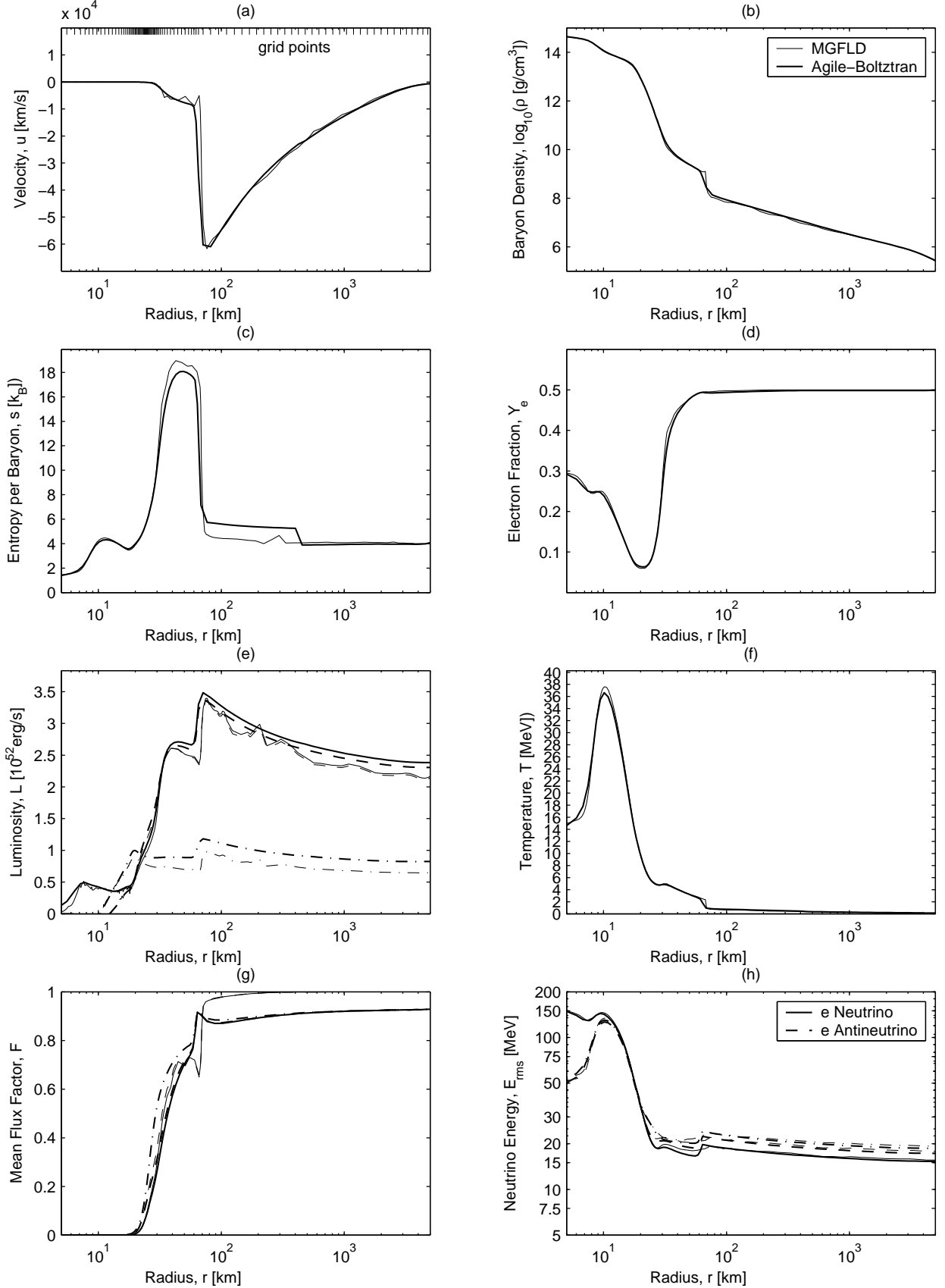


Fig. 23.— Comparison with MGFLD, 13 M_{\odot} model, 400 ms after bounce.

sphere and the shock position in the MGFLD simulation and a larger diffusive flux at very high densities in AGILE-BOLTZTRAN. On a longer time scale, the latter leads to a marginally larger deleptonization, visible in the innermost 7 km of the electron fraction profile. The electron fraction in AGILE-BOLTZTRAN is now 2% smaller, whereas it was 2% larger early after bounce. A new difference of 6% appears in the peak of the entropy profile, which might be due to differences in the hydrodynamics scheme for the solution of the shock jump conditions. We also point to the fact that the resolution of the shock in this stage is quite poor. The thin marks at the top of graph (a) represent the grid point locations in the AGILE-BOLTZTRAN simulation. Most of the grid points cluster around the forming density cliff between 20 km and 30 km radius. A high resolution in this domain is important for the radiation transport because most neutrinos are emitted from the cliff. However, this leaves less grid points to focus on the shock front. Graph (a) shows only a small increase of the grid point concentration at the shock front. The infall velocities inside the shock in graph (a) have increased to 10^4 km/s. At this speed, the infalling material is only very shortly exposed to neutrino heating. This is consistent with the observation that the entropy increase from the shock to the peak entropy is only marginal in both runs. Without unaccounted effects, a shock revival is impossible under these conditions. The most significant new differences appear in the luminosity and rms energy profiles. MGFLD has now consistently smaller luminosities and higher rms energies. The differences are 20% in the luminosities and unchanged 6% in the rms energies in the heating region. Also interesting to note is that the rms energies agree perfectly right outside the shock at 100 km radius, and develop deviations of 3% – 4% at far distances. There might be small differences in the implementation of the observer corrections. The flux factors in graph (g) are more difficult to compare, because the neutrinos no longer decouple at exactly the same radius. The flux factor in AGILE-BOLTZTRAN is still numerically limited in its asymptote, while the flux factor in MGFLD exhibits somewhat peculiar fluctuations in the heating region.

Overall, in our general relativistic simulations of stellar core collapse and postbounce evolution in spherically symmetric space-time, we find quite exactly the same physical evolution in both runs. One implementing the full Boltzmann transport equation, and the other based on the multi-group flux-limited diffusion approximation with a new sophisticated flux limiter. This is especially true in all phases of stationary radiation transport. There are modest quantitative differences in these simulations of failed supernovae. However, except for some obvious cases, like e.g. the limited asymptotic flux factor in AGILE-BOLTZTRAN, or the numerical fluctuations that the equation of state induces to purely Lagrangian hydrodynamics in MGFLD, these quantitative differences cannot uniquely be traced back to principal weaknesses or strengths of either method. They may rather be due to method-specific details in the implementation of two very different methods to solve a complex time-dependent

physical problem. The advantage of the Boltzmann solution is that it is complete, and, beside of numerical resolution, does not need to justify or verify any basic assumptions. The advantage of MGFLD is the transparency of the approach, and that it produces accurate results with much higher efficiency in the application we have tested here.

5. Conclusion

AGILE-BOLTZTRAN directly solves the general relativistic Boltzmann transport equation for the specific neutrino distribution function in spherically symmetric space-time. In combination with general relativistic hydrodynamics, we present a consistent finite differencing for fermion radiation hydrodynamics in spherical symmetry. We test our code in the context of stellar core collapse and postbounce evolution of a smaller $13 M_{\odot}$, and a more massive $40 M_{\odot}$ progenitor star. They embrace the progenitor mass range expected to produce explosions after core collapse. But no explosions are obtained in our simulations. We analyze the regions of neutrino emission by a statistical description allowing the detailed presentation of the specific production reactions and energies of escaping neutrinos.

The Boltzmann transport equation plays a fundamental role in kinetic gas theory. One may derive from it the diffusion equation, or—if one drives the limit further to vanishing transport—the hydrodynamics equations. Thermodynamical quantities are given by the expectation values of various operators on the fundamental particle distribution functions. It is quite unique to numerically solve a single equation for the fundamental particle distribution functions in an object of astronomical size! However, this basic approach becomes intricate in the detailed finite difference representation. In theory, the solution of the Boltzmann equation guarantees the correct evolution of expectation values in the energy conservation equation or the diffusion limit. Also the equation of state for radiation, $p \propto \rho/3$, will emerge correctly. This is not automatically the case in a numerically solved Boltzmann equation. Especially in the astrophysical application, a distant observer will rather observe macroscopic phenomena than the microscopic local state of the matter and the radiation field. Therefore we compose the finite difference representation of the microscopic physics such that important macroscopic quantities are accurately met. This optimizes the accuracy of the simulations at moderate resolution settings. However, it would be more straightforward to comply with this ambition if there would not be an additional complication. Physically, the Boltzmann transport equation is a trivial equation, describing free particle propagation on geodesics between independent collisions (even more so in spherical symmetry, where only two independent spatial degrees of freedom have to be considered). With respect to the collisions, the supernova has been investigated as a site of interesting nuclear physics and

neutrino-matter interactions. The cross sections depend on the local neutrino energies and scattering angles. They are most conveniently evaluated in the fluid rest frame and most easily described in combination with comoving coordinates. The latter are also favored by the initial core collapse where the relevant computational domain collapses with the matter from several thousands to some hundreds of kilometer radius, before it hopefully expands again with the explosion. The comoving coordinates convert the simple statement of the Boltzmann equation, that the derivative of the invariant particle distribution function along the phase flow vanishes between collisions, into a complicated sum of partial derivatives along the comoving coordinates. The finite differencing of all comoving frame correction terms have to be adjusted in a mutually dependent way to correctly transform to conservation equations for the observer in a laboratory frame. We construct number conservation to be guaranteed. With respect to energy conservation, we match the largest $O(v/c)$ terms to machine precision, while higher order gravitational terms are matched approximately, guided by specific limiting cases. The adaptive grid applied to the neutrino distribution function in the comoving frame introduces additional deviations from perfect energy conservation in the laboratory frame. In the worst case, i.e. in the evolution of the very massive $40 M_{\odot}$ progenitor star, all these deviations together reach the order of a supernova explosion energy ($\sim 10^{51}$ erg) at the time the protoneutron star collapses to a black hole. However, when the conditions are most favorable for an explosion (we should rather say least unfavorable), the numerical energy gain has not yet exceeded 10^{50} erg and we are confident that the remaining energy drift does not influence our physical conclusions. We have also tested the implementation of the gravitational redshift and bending, the angular advection in the free streaming regime, and the propagation of the neutrino burst. Quite generally, we find that the choice of first order upwind differencing is the limiting factor for the accuracy in our numerical solution. In space, it causes artificial pulse spreading. In the advection terms of the adaptive grid, it causes artificial diffusion. In momentum space, it causes angular diffusion in the evolution of the particle distribution function. Although these limitations can be reduced by the choice of higher resolution, more elaborate advection schemes could generally be beneficial for the accuracy of the simulations. With an investigation of the resolution dependence of the results in each phase space dimension, however, we demonstrate that our physical results are sufficiently converged in the supernova application. The undesired effects of low order upwind differencing predominantly affect the regions far from the neutrinospheres, where the radiation field is decoupled from the matter such that an adverse influence on the dynamics of the model can be excluded. We derived the moments entering the energy conservation equation. Moreover, we algebraically derived the finite difference representation of the diffusive limit, the nonrelativistic limit, and the radial dependence of the radiation quantities in a stationary state free streaming radiation field. These algebraic gymnastics led to a better understanding of the internal mechanisms in our finite difference representation

and, by comparison with the code results, enhanced the confidence that the implementation exactly corresponds to the programmer’s intention. In order to perform simulations over a second or more, the radiation transport and hydrodynamics have been implemented with implicit finite differencing. This allows reasonably sized time steps during the neutrino heating phase. Finally we compared the evolution of a 13 M_\odot star with an independently implemented general relativistic supernova code which applies the multi-group flux-limited diffusion approximation with a recently developed flux limiter (Bruenn 2002). We find significant agreement that is especially impressive in the neutrino heating phase. Other phases show regions with moderate deviations, but those are far from affecting any physical conclusions.

With the exponentially growing power of computer hardware, computational astrophysics may reach a comparable status in astronomical, nuclear and particle physics research as terrestrial experiments have received in the previous century. We may sort scientific progress into three phases: First, the astronomical observation or a new theoretical concept lead to a primary idea about the basic physics involved in an event. At this stage, order of magnitude estimates are made and compared to the qualitative observational data. The second step involves plausibility studies of the suggested scenario, which may include detailed numerical simulations and comparisons to observations. Often, however, approximations have to be used that are dictated by technical limitations in the newly developing field. Only in the simplest cases it can be shown that all assumptions are based on undeniably justifiable physical considerations. This exciting phase of discovery and controversy should be followed by more rigorous numerical simulations in a third step, when technical limitations fade and remaining approximations become quantifiable. This phase has to be accompanied by code documentation that allows independent researchers to analyze and eventually reproduce the numerical results, similar to the way the value of experimental data is enhanced by a detailed description of the reproduceable experiment. The recent emergence of functional Boltzmann solvers leads the radiation hydrodynamics in spherically symmetric supernova models into this third phase. The third phase, by principle, should be accompanied by solid agreement in the numerical solution found with independent implementations of the same physical ingredients. In order to perform such comparisons, we appreciate the situation that a basic set of standard nuclear and weak interaction physics has been defined and used for over 15 years (e.g. (Tubbs & Schramm 1975; Schinder & Shapiro 1982; Bruenn 1985)). In a comparison with the second phase—which used the former standard scheme for neutrino transport in supernovae—multi-group flux-limited diffusion, we hope to increase the confidence in our results. On the other hand, we support the validity of the MGFLD approximation in spherical symmetry if the flux limiter is chosen carefully. As satisfying as these close results are, they should not be mistaken as an example

of convergence to agreement in the sense of the third phase. The third phase is only reached if similar agreement is found between independent groups and other documented codes that solve physically complete neutrino transport equations with general relativistic effects, e.g. the variable Eddington factor method implemented by Rampp & Janka (2002). We hope that spherically symmetric simulations with neutrino radiation hydrodynamics have reached phase three and that accurate and detailed neutrino information continues to be useful for the exploration and improvement of the local microscopic input physics.

Acknowledgment

We thank Raph Hix for fruitful discussions and comments on the manuscript. We enjoyed discussions with Markus Rampp, Thomas Janka, Gabriel Martinez-Pinedo, and Karlheinz Langanke. We acknowledge support from the National Science Foundation under contract AST-9877130, the Oak Ridge National Laboratory, managed by UT-Batelle, LLC, for the U.S. Department of Energy under contract DE-AC05-00OR22725, the Swiss National Science Foundation under contract 20-61822.00, the NSF under contract 96-18423, the NASA under contract NAG5-3903, the Joint Institute for Heavy Ion Research, a DoE PECASE Grant, and the DoE HENP Scientific Discovery through Advanced Computing Program. Our regular simulations were carried out on the National Energy Research Supercomputer Center Cray SV-1, the high resolution runs and auxiliary checks on the CITA Intel Itanium I.

A. $O(v/c)$ limit of the finite difference representation

The $O(v/c)$ Boltzmann equation has been derived by Castor (Castor 1972). One can also obtain it by the elimination of higher order terms from Eq. (15). It is enough to set $\alpha = \Gamma = \text{const.} = 1$ and to replace u by the nonrelativistic velocity v . The conservation properties of the $O(v/c)$ Boltzmann equation become apparent when we take its energy and angular moments (Mihalas & Mihalas 1984):

$$\begin{aligned} \frac{\partial J}{\partial t} + \frac{\partial}{\partial a} [4\pi r^2 \rho H] + \frac{v}{r} (J - K) - \left(\frac{\partial \ln \rho}{\partial t} + \frac{2v}{r} \right) K \\ - \int \frac{j}{\rho} E^3 dE d\mu + \int \chi F E^3 dE d\mu = 0, \\ \frac{\partial H}{\partial t} + \frac{\partial}{\partial a} [4\pi r^2 \rho K] - \frac{1}{r} (J - K) - \left(\frac{\partial \ln \rho}{\partial t} + \frac{2v}{r} \right) H \end{aligned}$$

$$+ \int \chi F E^3 dE d\mu = 0. \quad (\text{A1})$$

As we construct the specific radiation energy in the laboratory frame, $J + vH$, we keep *all* terms that arise from the $O(v/c)$ Boltzmann equation and obtain, in analogy to Eq. (27), an almost conservative evolution equation for the radiation moments,

$$\begin{aligned} 0 &= \frac{\partial}{\partial t} (J + vH) + \frac{\partial}{\partial a} [4\pi r^2 \rho (vK + H)] \\ &- \int \frac{j}{\rho} E^3 dE d\mu + \int \chi F E^3 dE d\mu + v \int \chi F E^3 dE d\mu \\ &- \frac{1}{4\pi r^2 \rho} \frac{\partial}{\partial t} (4\pi r^2 \rho v) H. \end{aligned} \quad (\text{A2})$$

Although terms of higher order than (v/c) , especially the gravitational terms, require consideration in realistic supernova simulations, the $O(v/c)$ limit may be useful for various explorative studies. We give below a finite difference representation of the $O(v/c)$ Boltzmann equation by simply substituting $\alpha = \Gamma = 1$ in the corresponding general relativistic expressions:

$$C_t = \frac{F_{i',j',k'} - \overline{F}_{i',j',k'} \frac{da_{i'}}{da_{i'}}}{dt} + \frac{1}{da_{i'}} [u_{i+1}^{\text{rel}} F_{i+1,j',k'}^* - u_i^{\text{rel}} F_{i,j',k'}^*] \quad (\text{A3})$$

$$D_a = \frac{\mu_{j'}}{da_{i'}} [4\pi r_{i+1}^2 \rho_{i+1} F_{i+1,j',k'} - 4\pi r_i^2 \rho_i F_{i,j',k'}] \quad (\text{A4})$$

$$D_\mu = \frac{3[r_{i+1}^2 - r_i^2]}{2[r_{i+1}^3 - r_i^3]} \frac{1}{w_{j'}} (\zeta_{j+1} F_{i',j+1,k'} - \zeta_j F_{i',j,k'}) \quad (\text{A5})$$

$$\begin{aligned} O_E &= \frac{1}{E_{k'}^2 dE_{k'}} \left[(\mu_{j'}^2 A_{i',k'-dk} - B_{i',j'}) \frac{dE_{k'-dk}}{E_{k'} - E_{k'-dk}} E_{k'-dk}^3 F_{i',j',k'-dk} \right. \\ &- \left. (\mu_{j'}^2 A_{i',k'} - B_{i',j'}) \frac{dE_{k'}}{E_{k'+dk} - E_{k'}} E_{k'}^3 F_{i',j',k'} \right] \end{aligned} \quad (\text{A6})$$

$$\begin{aligned} O_\mu &= \frac{1}{w_{j'}} \left[(A_{i',k'} + B_{i',j'-dj}/\zeta_{j'-dj}) \frac{w_{j'-dj}}{\mu_{j'} - \mu_{j'-dj}} \zeta_{j'-dj} \mu_{j'-dj} F_{i',j'-dj,k'} \right. \\ &- \left. (A_{i',k'} + B_{i',j'}/\zeta_{j'}) \frac{w_{j'}}{\mu_{j'+dj} - \mu_{j'}} \zeta_{j'} \mu_{j'} F_{i',j',k'} \right] \end{aligned} \quad (\text{A7})$$

$$C_c = \frac{j_{i',k'}(\rho_{i'}, T_{i'}^*, Y_{e,i'}^*)}{\rho_{i'}} - \chi_{i',k'}(\rho_{i'}, T_{i'}^*, Y_{e,i'}^*) F_{i',j',k'}. \quad (\text{A8})$$

The expressions basically reduce to the finite difference representation described in (Mezzacappa & Bruenn 1993a), except for the adaptive grid extension, the new code flow outlined in section 3.5, the improved choice of transport coefficients $\beta_{i,k'}$ and $\gamma_{i',k'}$ in Eq. (56), the

new discretization of angular aberration, and the matched finite difference representation of $A_{i',k'}$ and $B_{i',j',k'}$,

$$A_{i',k'} = \frac{4\pi\rho_{i'}}{da_{i'}} (r_{i+1}^2 (v_{i+2} - v_{i+1}) \beta_{i+1,k'} + r_i^2 (v_{i+1} - v_i) (1 - \beta_{i,k'})) \quad (\text{A9})$$

$$B_{i',j',k'} = \frac{3}{2} \frac{r_{i+1}^2 - r_i^2}{r_{i+1}^3 - r_i^3} \frac{v_{i+1}}{w_{j'}} [\gamma_{i',k'} \zeta_{j+1} (\mu_{j'+1} - \mu_{j'}) + (1 - \gamma_{i',k'}) \zeta_j (\mu_{j'} - \mu_{j'-1})] . \quad (\text{A10})$$

The angular difference coefficients, ζ_j , are defined in Eq. (63).

B. Attenuation factors for the presentation of interaction rates

Whenever one composes a graph for the discussion of weak interaction rates in the supernova environment, one has to circumvent the inherently large scale differences of the rates at different locations in the star. In a logarithmic presentation, many details are hidden and differences between absorption and emission are difficult to appreciate. One can focus on the neutrinospheres and investigate the rates of interest under the corresponding conditions. However, the definition of the neutrinosphere is only based on the opacity and does not account for large emissivities outside the neutrino sphere. One may miss important sources of the total neutrino luminosity and fail in the explanation of the spectra. Moreover, it is common to average the extremely energy-dependent location where a given optical depth is reached to one single neutrinosphere—an even more problematic concept. In this appendix, we motivate a convenient presentation of interaction rates according to their relevance to the total luminosities. The approach aims to produce intuitively accessible figures with information about where the neutrinos come from, which reactions contribute to the total luminosity, how they locally compare to other reactions, and how the neutrino spectra are formed.

We derive auxiliary attenuation factors in terms of a staggered grid with zone edge indices i and zone center indices $i' = i + 1/2$. We start with a conserved luminosity L_i with respect to spheres around the symmetry center. We may choose the neutrino number luminosity in units of particles per second or the neutrino energy luminosity in ergs per second. Each zone may have a number or energy source, $em_{i'}$, and a number or energy sink, $ab_{i'}$, in number or ergs per gram and second. The luminosity is then recursively defined by its central value $L_0 = 0$ and

$$L_{i+1} = L_i + (em_{i'} - ab_{i'}) da_{i'}, \quad (\text{B1})$$

where $da_{i'}$ denotes the rest mass contained in the mass shell i' . The entering luminosity, L_i , and the source, $em_{i'} da_{i'}$, are subject to absorption in this shell. We define an attenuation

factor, $x_{i'} \leq 1$, which accounts for the reduction of these quantities,

$$L_{i+1} = x_{i'} (L_i + em_{i'} da_{i'}). \quad (\text{B2})$$

From Eq. (B1) and (B2), we can readily isolate $x_{i'}$:

$$x_{i'} = \frac{L_{i+1}}{L_i + em_{i'} da_{i'}} = \frac{L_{i+1}}{L_{i+1} + ab_{i'} da_{i'}}.$$

In the rare cases of a negative $x_{i'}$, we set $x_{i'}$ to zero. If we calculate a mean free path, $\lambda_{i'}$, from all reactions that may act as a sink, the absorption rate can also be derived from the local specific number or energy density, $J_{i'}$, according to $ab_{i'} = cJ_{i'}/\lambda_{i'}$. The attenuation factor $x_{i'}$ can then be expressed by physical quantities that are well accessible in a numerical evolution of radiation hydrodynamics,

$$x_{i'} = \frac{L_{i+1}}{L_{i+1} + \frac{cJ_{i'}}{\lambda_{i'}} da_{i'}}. \quad (\text{B3})$$

On the other hand, we derive from Eq. (B2) by two recursive self-substitutions,

$$L_{i+1} = x_{i'} (x_{i'-1} (x_{i'-2} (L_{i-2} + em_{i'-2} da_{i'-2}) + em_{i'-1} da_{i'-1}) + em_{i'} da_{i'}).$$

The continuation to $L_0 = 0$ and a rearrangement of the terms leads to

$$L_{n+1} = \sum_{i=1}^n \left(\prod_{l=i}^n x_{l'} \right) em_{i'} da_{i'}. \quad (\text{B4})$$

This equation describes how the total number or energy luminosity at a radius r_{n+1} is composed by contributions of distributed emissivities in the star. The attenuation coefficients

$$\xi_{n+1,i'} = \prod_{l=i}^n x_{l'} = \prod_{l=i}^n \frac{L_{l+1}}{L_{l+1} + \frac{cJ_{l'}}{\lambda_{l'}} da_{l'}} \quad (\text{B5})$$

suppress irrelevant sources that are subject to large reabsorption. It is instructive to go a step further. We introduce the flux factor $h_{i'} = L_{i+1}/(4\pi r^2 c \rho J_{i'})$ and rewrite Eq. (B5) as

$$\xi_{n+1,i'} = \left(1 + \frac{dr_{i'}}{h_{i'} \lambda_{i'}} \right)^{-1} \xi_{n+1,i'+1}$$

in order to extract the logarithmic derivative of ξ ,

$$\frac{\xi_{n+1,i'+1} - \xi_{n+1,i'}}{\xi_{n+1,i'}} = \frac{dr_{i'}}{h_{i'} \lambda_{i'}}.$$

This is a finite difference representation of the equation

$$\frac{d \ln \xi}{dr} = \frac{1}{h\lambda}$$

with the solution $\xi = \exp(-\int (h\lambda)^{-1} dr)$. It is the familiar attenuation $\exp(-\tau)$, if the radius-dependent flux factors are properly accounted for in the evaluation of the optical depth, $\tau = \int (h\lambda)^{-1} dr$. However, we evaluate the attenuation coefficients according to Eq. (B5) where the finite differencing is consistent with the conservation laws in our implementation of the Boltzmann equation. As a consistency check, we compare in Fig. (24) the original luminosities L_{n+1} from the simulation with the luminosities reconstructed according to Eq. (B4).

We can use the attenuation coefficients in many convenient ways. A graph showing

$$g_{n+1}(r_{i'}) = \xi_{n+1,i'} em_{i'} \frac{da_{i'}}{dr_{i'}}$$

as a function of radius, $r_{i'}$, visualizes the contribution of each region in the star towards the total luminosity (represented by the area under the graph) at radius r_{n+1} . In a comparison of different neutrino species, the graphs illustrate the decoupling at different radii. If the gravitational well is not too deep, the neutrino energy is approximately a constant of motion and the neutrino in different energy groups can be treated like different species. Moreover, instead of considering total emissivities and opacities, one can disentangle them into different reactions which we will enumerate with a superscript ℓ . A figure with graphs showing

$$g_{n+1}^{\ell}(r_{i'}) = \xi_{n+1,i'} em_{i'}^{\ell} \frac{da_{i'}}{dr_{i'}} \quad (\text{B6})$$

as a function of radius $r_{i'}$ would visualize the contribution of reaction ℓ to the total luminosity at radius r_{n+1} by the enclosed area under the line g_{n+1}^{ℓ} . The graph is automatically scaled such that the most important reactions for the total luminosity are presented most prominently. If a reaction conserves the analyzed quantity we are free to include or not include it in the evaluation of the mean free path in Eq. (B5) and the emissivities in Eq. (B4). Scattering, for example, does not change the neutrino number. If we include scattering as a reaction in the analysis of the number luminosity, the attenuation coefficients would indicate the probability to escape from a given location without any further scattering. If we do not include scattering, the attenuation coefficients indicate the (in many cases larger) probability to escape from a given location without being absorbed on the way out. The number luminosity is the same in both cases because scattering conserves the number of propagating neutrinos. If we work with the energy luminosity instead of the number luminosity, we have to include neutrino-electron scattering because this reaction affects the energy of escaping

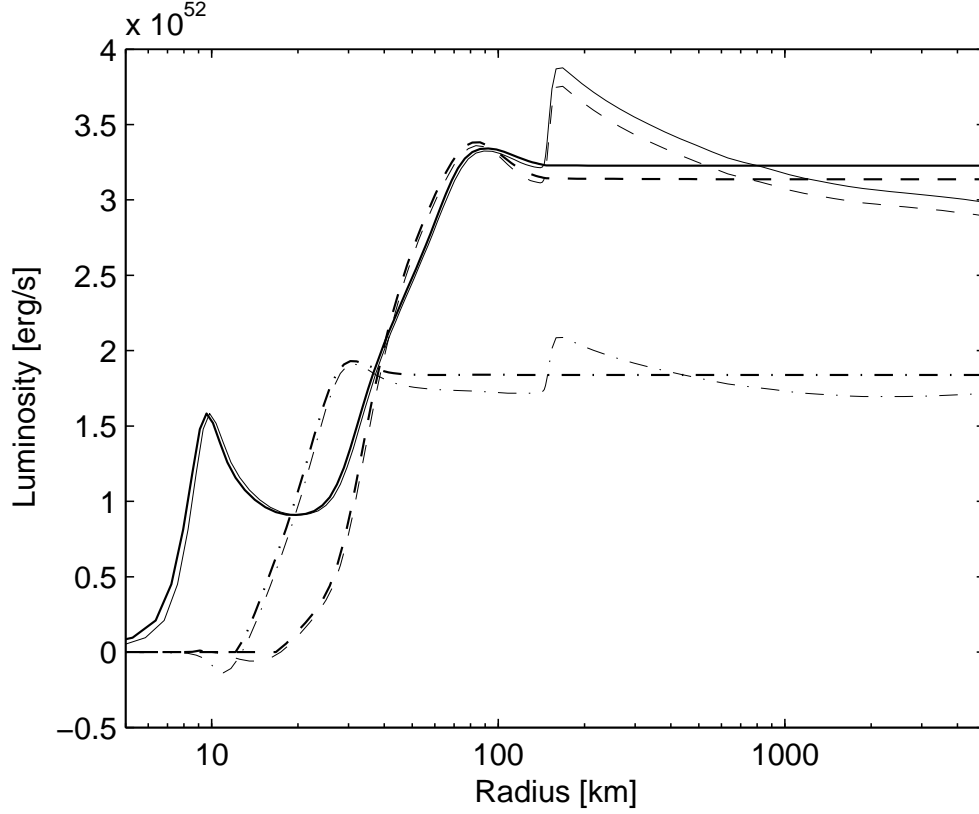


Fig. 24.— The thin lines show the luminosity profiles in the evolution of the $13 M_{\odot}$ progenitor star at 100 ms after bounce. The solid line represents the electron neutrino luminosity, the dashed line the electron antineutrino luminosity, and the dash-dotted line the μ - and τ -neutrino luminosity. The thick lines show the luminosity profiles evaluated according to Eq. (B4), i.e. based on attenuated local emissivities. The reconstruction obviously misses the observer corrections in regions with low interaction rates. Otherwise, it reproduces the original luminosities sufficiently well to be accurate in the analysis of the formation of the neutrino spectra.

neutrinos after their production. We simply decompose a neutrino-electron scattering reaction into a neutrino absorption at the incoming neutrino energy and a neutrino production at the outgoing neutrino energy. These terms are then included in the opacities and emissivities in Eqs. (B5) and (B4). In this case, the attenuation coefficients indicate the probability to escape from a given location without an energy-changing reaction. We found this choice to be the most interesting for the analysis of the formation of the neutrino spectra. The omitted isoenergetic scattering reactions are reflected in the transport spheres which are easily displayed as a complement. Finally, we mention the potential use of the attenuation coefficients for statistical evaluations, e.g. for the average radius of neutrino emission,

$$\langle r \rangle = \frac{\sum_{i=1}^n r_{i'} \xi_{n+1,i'} e m_{i'} da_{i'}}{\sum_{i=1}^n \xi_{n+1,i'} e m_{i'} da_{i'}}. \quad (\text{B7})$$

In contrast to the classical definition of the neutrinosphere, the quantity $\langle r \rangle$ accounts for regions with high emissivities in transparent regimes. Many other statistical informations at the origin of the neutrino emission may be obtained analogously.

REFERENCES

- Arnett, W. D. 1967, *Canadian J. of Phys.*, 215, 1621
- Arnett, W. D. 1977, *ApJ*, 218, 815
- Arnowitt, A., Deser, S., & Misner, C. W. 1962, in *Gravitation: An Introduction to Current Research*, ed. L. Witten (New York: Wiley)
- D’Azevedo, E. F., Messer, O. E. B., Mezzacappa, A., Peyton, B. W., Romine, C. H., & Liebendörfer, M. 2002, submitted to *SIAM Journal on Scientific Computing*
- Baron E., Cooperstein J., & Kahana, S. 1985, *Phys. Rev. Lett.*, 55, 126
- Baumgarte, T. W., Janka, H.-T., Keil, W., Shapiro, S. L., & Teukolsky, S. A. 1996, *ApJ*, 468, 823
- Bethe, H. A. & Wilson, J. R. 1985, *ApJ*, 295, 14
- Bethe, H. A. 1990, *Rev. Mod. Phys.*, 62, 801
- Bowers, R. L. & Wilson, J. R. 1982, *ApJS*, 50, 115
- Bruenn, S. W. 1985, *ApJS*, 58, 771

- Bruenn, S. W. & Haxton, W. C. 1991, *ApJ*, 376, 678
- Bruenn, S. W., DeNisco, K. R., & Mezzacappa, A. 2001, *ApJ*, 560, 326
- Bruenn, S. W. 2002, personal communication
- Buras, R., Janka, H.-T., Keil, M. T., Raffelt, G. G., & Rampp, M. 2003, *ApJ*, 587, 320
- Buras, R., Rampp, M., Janka, H.-T., & Kifonidis, K. 2003, *Phys. Rev. Lett.*, 90, 241101
- Burrows, A., Hayes, J., & Fryxell, B. A. 1995, *ApJ*, 450, 830
- Burrows, A. & Young, T. 2000, *Phys. Rep.*, 333, 63
- Burrows, A., Young, T., Pinto, Ph., Eastman, R., & Thompson, T. A. 2000, *ApJ*, 539, 865
- Castor, J. I. 1972, *ApJ*, 178, 779
- Colgate, S. A. & White, R. H. 1966, *ApJ*, 143, 626
- Dorfi, E. A. & Drury, L. O’C. 1987, *J. Comput. Phys.*, 69, 175
- Fryer, C. F. & Heger, A. 2000, *ApJ*, 541, 1033
- Fryer, C. F. & Warren, M. S. 2002, *ApJ*, 574, L65
- Galama, T. J., et al. 1998, *Nature*, 395, 670
- Glendenning, N. K. 1985, *ApJ*, 293, 470
- Herant, M., Benz, W., & Colgate, S. A. 1992, *ApJ*, 395, 642
- Herant M., Benz W., Hix R. W., Fryer C. L., & Colgate, S. A. 1994, *ApJ*, 435, 339
- Höflich, P., Wheeler, J. C., & Wang, L. 1999, *ApJ*, 521, 179
- Janka, H.-T. 1992, *A&A*, 256, 452
- Janka, H.-T. & Müller, E. 1996, *A&A*, 306, 167
- Janka, H.-T. 2001, *A&A*, 368, 527
- Janka, H.-T., Kifonidis, K., & Rampp, M. 2001, in *Proc. Workshop on Physics of Neutron Star Interiors*, ed. D. Blaschke, N. Glendenning, & A. Sedrakian, *Lecture Notes in Physics* (Germany: Springer), 333

- Khokhlov, A. M., Höflich, P. A., Oran, E. S., Wheeler, J. C., Wang, L., & Chtchelkanova, A. Yu. 1999, *ApJ*, 524, 107
- Langanke, K., Martinez-Pinedo, G., Sampaio, J. M., Dean, D. J., Hix, W. R., Messer, O. E. B., Mezzacappa, A., Liebendörfer, M., Janka, H.-T., & Rampp, M. 2003, *Phys. Rev. Lett.*, 90, 241102
- Lattimer, J. & Swesty, F. D. 1991, *Nucl. Phys.*, A535, 331
- Leonard, D. C., Filippenko, A. V., Barth, A. J., & Matheson, T. 2000, *ApJ*, 536, 239
- Lewis, E. E. & Miller Jr., W. F. 1984, *Computational Methods of Neutron Transport*, La Grange Park (New York: Wiley-Interscience)
- Liebendörfer, M. 2000, Ph.D. thesis (Basel: University of Basel)
- Liebendörfer, M., Mezzacappa, A., & Thielemann, F.-K. 2001, *Phys. Rev. D*, 63, 104003
- Liebendörfer, M., Mezzacappa, A., Thielemann, F.-K., Messer, O. E. B., Hix, W. R., & Bruenn, S. W. 2001, *Phys. Rev. D*, 63, 103004
- Liebendörfer, M., Messer, O. E. B., M., Mezzacappa, A., & Hix, W. R. 2001, in *Proceedings of the 20th Texas Symposium on Relativistic Astrophysics*, ed. by J. C. Wheeler & H. Martel (American Institute of Physics), 472
- Liebendörfer, M., Messer, O. E. B., Mezzacappa, A., Hix, R., Thielemann, F.-K., & Langanke, K. 2002, *Proc. of the 11th Workshop on Nuclear Astrophysics*, ed. W. Hillebrandt & E. Müller (Garching b. München: Springer), 126
- Liebendörfer, M., Rosswog, S. K., & Thielemann, F.-K. 2002, *ApJS*, 141, 229
- Liebendörfer, M., Rampp, M., Janka, H.-T., Mezzacappa, A 2003, in preparation
- Lindquist, R. W. 1966, *Ann. Phys.*, 37, 487
- MacFadyen, A. I. & Woosley, S. E. 1999, *ApJ*, 524, 262
- May, M. M. & White, R. H. 1966, *Phys. Rev.*, 141, 1232
- May, M. M. & White, R. H. 1967, *Comput. Phys.*, 7, 219
- Messer, O. E. B., Mezzacappa, A., Bruenn, S. W., & Guidry, M. W. 1998, *ApJ*, 507, 353
- Messer, O. E. B. 2000, Ph.D. thesis (Knoxville: University of Tennessee)

- Messer, O. E. B., Liebendörfer, M., Hix, W. R., Mezzacappa, A., & Bruenn, S. W. 2003, in Proceedings of the ESO/MPA/MPE Workshop, ed. by Hillebrandt, W. & Leibundgut, B. (Heidelberg: Springer), 70
- Mezzacappa, A. & Matzner, R. A. 1989, ApJ, 343, 853
- Mezzacappa, A. & Bruenn, S. W. 1993, ApJ, 405, 669
- Mezzacappa, A. & Bruenn, S. W. 1993, ApJ, 405, 637
- Mezzacappa, A. & Bruenn, S. W. 1993, ApJ, 410, 740
- Mezzacappa, A., Calder, A. C., Bruenn, S. W., Blondin, J. M., Guidry, M. W., Strayer, M. R., & Umar, A. S. 1998, ApJ, 495, 911
- Mezzacappa, A. & Messer, O. E. B. 1999, JCAM, 109, 281
- Mezzacappa, A., & Bruenn, S. W. 2000, Journal of the Italian Astronomical Society, 71, 515
- Mezzacappa, A., Liebendörfer, M., Messer, O. E. B., Hix, W. R., Thielemann, F.-K., & Bruenn, S. W. 2001, PRL, 86, 1935
- Mihalas, D. & Weibel-Mihalas, B. 1984, Foundations of Radiation Hydrodynamics, (Oxford University Press)
- Miller, D. S., Wilson, J. R., & Mayle, R. W. 1993, ApJ, 415, 278
- Misner, C. W., & Sharp, D. H. 1964, Phys. Rev., B136, 571
- Myra, E. S., Bludman, S. A., Hoffman, Y., Lichtenstadt, I., Sack, N., & Van Riper, K. A. 1987, ApJ, 318, 744
- Myra, E. S. & Bludman, S. A. 1989, ApJ, 340, 384
- Nomoto, K. & Hashimoto, M. 1988, Phys. Rep., 163, 13
- Pons, J. A., Reddy, S., Prakash, M., Lattimer, J. M., & Miralles, J. A. 1999, ApJ, 513, 780
- Press W. H., Teukolsky, S. A., Vetterling, W. T., Flannery, B. P. 1992, Numerical Recipes, (Cambridge: Cambridge University Press)
- Rampp, M. & Janka, H. T. 2000, ApJ, 539, L33
- Rampp, M. & Janka, H. T. 2002, A&A, 396, 361

- Rezzolla, L. & Miller, J. C. 1994, *Class. Quantum Grav.*, 11, 1815
- Schinder, P. J. & Shapiro, S. L. 1982, *ApJS*, 50, 23
- Schinder, P. J. & Bludman, S. A. 1989, *ApJ*, 346, 350
- Schwartz, R. A. 1967, *Ann. Phys.*, 43, 42
- Smarr, L. & York, J. W. 1978, *Phys. Rev.*, D17, 2529
- Smit, J. M., van den Horn, L. J., & Bludman, S. A. 2000, *A&A*, 356, 559
- Strom, R., Johnston, H. M., Verbunt, F., & Aschenbach, B. 1995, *Nature*, 373, 587
- Swesty, F. D. 1995, *ApJ*, 445, 811
- Thompson, T. A., Burrows, A., Horvath, J. E. 2000, *Phys. Rev. C*, 62, 5802
- Thompson, T. A., Burrows, A., Pinto, P. A. 2003, *ApJ*, 592, 434
- Tubbs, D. & Schramm, D. 1975, *ApJ*, 201, 467
- Tueller, J., Barthelmy, S., Gehrels, N., Leventhal, M., MacCallum, C. J., & Teegarden, B. J. 1991, in *Supernovae*, ed. by Woosley, S. E. (Berlin: Springer), 278
- Van Riper, K. A. 1979, *ApJ*, 232, 558
- Van Riper, K. A., & Lattimer, J. M. 1981, *ApJ*, 249, 270
- Wheeler, J. C., Yi, I., Höflich, P., & Wang, L. 2000, *ApJ*, 537, 810
- Wilson, J. R. 1971, *ApJ*, 163, 209
- Wilson, J. R. 1985, in *Numerical Astrophysics*, ed. by Centrella, J. M., LeBlanc, J. M., & Bowers, R. L. (Boston: Jones and Bartlett)
- Winkler, K.-H., Norman, M. L., & Mihalas, D. 1984, *J. Quant. Spectrosc. Radiat. Transf.*, 31, 473
- Woosley, S. E. & Weaver, T. A. 1995, *ApJS*, 101, 181
- Yamada, S. 1997, *ApJ*, 475, 720
- Yamada, S., Janka, H.-T., & Suzuki, H. 1999, *A&A*, 344, 533